Novel Methods in Trapped-Ion Quantum Computing: Single-Photon-Sensitive Time-Resolving Camera, Sympathetic Cooling, and Qutrit

Liudmila Zhukas

A dissertation
submitted in partial fulfillment of the
requirements for the degree of

Doctor of Philosophy

University of Washington

2021

Reading Committee:

Boris Blinov, Chair

Lukasz Fidkowski

Subhadeep Gupta

Program Authorized to Offer Degree:
Physics

University of Washington

Abstract

Novel Methods in Trapped-Ion Quantum Computing: Single-Photon-Sensitive Time-Resolving Camera, Sympathetic Cooling, and Qutrit

Liudmila Zhukas

Chair of the Supervisory Committee:
Associate Professor Boris Blinov
Department of Physics

Qubit state detection and ion imaging is an important part of quantum computation. Here we demonstrate the use of Tpx3cam, a novel single-photon sensitive camera, in trapped ion experiments. We perform detection of the multiple-qubit state as well as observation of micromotion in a linear ion chain. We show the possibility to use this camera to study collective effects in quantum jumps.

Another part of this thesis is dedicated to studying sympathetic cooling of the radial ion motion in a linear RF trap in mixed barium-ytterbium chains. In this case, barium ions are Doppler-cooled, while ytterbium ions are cooled through their interaction with the cold barium ions. We study the mechanics of the cooling and demonstrate efficient sympathetic cooling of all radial normal modes for the trap aspect ratio of approximately 2.9. Utilizing some of the hardware used for studying sympathetic cooling, we discuss the possibility to realize quantum simulations $^{138}Ba^{+}$.

TABLE OF CONTENTS

Page

LIST OF FIGURES

GLOSSARY

AOM: Acousto-optic modulator. When the RF signal is sent to the AOM, it creates a standing or running acoustic wave to diffract the laser beam.

SPAOM: Single pass acousto-optic modulator. The laser beam propagates once through the AOM.

DPAOM: Double pass acousto-optic modulator. The laser beam propagates twice through the AOM.

PID CONTROLLER: Proportional, Integral, Differential Controller with three terms proportional to the input error signal, its integral, and derivative.

PMT: Photomultiplier Tube. Photon detection device that utilises photoelectron amplification.

RF: Radio Frequency.

FWHM: Full width at half maximum.

PBS: Polarizing beam splitter.

NA: Numerical aperture.

ECDL: External cavity diode laser.

EMCCD: Electron multiplying charge coupled device.

CW: Continuous wave.

ZEMAX: Optics simulation software.

HWP: Half wave plate.

QWP: Quarter wave plate.

ROI: Region of interest.

ACKNOWLEDGMENTS

First and foremost, I thank my advisor, Boris Blinov, for welcoming me into the lab and being an amazing advisor. I appreciate how Boris offered enough freedom to help me become independent, yet he always found time to answer all my questions. Boris's creativity and passion regarding solving problems in experimental physics have drastically changed the way I look at scientific problems now.

Despite a short overlap, I want to thank Tomasz Sakrejda for being a great mentor. Due to Tomasz's teaching me and tolerating my clumsiness, I learned a lot and could operate the setup quickly. Tomasz's passion for mentorship, experience and thought-out arguments in all our discussions made a huge difference at the beginning of my graduate career.

A special thank goes to Jennifer Lilieholm for being a great labmate and a friend along the way. It was nice to share all 'ups' and 'downs' with you, endlessly talk about science and do all non-lab-related activities.

I am also thankful to the rest of the ion trappers (former and current) in Boris's lab: Megan Ivory, Alexander Kato, Sara Branson, Sarah Edwards, Carl Thomas, and Sarah Edwards. It was great to meet all of you and learn from each other. A special thank goes to all undergraduate students I worked with: Thalya Paleologu, Kurt Delegart, Yana Lozina, Maverick Millican, and Akanksha Mishra. It was a pleasure to meet such capable, hard-working students and be one of your research mentors.

Nowadays, exciting science happens in interdisciplinary fields, and our projects are no exception. I want to thank my brilliant collaborators Andrei Nomerotsky, Martin Savage, and Natalie Klco, who brought their experience and facilitated the work.

I will never forget the time when I stayed late in the lab; the reason for it was either taking new exciting data sets or complete failure of the setup. In both of these cases Eric Lindahl was always curious to know what was going on, and we spent a lot of time discussing

solutions to the problems. I got the impression that Eric knows everything, every tiny detail of experimental methods, and his bits of advice were always precious and eye-opening. I cannot thank him enough for his contribution.

I want to thank my friends: Akaxia Danaë, Dake Zhou, JunHui SeeToh, Zeeshawn Kazi, Xinxin Tang, Vladimir Milchakov, Jenni Chen, Maria Viitaniemi, Alena Bessmertnykh, Innokentiy Protasov, Maria Mikhaylova, Egor Chesakov, Katy Bogach, Mikhail Olenin, and Tatiana Olenina. Thank you for the incredible time we spent talking about science, hiking, camping, cooking, playing board games, and exploring the United States together. Special thanks here goes to Ivan Popov, who made me physically capable of lifting and moving heavy things, which impacted my career in experimental physics.

Finally, I would like to thank my parents, brother, and husband for their support. Without my parents and brother, I would never be where I am now. My husband's contribution to my career as a physicist, and my life, in general, is enormous due to his endless support. Sergey, I dedicate this thesis to you.

DEDICATION

to Sergey

Chapter 1

MOTION OF TRAPPED IONS AND LASER COOLING

This chapter describes relevant experimental techniques to trap ions and cool them for better confinement and further operations. In the first section, a general concept of trapped charged particle motion in an electromagnetic potential is given. Next, the mechanism of Doppler and sub-Doppler cooling and their necessity for certain applications are discussed. Finally, a concept of collective motion of trapped multi-species ion chains is described.

1.1 Quadrupole Ion Trap

A charged particle can be localized by using electromagnetic field. However, this problem turns out to be more difficult since Earnshaw's theorem proves that the charged particle cannot be in stable equilibrium when acted by electrostatic forces. This will be shown in the next few paragraphs.

In the case of a stable equilibrium, it is necessary for the restoring force F_i to act in the direction opposite to the particle's displacement:

$$F_i = -k_i i; k_i > 0, i = x, y, z. \tag{1.1}$$

To construct this potential, we choose electric field due to the stronger interaction with a charged particle than magnetic field. Thus, it leads us to $\vec{F} = -q\nabla\phi$, where q is the charge of the particle and ϕ is electric potential. Because we state the linearity of the force F_i above, the potential ϕ must take a form:

$$\phi = Ax^2 + By^2 + Cz^2; A, B, C > 0. \tag{1.2}$$

Recalling the Laplace equation $\triangle\phi = 0$ and requiring the stability of this system, we get $A + B + C = 0$. This contradicts the statement above: $A, B, C > 0$; thus, it is not possible to construct static electric potential to localize a charged particle.

Since the static potential does not provide a stable equilibrium, the dynamic potential is considered. In constructing the desired potential, one can impose a symmetry requirement. Since $A + B + C = 0$, $C = -(A + B)$. Assuming equal strength of electric field in x and y directions, $A = B$, the potential take this form:

$$\phi = A(x^2 + y^2 - 2z^2). \tag{1.3}$$

Here we can see the cylindrical symmetry; along the z-axis $\phi(-x) = \phi(x)$ and $\phi(-y) = \phi(y)$. Taking into account our previous assumption about the necessity of the dynamical potential, $A \to A(t)$ and, $A(t)$ is assumed periodic. Define $R^2 = x^2 + y^2$. The dynamics of this potential is shown in Figure 1.1. This illustrates how the stability of the charged particle can be achieved in the periodic potential; in Figure 1.1 a) and b) the restoring force and the force that pushes the particle away from the center alternate. Hence, by choosing the right period T, the charged particle can be stabilized in the finite region of this potential.

The invention of this type of ion trap belongs to Wolfgang Paul [84], and had led to the Nobel prize in physics shared with Hans Dehmelt and Norman Ramsey in 1989. Over time, the design of the ion traps has changed, but the main principle remained the same. Initially, designing hyperbolic electrodes to produce quadruople field were assumed to be necessary. Nowadays, cylindrical electrodes are commonly used for the ease of fabrication. The conventional linear (assuming cylindrical symmetry) trap represents four symmetrically placed cylindrical electrodes to confine ions in the radial direction and two electrodes with static potential (end caps) to confine ions in the axial direction. One diagonal pair of cylindrical electrodes is grounded, and the other pair is connected to the periodic potential. A common design of the linear trap is presented in Figure 1.2. This trap design will be the central element of this thesis.

Referring to this trap design, we can list crucial parameters and the final form of the potential. The potential can be uniquely defined by the characteristics of the internal dimension of the trap R_0, the amplitude of time-dependent part of the potential V_{RF}, its frequency Ω, the static potential U_{sq} applied to the diagonal rods, and geometric factor k of the trap. Considering all mentioned above, we get:

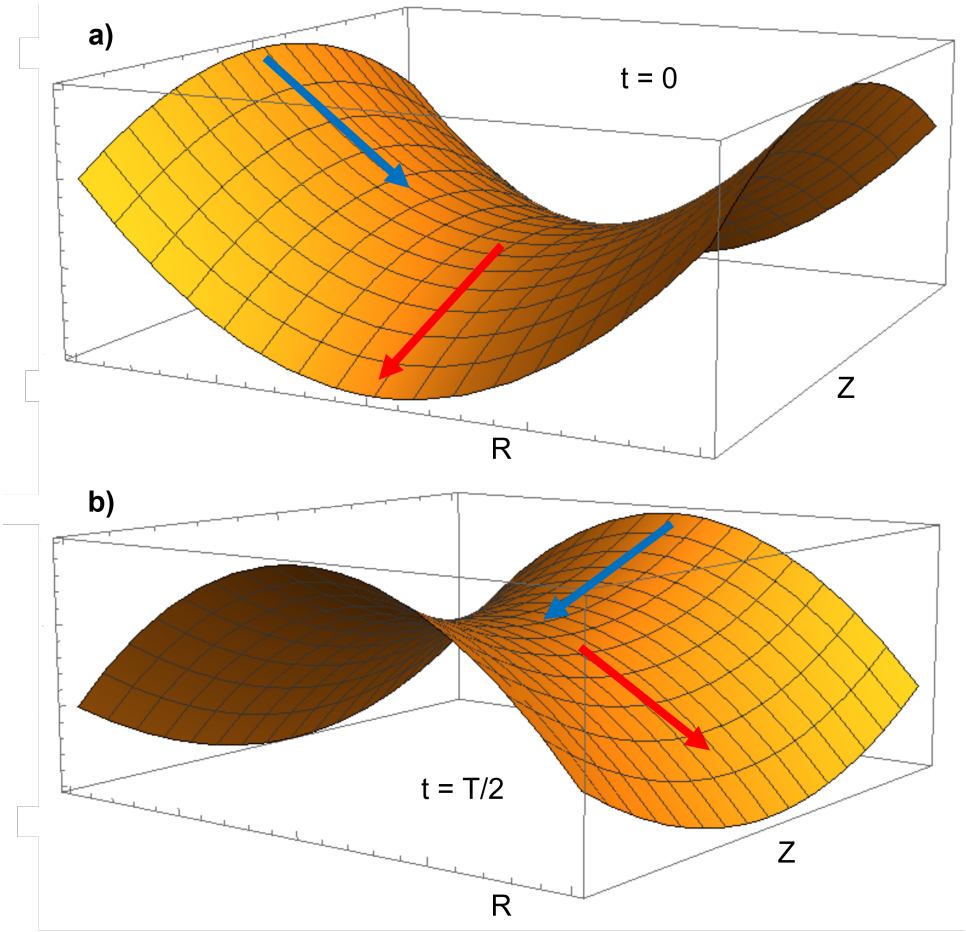

Figure 1.1: Graphical representation (a 'snapshot') of a periodical 'saddle' potential $\phi = A(t)(R^2 - 2z^2)$, where $R^2 = x^2 + y^2$. The Blue arrow corresponds to the restoring force, and the red arrow represents the force pushing the particle away from the center. a) The snapshot at t = 0. A recess in the middle is the region of a charged particle localization. However, one can see that it is not a region of stability; the restoring force is not present in all directions. b) On the second 'snapshot', one can see this potential after half of period T. In this configuration, the restoring direction is reversed compared to a).

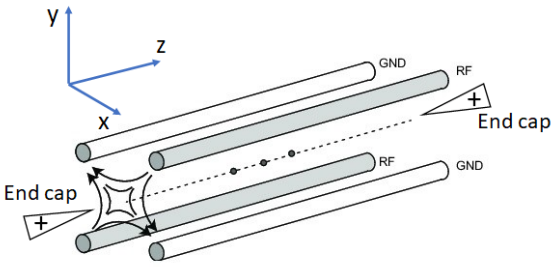

Figure 1.2: A schematic representation of a four-rod linear trap design containing three ions placed along the trap axis (dashed line). Static potentials ('+') are applied to the two end cap electrodes along the trap axis, which confine ions in the axial direction. Two opposite rods are grounded ('GND'), while the oscillating potential is applied to the other two ('RF'). A schematic drawing of the quadrupole electric field lines is shown on the left side.

$$\phi_{RF} = k\frac{U_{sq} + V_{RF}Cos(\Omega t)}{2R_0^2}(3x^2 + y^2). \tag{1.4}$$

The electric potential due to the dc electrodes at the center of the linear trap is:

$$\phi_{DC} = \alpha\frac{U_{DC}}{2z_0^2}(2z^2 - (x^2 + y^2)). \tag{1.5}$$

where U_{dc} is the dc voltage applied to both needles, α is a geometrical constant, and z_0 is the minimum distance along the z-axis from the trap center to the end cap needles.

1.2 Ion Motion In the Linear Paul Trap

In the previous section, we derived the time-dependent potential to hold ions in the trap. Now, we will describe the motion of ions in such a potential. Recall $\vec{F} = -q\nabla\phi(x, y, z, t)$:

$$\ddot{x} + \frac{qk}{mR_0^2}(U_{sq} + V_{RF}Cos(\Omega t))x + (\frac{q\alpha}{mz_0^2}U_{DC})x = 0. \tag{1.6}$$

$$\ddot{y} - \frac{qk}{mR_0^2}(U_{sq} + V_{RF}Cos(\Omega t))y + (\frac{q\alpha}{mz_0^2}U_{DC})y = 0. \tag{1.7}$$

$$\ddot{z} + \frac{\alpha q U_{DC}}{mz_0^2}z = 0. \tag{1.8}$$

The equation of motion decomposes into separate equations for each coordinate, and it can be solved separately. The equation of motion in the z-direction (see equation 1.8) results in a simple harmonic motion with the frequency $\omega_z^2 = \frac{2\alpha q U_{DC}}{mz_0^2}$. Most of the focus of this work will be on the radial motion. Reasons for this will be discussed later. For now, let's consider radial motion in the x-direction and omit U_{sq} for simplicity. The motion along the x-axis and the y-axis will be different when U_{sq} is applied. The equation along the x-axis can be transformed to the canonical Mathieu equation, where all parameters are dimensionless [3]:

$$\frac{\partial^2 x}{\partial \tau^2} + (a_x + 2q_x Cos(2\tau))x = 0, \tag{1.9}$$

where

$$\begin{aligned} \tau &= \Omega t/2, \\ q_x &= \frac{2qkV_{RF}}{R_0^2\Omega^2}, \\ a_x &= -\frac{4q\alpha U_{DC}}{z_0^2\Omega^2}. \end{aligned} \tag{1.10}$$

The general solution to Mathieu's equation is rather complex and represents an infinite series of hypergeometric functions weighted with polynomials. However, taking the lowest order, yields:

$$x(t) = x_0 Cos(\beta\Omega t)[1 - \frac{q_x}{2}Cos(\Omega t)], \tag{1.11}$$

where

$$\beta = \sqrt{a_x + \frac{q_x^2}{2}} \tag{1.12}$$

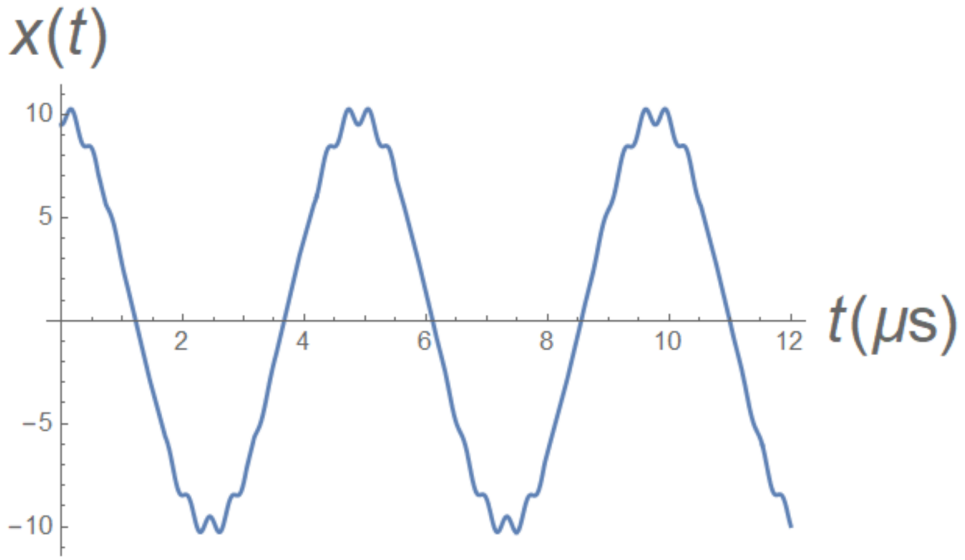

Figure 1.3: Illustration of the one-dimensional ion motion in a linear Paul trap. For this demonstration the deviation from the trap center $x_0 = 10$, $a_x = 0.0001$ and $q_x = 0.1$. The trap frequency, Ω, is 18 MHz, and the secular frequency, ω_x, is 1.28 MHz. Overall period of this motion corresponds to the secular motion, whereas the small 'perturbations' corresponds to the micromotion that happens exactly with trap frequency Ω. Note that the amplitude of the micromotion increases as an ion moves away from the trap null (x=0).

Typically, $a_x << q_x^2 << 1$. Hence, $\beta\Omega$ represents a slower motion in comparison with motion at frequency Ω; it is called the secular motion with frequency $\omega_x = \frac{\beta\Omega}{2}$. The amplitude of the fast motion happening with frequency Ω is suppressed by the factor $\frac{q_x}{2}$ and, thus, it is called the micromotion. In Figure 1.3 one can see an illustration of ion's motion in the x-direction. If time averaging is considered, then the fast oscillating term corresponding to the micromotion can be ignored. In this case, ion moves in x-direction as if it is located in a pseudo-harmonic potential:

$$V(x) = \frac{1}{2} m\omega_x^2 x^2 \tag{1.13}$$

In quantum computing with trapped ions, most protocols utilize secular motion. For

example, it can be used for the information transfer from one ion to another [61] or to implement sideband cooling [35]. For most applications using trapped ions, micromotion needs to be minimized. In fact, minimizing the amplitude of secular motion reduces the amplitude of micromotion to a certain limit [13]. This can be achieved by reducing ion's overall kinetic energy through cooling. However, there are two scenarios where the amplitude of the micromotion increases. One of them is the ion being pushed away from the trap center by, for example, a stray electric field from the charged rods (similar to Figure 1.3). And the second one is the phase difference between the RF signals applied to the trap rods [13]. More details about the micromotion, methods of its detection, and compensation will be given in the next chapters.

To conclude this section, I would like to emphasize why linear trap geometry is so commonly used. First of all, it is the possibility to optically address each ion in a linear chain. Second, it is the relative simplicity of micromotion minimization since all ions can be moved simultaneously to the trap RF null, unlike, for example, in a trap with the two-dimensional or three-dimensional trap geometry [54].

1.3 Doppler Cooling

As we discussed earlier, when exposed to the trap potential, ions undergo periodic motion. In a typical setup, when charged particles are trapped, their velocity is about a few hundred meters per second. The amplitude of the thermal motion is of order 200 μm for a typical trap. In order to reduce the kinetic energy and optically resolve the trapped ions, they need to be cooled.

The first stage of reducing trapped ions' kinetic energy is the Doppler cooling process [19]. This method requires resonant coupling of the atomic levels with the electromagnetic field. The atomic transitions used are typically dipole-allowed and cycling. The latter requirement implies the repeatability and continuity of the 'ground-to-excited' and 'excited-to-ground' transitions with a small probability of decay or off-resonance pumping ion to a different atomic level. Although it is possible to find ions that meet such requirements, see as an example [33, 11], in most cases repump laser beam is still required. By addressing more atomic transitions, we move away from the convenient two-levels system, and the description

of the transitions requires more complicated approaches, which will be discussed later. For now, I would like to focus on the two-level system.

The Doppler cooling method is based on the imbalance in the light scattering forces for a moving ion that arises from the Doppler shift. In the reference frame of the moving ion, the frequency of applied oscillating electric field has a detuning of $\Delta' = \Delta - \mathbf{kv}$, where $\mathbf{v}$ is the velocity of the ion and Δ is detuning of the field from the atomic resonance in the lab frame. When the field is red-detuned, the ion scatters more frequently with $\mathbf{kv} > 0$, and vice versa. Since the spontaneous emission is isotropic, the enhanced absorption in one direction results in more recoil energy transfer to the ion when it moves toward the beam; hence, the net momentum gain is negative. Working with the neutral atoms, two counter-propagating beams with the same detuning would be sufficient to localize an atom in one dimension, and six beams are necessary to localize the atom in all three dimensions. In the case of trapped ions, only one beam would be sufficient since the restoring force of the trap always returns ions to the condition $\mathbf{kv} > 0$. The only requirement is for the cooling laser to have a wave-vector component along all three trap axes.

The time-averaged force acting on ions due to the scattering of photons from the applied laser field in case of the dipole transition is:

$$F_s = \frac{s\Gamma/2}{1 + s + (\frac{2\Delta}{\Gamma})^2}. \tag{1.14}$$

I choose $^{138}\mathrm{Ba}^+$ $6^2\mathrm{S}_{1/2} \rightarrow 6^2\mathrm{P}_{1/2}$ transition. Here, s is the saturation parameter, $s = \frac{I}{I_0}$, where I is intensity of the applied laser beam, I_0 is the saturation intensity, $I_0 = \frac{\pi\Gamma hc}{3\lambda^3} = 20$ $\mu\mathrm{W/mm}^2$, and $\Gamma = 2\pi\times15\mathrm{MHz}$ is the natural linewidth of selected transition.

The resulting force acting on the ion, in the case where the Doppler shift is small compared to γ, is:

$$\begin{aligned} F_{tot} = F_s(\Delta - kv) - F_{trap} \approx \\ \approx F_s(\omega - \omega_0) - kv\frac{\partial F_s}{\partial \omega} - F_{trap} \approx \\ \approx -kv\frac{\partial F_s}{\partial \omega}. \end{aligned} \tag{1.15}$$

Where F$_t rap$ is the force acting on the ion by the trap electric field and/or neighboring

ions when the ion is displaced from the equilibrium position. Since the displacement is in order of nm, this force is negligible.

Next, let's discuss the minimum temperature that can be achieved with the Doppler cooling method. In one scenario, the minimum temperature is limited by external heating, which is common for chip-scale surface electrode traps where ions locate very close to the trap surface [17]. Considering the trap geometry we work with, where the ion-electrode distances are large, the limitation is caused by the randomness of spontaneous emission, which we ignored by time-averaging the scattering force (see equation 1.14). By equating two competing terms, one related to the random walk of the velocity and another one representing the Doppler cooling force (see equation 1.15); the resulting minimum temperature is reached at the optimal detuning $\Delta = \frac{\Gamma}{2}$:

$$k_B T_D = \frac{\hbar\Gamma}{2} \tag{1.16}$$

1.3.1 Doppler-Cooling and Optical Pumping of $^{138}Ba^{+}$

In this section, I would like to talk about Ba^{+} cooling. This particular ion is noticeable due to its photon emission spectra that lie in the visible range, such as transition at 493 nm. Visible range is more efficient for most available fiber optics and detectors. This makes Ba^{+} ions good candidates as communication qubits [6, 27]. In addition to its convenient, visible spectra, $^{137}Ba^{+}$ or, as it was recently introduced, $^{133}Ba^{+}$ are good candidates as informational species [113, 33]. Finally, $^{138}Ba^{+}$ is used with $^{171}Yb^{+}$, the 'clock' qubit, for sympathetic cooling, which was extensively studied in this work. Here, the atomic structure of $^{138}Ba^{+}$ is discussed.

The essential set of $^{138}Ba^{+}$ atomic levels for Doppler cooling is illustrated in Figure 1.4. The primary cooling transition is $^2S_{1/2} \rightarrow {}^2P_{1/2}$ line at 493 nm (blue). The excited state $^2P_{\frac{1}{2}}$ has a strong branching ratio of ≈ 1 to 3 to decay to the $^2D_{3/2}$ atomic level, so it is necessary to drive the $^2D_{3/2} \rightarrow {}^2P_{1/2}$ 650 nm transition (red). Since both of these transitions address the same excited state, the strong interference between these two states can be observed. Previously, we came up to the conclusion that the optimal detuning for

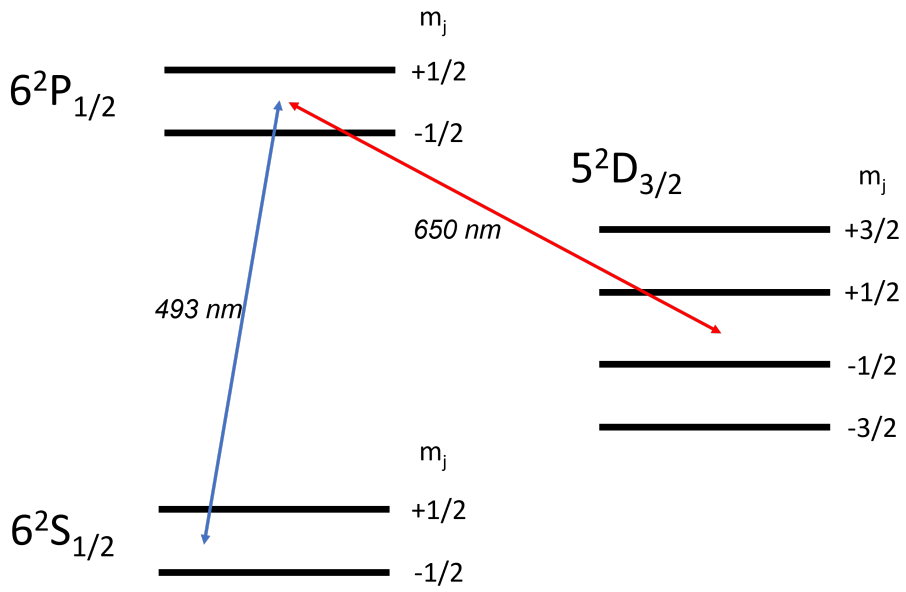

Figure 1.4: $^{138}Ba^{+}$ atomic level diagram that includes all necessary transitions for the Doppler cooling. Sub-levels for S,P and D atomic levels indicate first order Zeeman splitting due to the applied external magnetic filed, m_j indicates the z-axis projection of the total angular momentum for each sub-level.

a two-level system is $\Gamma/2$, but this can no longer be applied in this case. In order to find optimal cooling parameters, all states addressed by the cooling and the repump lasers need to be considered. Ideally, this includes all Zeeman sub-levels, which leads to a total of eight states.

Initially, let's assume only the 493 nm transition, ignoring the Zeeman splitting, as well as the direction of laser propagation and polarization - this will give us an estimate of a minimum temperature. It is convenient to represent ion's temperature or kinetic energy in terms of the average motional occupation number $\bar{n}$: $\frac{m\bar{v}^2}{2} = \frac{\hbar\Gamma}{2} = \hbar\omega\bar{n}$. Here, $\bar{v}$ is the ion's average velocity, Γ is the natural linewidth for the selected transition, and ω is the secular trap frequency. Assuming $\Gamma = 2\pi x15$ MHz for 493 nm transition and $\omega = 1.7$ MHz, the minimum temperature of the Doppler cooled ion is:

$$\bar{n} = \frac{\Gamma}{2\omega} \approx 10 \tag{1.17}$$

Next, let's consider the three-level system including $^2S_{1/2}$, $^2P_{1/2}$, and $^2D_{3/2}$ atomic levels and ignore the Zeeman splitting. Assume $|1\rangle$ state corresponds to $^2S_{1/2}$, $|2\rangle$ sate corresponds to $^2P_{1/2}$, $|3\rangle$ sate corresponds to $^2D_{3/2}$, where states $|1\rangle$, $|2\rangle$ and $|3\rangle$ form the basis:

$$|1\rangle = \begin{bmatrix} 1 \\ 0 \\ 0 \end{bmatrix}, |2\rangle = \begin{bmatrix} 0 \\ 1 \\ 0 \end{bmatrix} |3\rangle = \begin{bmatrix} 0 \\ 0 \\ 1 \end{bmatrix} \tag{1.18}$$

Then the part of Hamiltonian that represents the levels $\hat{H}_{atomic}$ takes the form:

$$\hat{H}_{atomic} = \hat{I}\hat{H}_{atomic}\hat{I} = \sum_{n=0}^{3} \hbar\omega_n |n\rangle\langle n| \tag{1.19}$$

Where $n = 1,\ 2,\ 3$, and $\hbar\omega_n$ corresponds to the energy of the state n.

$$\hat{I} = |1\rangle\langle 1| + |2\rangle\langle 2| + |3\rangle\langle 3| \tag{1.20}$$

.

For more convenience, this Hamiltonian can be written in the matrix form. Setting energy of the state $|2\rangle$ equal zero, the Hamiltonian takes the following form:

$$\hat{H}_{atomic} = \hbar \begin{pmatrix} \omega_1 - \omega_2 & 0 & 0 \\ 0 & 0 & 0 \\ 0 & 0 & \omega_3 - \omega_2 \end{pmatrix} \tag{1.21}$$

The second part of the Hamiltonian, $\hat{H}_{int}$, represents interaction with the electromagnetic field. Since all transitions are dipole-allowed, the Hamiltonian is:

$$\hat{H}_{int} = -\vec{D} \cdot \vec{E} \tag{1.22}$$

where $\vec{E}$ is the incident electric field operator and $\vec{D}$ is the dipole moment operator.

Three atomic levels are coupled with two laser fields. As it was mentioned above, 493 nm light (blue) drives the transition between the states $|1\rangle$ and $|2\rangle$ while 650 nm light (red) couples states $|2\rangle$ and $|3\rangle$. Ideally, we can use a representation for quantized electromagnetic field and take into account states of photons. However, there is no need for it because the state of the laser electric field is not strongly affected by losing a single photon. Moreover, here we are not interested in monitoring the states of the photons. Hence, classical representation for the monochromatic electric field is sufficient:

$$\vec{E}(t) = \vec{\epsilon} E_o e^{i\omega t} \tag{1.23}$$

Where $\vec{\epsilon}$ is electric field polarization, E_o is electric field amplitude, and ω is a frequency of either 650 or 493 nm light, define these frequencies as ω_r and ω_b respectively. Note that we omit complex-conjugated term in the equation for convenience.

Define $\vec{D}_{12}$ and $\vec{D}_{23}$, E_b and E_r, $\vec{\epsilon}_b$ and $\vec{\epsilon}_r$ as dipole moments, electric field amplitudes, and polarisations for 493 and 650 nm transitions respectively. Knowing that $D_{ij} = D_{ij}^*$, $\hat{H}_{int}$ becomes:

$$\hat{H}_{int} = \hbar \begin{pmatrix} 0 & \frac{\vec{\epsilon}_b \vec{D}_{12} E_b}{2} e^{i\omega_b t} & 0 \\ \frac{\vec{\epsilon}_b \vec{D}_{12} E_b}{2} e^{-i\omega_b t} & 0 & \frac{\vec{\epsilon}_r \vec{D}_{23} E_r}{2} e^{-i\omega_r t} \\ 0 & \frac{\vec{\epsilon}_r \vec{D}_{23} E_r}{2} e^{i\omega_r t} & 0 \end{pmatrix} \tag{1.24}$$

Finally, $\hat{H}_{tot} = \hat{H}_{atomic} + \hat{H}_{int}$:

$$\hat{H}_{tot} = \hbar \begin{pmatrix} \omega_1 - \omega_2 & \frac{\vec{\epsilon}_b \vec{D}_{12} E_b}{2} e^{i\omega_b t} & 0 \\ \frac{\vec{\epsilon}_b \vec{D}_{12} E_b}{2} e^{-i\omega_b t} & 0 & \frac{\vec{\epsilon}_r \vec{D}_{23} E_r}{2} e^{-i\omega_r t} \\ 0 & \frac{\vec{\epsilon}_r \vec{D}_{23} E_r}{2} e^{i\omega_r t} & \omega_3 - \omega_2 \end{pmatrix} \tag{1.25}$$

It is convenient to further rewrite $\hat{H}_{tot}$ in terms of the Rabi-frequency since it can be measured in an experiment. Note that values of the Rabi frequencies are real. Define the Rabi frequencies Ω_b and Ω_r as:

$$\Omega_b = \frac{\vec{\epsilon}_b \vec{D}_{12} E_b}{\hbar}$$
$$\Omega_r = \frac{\vec{\epsilon}_r \vec{D}_{23} E_r}{\hbar} \tag{1.26}$$

It is more convenient to move into a frame rotating at the laser frequency. Applied unitary operator $\hat{U}_0$(t) is:

$$\hat{U}_0(t) = e^{\frac{-i\hat{H}_{atomic}t}{\hbar}} = \begin{pmatrix} e^{-i\omega_1 t} & 0 & 0 \\ 0 & 1 & 0 \\ 0 & 0 & e^{-i\omega_2 t} \end{pmatrix} \tag{1.27}$$

Omitting the fast oscillating terms, the $\hat{H}_I$ in the rotating frame becomes:

$$\hat{H}_I = \hat{U}_0^{\dagger}(t)\hat{H}_{tot}(t)\hat{U}_0(t) - i\hbar\frac{d\hat{U}_0{}^{\dagger}(t)}{dt} =$$
$$= \hbar \begin{pmatrix} \omega_b - (\omega_1 - \omega_2) & \frac{\Omega_b}{2\hbar} & 0 \\ \frac{\Omega_b}{2} & 0 & \frac{\Omega_r}{2} \\ 0 & \frac{\Omega_r}{2\hbar} & \omega_r - (\omega_3 - \omega_2) \end{pmatrix} \tag{1.28}$$

Define the blue and red laser detunings:

$$\omega_b - (\omega_1 - \omega_2) = \Delta_b$$
$$\omega_r - (\omega_3 - \omega_2) = \Delta_r \tag{1.29}$$

To complete this model, spontaneous emission needs to be introduced.

Population decays from state $|2\rangle$ to sate $|1\rangle$ and from state $|2\rangle$ to sate $|3\rangle$ (we ignore the $|3\rangle$ to $|1\rangle$ decay since the $^2D_{3/2}$ state's lifetime is ≈80 s.). This decay process can be treated using previously defined state vectors and a non-Hermitian Hamiltonian. Hence, the transition to density matrix $\hat{\rho}$ needs to be made where the diagonal terms describe the probability to be in the state, whereas the off-diagonal elements relate to relaxation (called 'coherence' terms). The evolution of the density matrix elements is described by the Liouville equation:

$$\frac{d\hat{\rho}}{dt} = -\frac{i}{\hbar}[\hat{H}_{tot}, \hat{\rho}] - \frac{1}{2}\sum_n \hat{C}_n^{\dagger}\hat{C}_n\hat{\rho} + \hat{\rho}\hat{C}_n^{\dagger}\hat{C}_n - 2\hat{C}_n^{\dagger}\hat{\rho}\hat{C}_n \tag{1.30}$$

where

$$\hat{\rho} = \sum_{m,n=1,2,3} \hat{\rho}_{mn}|m\rangle\langle n| \qquad \sum_{n=1,2,3} \hat{\rho}_{nn} = 1 \tag{1.31}$$

Operators $\hat{C}_n$ form off-diagonal terms in the same basis that describe dissipative processes. In our case this is a decay to the lower states $|1\rangle$ and $|3\rangle$, and the decoherence through the finite bandwidth of applied laser radiation:

$$\begin{aligned} \hat{C}_{21} &= \sqrt{\Gamma_{21}}|1\rangle\langle 2| \\ \hat{C}_{23} &= \sqrt{\Gamma_{23}}|3\rangle\langle 2| \\ \hat{C}_{b} &= \sqrt{\Gamma_{b}}|1\rangle\langle 1| \\ \hat{C}_{r} &= \sqrt{\Gamma_{r}}|3\rangle\langle 3| \end{aligned} \tag{1.32}$$

Under the previous consideration to move into the rotating frame (Eq. 1.27), the density matrix needs to be transformed:

$$\hat{\rho}_I = \hat{U}_0(t)\hat{\rho}(t)\hat{U}_0^{\dagger}(t) \tag{1.33}$$

Next, $\hat{\rho}_I$, $\hat{H}_I$, and $\hat{C}_n$ are plugged in 1.30. In order to get all components of the density matrix, set of linear differential equations need to be solved. An example of the evolution of the diagonal component of the density matrix is in Figure 1.5. The system was initialized in the ground $S_{1/2}$ state so $\rho_{11}[0] = 1,\ \rho_{22}[0] = 0,\ \rho_{33}[0] = 0$, and only 493 nm radiation was applied.

To obtain the fluorescence intensity versus the detuning of one of the lasers, we need to find one component of the density matrix, ρ_{22}. The population ρ_{22} can be calculated from the steady-state solutions. Then the average rate of emitted photons:

$$\begin{aligned} N_{tot} &= N_b + N_r \\ N_b &= \Gamma_{21}\rho_{22} \\ N_r &= \Gamma_{23}\rho_{22} \end{aligned} \tag{1.34}$$

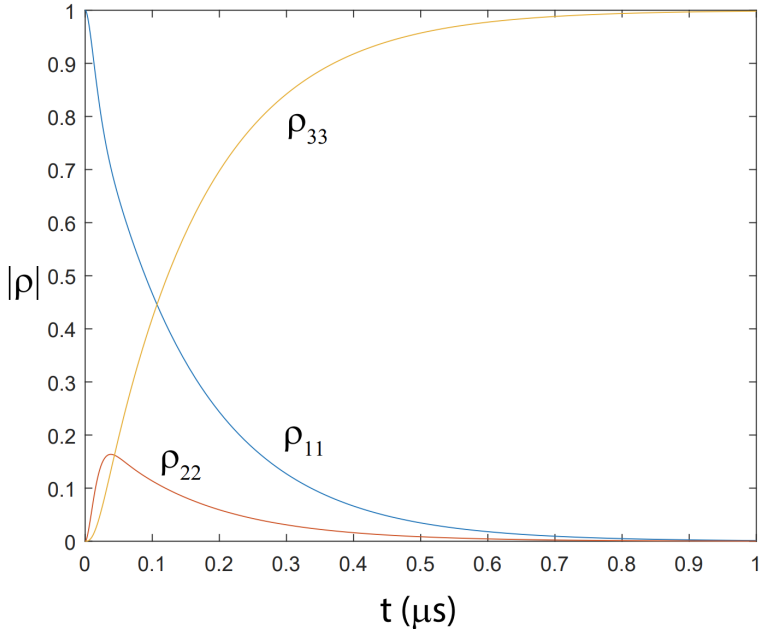

Figure 1.5: Evolution of the density matrix diagonal components when the ion was initialized in the ground S-state with only 493 nm light applied. Selected parameters are: $s_b = 1, \Delta_b = 0, \Delta_r = 0, \Gamma_b = 0, \Gamma_r = 0$. It is obvious from this Figure that the steady-state solution can be reached in less than 1 μs.

The saturation parameter determines the intensity at which a substantial amount of population is pumped to the excited state. Thus, it is convenient to represent the Rabi-frequency in terms of the saturation parameters related to the laser power s_b or s_r:

$$\Omega_{b,r} = \sqrt{\frac{s_{b,r}}{2}}\Gamma_{21} \tag{1.35}$$

One notable feature in the spectrum appears when $\Delta_r = \Delta_b$. In this condition the ion is in the superposition of states $|1\rangle$ and $|3\rangle$ whereas state $|2\rangle$ is not populated ($\rho_{22} = 0$). Hence, there is no fluorescence from the ion. The steady-state solution ($\mathrm{d}\hat{\rho}_d/\mathrm{dt} = 0$) for the density matrix under this condition would be:

$$\hat{\rho}_d = \begin{pmatrix} \frac{\Omega_b^2}{\Omega_b^2+\Omega_r^2} & 0 & \frac{\Omega_b\Omega_r}{{\Omega_b}^2+{\Omega_r}^2} \\ 0 & 0 & 0 \\ \frac{\Omega_b\Omega_r}{\Omega_b^2+\Omega_r^2} & 0 & \frac{\Omega_r^2}{\Omega_b^2+\Omega_r^2} \end{pmatrix} \tag{1.36}$$

This phenomenon is common for Λ systems and has the name 'dark resonance' because no fluorescence is observed in this case. The perfect condition where the ion is in the superposition of states $|1\rangle$ and $|3\rangle$ so that $\rho_{22} = 0$ does not happen in reality due to non-zero linewidths of the 650 and 493 nm lasers. The larger these linewidths are, the less deep these 'dark resonances' become. All possible attempts should be taken to avoid this resonance since it reduces the efficiency of Doppler cooling. Fortunately, this is doable since either of the laser frequencies can be tuned to avoid $\Delta_r = \Delta_b$. In addition, turning on a small magnetic field ($\sim$1Gauss) helps to avoid the resonance. Experimental observations of the 'dark resonance' while scanning frequencies of both lasers were done on our setup and are described in detail here [93].

In order to simplify the expression for ρ_{22} and to plot the number of emitted photons versus the detuning of the blue laser, assume the red laser frequency is set exactly at the resonance between $|2\rangle$ and $|3\rangle$. There is a noticeable decrease of photon emission when $\Delta_b = 0$, and both saturation parameters are equal to 1. In this case some population is trapped into the lower level $|1\rangle$ ($\rho_{11} \approx 1$) leaving the middle level $|3\rangle$ and upper levels $|2\rangle$ less populated, see Figure 1.6. If the power of the blue laser is increased so that $s_b = 5$, the 'dark resonance' become more prominent, see Figure 1.7. Moreover, it significantly broadens the

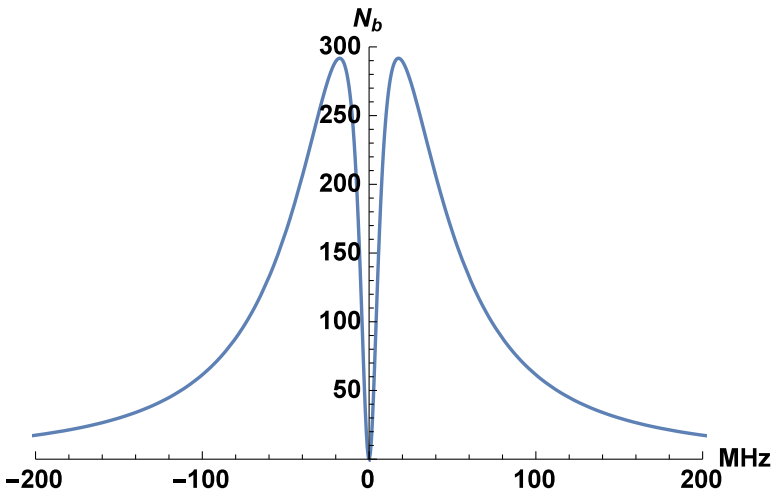

Figure 1.6: Number of 493 nm photons (see equation 1.34) collected with 1% efficiency with acquisition time of 50 ms versus detuning of the blue laser Δ_b from the $|2\rangle$-$|1\rangle$ resonance taking steady-state solution for ρ_{22}. Red laser is set on resonance with $|2\rangle$ and $|3\rangle$. Saturation parameters are: $s_b = 1$, $s_r = 1$. $\Gamma_{21} = 15.1$ MHz$/2\pi$ and $\Gamma_{23} = 5.3$ MHz$/2\pi$, $\Gamma_b = \Gamma_r = 0$.

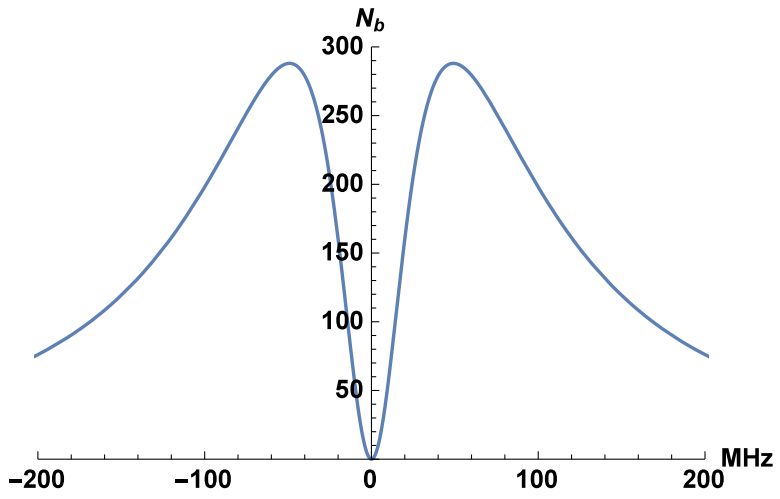

Figure 1.7: Number of 493 nm photons (see equation 1.34) collected with 1% efficiency with acquisition time of 50 ms versus detuning of the blue laser Δ_b from the $|2\rangle$-$|1\rangle$ resonance taking steady-state solution for ρ_{22}. Red laser is set on resonance with $|2\rangle$ and $|3\rangle$. Saturation parameters are: $s_b = 5$, $s_r = 1$. $\Gamma_{21} = 15.1$ MHz$/2\pi$ and $\Gamma_{23} = 5.3$ MHz$/2\pi$, $\Gamma_b = \Gamma_r = 0$.

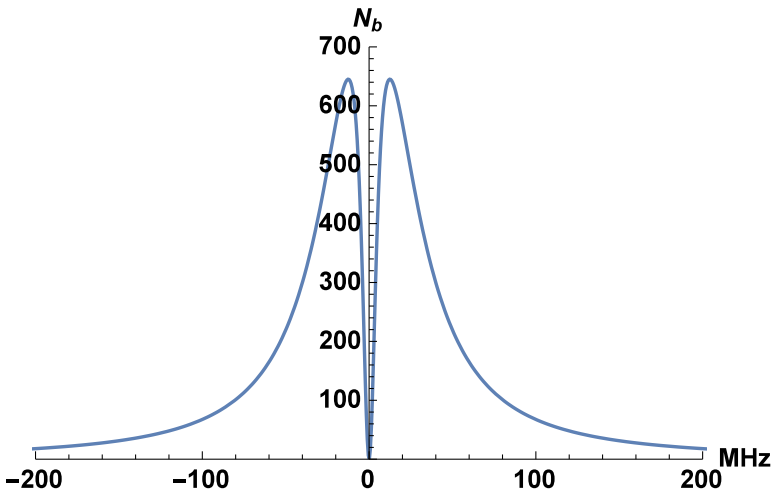

Figure 1.8: Number of 493 nm photons (see equation 1.34) collected with 1% efficiency with acquisition time of 50 ms versus detuning of the blue laser Δ_b from the $|2\rangle$-$|1\rangle$ resonance taking steady-state solution for ρ_{22}. Red laser is set on resonance with $|2\rangle$ and $|3\rangle$. Saturation parameters are: $s_b = 1$, $s_r = 5$. $\Gamma_{21} = 15.1$ MHz$/2\pi$ and $\Gamma_{23} = 5.3$ MHz$/2\pi$, $\Gamma_b = \Gamma_r = 0$.

curve and makes cooling less efficient. On the other hand, leaving $s_b = 1$ and increasing power of the 650 nm red laser ($s_r = 5$) leads to a more narrow dark resonance peak as well as higher fluorescence rate and the possibility to perform more efficient cooling, see Figure 1.7. So, practically, it is better to keep 650 nm laser a few times higher than the power of 493 nm laser while maintaining $s_{b,r} < 10$ to avoid power broadening. For efficient cooling, the 493 nm laser needs to stay ≈20-30 MHz lower than the resonance.

1.4 Lamb-Dicke Regime and Resolving Motional Sidebands

As was discussed in the previous two chapters, ions can be Doppler cooled with the red-detuned lasers. Ions undergo macro-motion in a 3-dimensional harmonic potential. In each of these three directions, the ion vibrates at a different frequency (generally), determined by the strength of the potential. In this section, for simplicity, we only consider one dimension out of three.

During the cooling process, the kinetic energy transferred to an ion by absorption or emission of a photon with frequency ω_{eg} is called the recoil energy E_{rec}:

$$E_{rec} = \frac{\hbar^2 k^2}{2m} \tag{1.37}$$

Where $k = \omega_{sec}/c$ and m is the mass of the ion.

The Lamb-Dicke parameter η is defined as the ratio between the rms size of the ground state wavefunction of the ion in the tap $\sqrt{\langle 0|r^2|0\rangle} = \sqrt{\hbar/2m\omega_{sec}}$ and the wavelength λ_0 of light, ω_{sec} is the secular trap frequency (see section 1.2):

$$\eta = \frac{\sqrt{\hbar/2m\omega_{sec}}}{\lambda_0/2\pi} \tag{1.38}$$

If the ion is not in the ground state, but in the state $|n\rangle$ of the harmonic oscillator, then equation 1.38 is modified to:

$$\eta_n = \sqrt{2n+1}\eta \tag{1.39}$$

In this work, we aim for $\eta_n < 1$ to be able to implement resolved sideband spectroscopy with narrow 1762 nm laser light. If $\eta_n < 1$, in ion's reference frame the laser light is

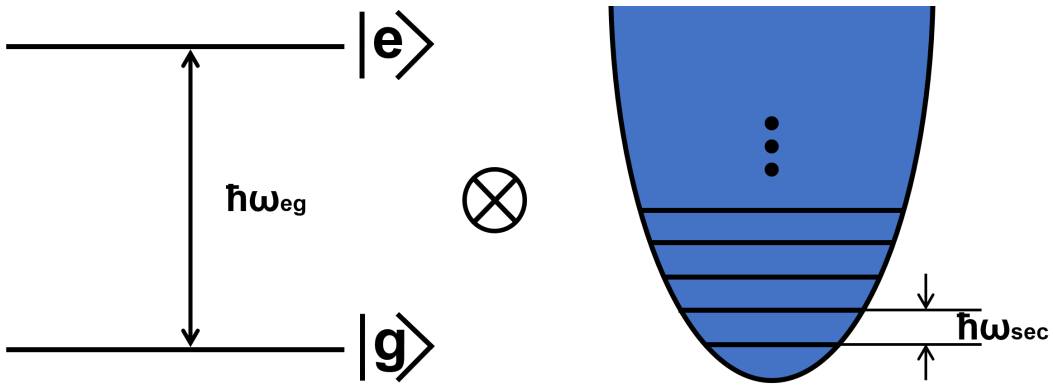

Figure 1.9: Illustration of the tensor product of a two-level atomic structure and the motional states in a linear harmonic trap. Here, ω_{sec} is the secular trap frequency, and ω_{eg} is the resonant frequency.

modulated with trap frequency ω_i. In the case of weak confinement i.e. $\omega_i << $ resonance light linewidth Γ, these sidebands are not resolved. However, if $\omega_i >> \Gamma$, then by scanning the frequency of the resonance light, a motional sideband can be resolved.

At this point, it is important to recall that the resulting state of the ion in a trap is a tensor product of the two-level internal atomic structure and the motional states, as illustrated in figure 1.9. Hence, atomic transitions can happen together with motional transitions. However, as we will show later, lowering the Lamb-Dickie parameter to $\eta_n << 1$ imposes restrictions on the motional transitions.

The 'bare' Hamiltonian $\hat{H}_0$ of a single trapped ion consist of two terms, a term that represents the harmonic trap potential and a term that represents the internal atomic two-level structure:

$$\hat{H}_0 = \hbar\omega_{sec}(\hat{a}^\dagger\hat{a} + \frac{1}{2}) + \frac{\hbar\omega_{eg}}{2}\hat{\sigma}_z \tag{1.40}$$

where $\hat{a}^\dagger$ and $\hat{a}$ are raising and lowering operators (also called the creation and annihilation operators) acting on the motional ion states, $\hbar\omega_{eg}$ is splitting between $|e\rangle$ and $|g\rangle$ atomic levels, and $\hat{\sigma}_z$ is the Pauli matrix.

With an oscillating electric field applied along the x-axis, the interaction Hamiltonian

$\hat{H}_I$ is:

$$\hat{H}_I = -qxE_oCos(\omega t - kr) \tag{1.41}$$

Where E_0 is an amplitude, ω is the oscillating frequency of the electric field, k is the wave-vector, x is the ion's displacement from the x=0 (in the case when no field is present) along the x-axis, and r is a coordinate in the direction of the propagating vector k.

Rewriting this in $|e\rangle$, $|g\rangle$ complete basis gives:

$$\hat{H}_I = -q(|e\rangle\langle g|\langle e|x|g\rangle + |g\rangle\langle e|\langle g|x|e\rangle)Cos(\omega t - kr) \tag{1.42}$$

Note that $\langle e|\langle g|$ and $|g\rangle\langle e|$ are the raising $\hat{\sigma}_+$ and lowering $\hat{\sigma}_-$ operators, and the matrix elements with the x in it relate to the Rabi frequency Ω:

$$\Omega = \frac{\langle g|exE_0|e\rangle}{\hbar} \tag{1.43}$$

The ion's coordinate r along the propagating vector k can be expressed in terms of $\hat{a}^\dagger$ and $\hat{a}$:

$$\hat{H}_I = -\hbar\Omega[\hat{\sigma}_+ + \hat{\sigma}_-]Cos(\omega t - kr) =$$

$$= -\hbar\Omega[\hat{\sigma}_+ + \hat{\sigma}_-]Cos\left(\omega t - k\sqrt{\frac{\hbar}{2m\omega_{sec}}}(\hat{a} + \hat{a}^\dagger)\right) = \tag{1.44}$$

$$= \frac{-\hbar\Omega}{2}[\sigma_+ + \sigma_-][e^{i[\omega t - \eta(\hat{a}+\hat{a}^\dagger)]} + e^{-i[\omega t - \eta(\hat{a}+\hat{a}^\dagger)]}]$$

Assuming $\eta << 1$ and performing Taylor-expansion of the exponents, while keeping the lowest order terms, we get:

$$\hat{H}_I \approx \frac{-\hbar\Omega}{2}[\sigma_+ + \sigma_-][(e^{i\omega t} + e^{-i\omega t}) - i\eta\hat{a}(e^{i\omega t} - e^{-i\omega t}) - i\eta\hat{a}^\dagger(e^{i\omega t} - e^{-i\omega t})] \tag{1.45}$$

From the expression 1.45 one can see that if $\eta << 1$, the atomic states change is associated with either no motional state change $\Delta n = 0$, or with $\Delta n = \pm 1$. The first

transition is called the 'carrier', the $\Delta n = -1$ transition is called 'red sideband', and $\Delta n = +1$ is called 'blue sideband'. On the spectrum, the red and blue sidebands are equidistant from the carrier such that $|\omega^{carrier} - \omega_{r,b}^{side}| = \omega_{sec}$. One can scan the frequency of the laser to locate the carries and both sidebands; this is called motional spectroscopy. We work in the regime $\eta << 1$ to study ions' collective motion and to perform the optical qubit operations.

The wavelength we aim to use to perform ion's motional spectroscopy is $\lambda_0 = 1762$ nm. One can estimate what n is needed to reach $\eta << 1$. Taking that the probability P_n of being in vibrations state n obeys Maxwell-Boltzmann distribution:

$$P_n = \frac{1}{1+\bar{n}} \frac{\bar{n}^n}{(1+\bar{n})^n} e^{-\frac{n\hbar\omega_{sec}}{k_b T}} = \\ = \frac{1}{1+\bar{n}} \frac{\bar{n}^n}{(1+\bar{n})^n} e^{-\frac{n}{\bar{n}}} \tag{1.46}$$

Where the system has an average energy $\langle E \rangle$, k_b is the Boltzmann constant, and we define $\bar{n}$ as average motional occupation number:

$$\langle E \rangle = k_b T = \bar{n}\hbar\omega_{sec} \tag{1.47}$$

Now using equations 1.39, 1.38 and assuming that $\frac{\bar{n}}{1+\bar{n}} \sim 1$ since the Doppler-cooling limited $\bar{n} \sim 10$, we get the following condition:

$$\frac{\eta}{1+\bar{n}} \int_0^\infty \sqrt{n} e^{\frac{n}{\bar{n}}} dn << 1 \tag{1.48}$$

or

$$\frac{\sqrt{\pi}\eta}{1+\bar{n}} \bar{n}^{3/2} << 1 \tag{1.49}$$

Taking $\omega_{sec} = 1.5$ MHz, $\lambda_0 = 1.72$ μm, the resulting condition applying to $\bar{n}$ is:

$$\bar{n} << 500 \tag{1.50}$$

This means that even with just the Doppler cooling, we are well within the Lamb-Dicke limit.

1.5 Collective radial motion of different ion species in a linear harmonic trap

When several ions are trapped, they undergo collective motion that can be described classically. In this work, we are interested in transverse or radial motion, which is discussed in this section. Nevertheless, a similar approach can be repeated for the axial motion. The only differences are the weaker confinement and the stronger Coulomb interaction along the trap axis.

For simplicity, we will focus on describing the motion of two ions: a $^{138}Ba^{+}$ ion and a $^{171}Yb^{+}$ ion; this can be solved analytically. First, let's write down the kinetic energy in one transverse direction of motion:

$$K_t = \frac{m_1 \dot{x}_1}{2} + \frac{m_2 \dot{x}_2}{2}, \tag{1.51}$$

Where m_1, m_2 are masses of the selected ions, x_1, x_2 are the displacements of the first and the second ions along the selected direction of motion (x was selected in this case).

The potential energy of the ions due to the transverse field U_t:

$$U_t = \frac{m_1 \omega_1^2 x_1^2}{2} + \frac{m_2 \omega_2^2 x_2^2}{2} + \frac{e}{|\vec{r_1} - \vec{r_2}|} \tag{1.52}$$

Where $\omega_{1,2}$ are the secular motional frequencies of ion 1 and 2 in the transverse direction x, $\vec{r_1}, \vec{r_2}$ are ion's positions. Since k is the characteristic of the potential (transverse) both ions move in, $k = m_1\omega_1^2 = m_2\omega_2^2$.

The next step is the Taylor series expansion of Coulomb interaction from equation 1.52. Assuming that the separation between ion ($\sim 10\mu$m) along z-axis $z_1 - z_2$ is much larger than the displacement along the x-axis, and e = 1:

$$\frac{1}{|\vec{r_1}-\vec{r_2}|}=\frac{1}{\sqrt{(z_1-z_2)^2+(x_1-x_2)^2}}\approx$$
$$\approx\frac{1}{z_1-z_2}\left(1-\frac{1}{2}\frac{(x_1-x_2)^2}{(z_1-z_2)^2}\right) \tag{1.53}$$

The Lagrange equations are:

$$\begin{aligned}\frac{d}{dt}\frac{\partial L}{\partial\dot{q}_i}-\frac{\partial L}{\partial q_i}&=0\\ L&=K_t-U_t\\ q_i&=x_1,x_2\end{aligned} \tag{1.54}$$

We assume that the ions are at the fixed equilibrium positions along the z-axis. The potential energy U_l due to motion along z-axis is:

$$U_l=\frac{k_l z_1^2}{2}+\frac{k_l z_2^2}{2}+\frac{e}{|z_1-z_2|} \tag{1.55}$$

Where k_l is is the characteristic of the potential (longitudinal) both ions move in, and $k_l=m_1\omega^2$, where ω is the motional frequency along the z-axis of the ion 1.

One can find the equilibrium position along z- and x-axes by minimizing U_l and U_t:

$$\begin{aligned}\frac{\partial U_t}{\partial x_i}&=0\\ \frac{\partial U_l}{\partial z_i}&=0\end{aligned} \tag{1.56}$$

The equilibrium positions along the x-axis are: $x_1^e=0,\ x_2^e=0.$ he equilibrium positions along z-axis are: $z_1^e=-(1/2k_l^2)^{2/3}=-(1/2m_1^2\omega^4)^{2/3},\ z_2^e=(1/2m_1^2\omega^4)^{2/3}$.

Then the Lagrangian equation for the radial motion transforms into:

$$\begin{aligned}m_1\ddot{x}_1+\left.\frac{\partial^2 U_t}{\partial x_1^2}\right|_0 x_1+\left.\frac{\partial^2 U_t}{\partial x_1\partial x_2}\right|_0 x_2=0\\ m_2\ddot{x}_2+\left.\frac{\partial^2 U_t}{\partial x_2^2}\right|_0 x_2+\left.\frac{\partial^2 U_t}{\partial x_1\partial x_2}\right|_0 x_2=0\end{aligned} \tag{1.57}$$

When applying results from 1.56, the final equations are:

$$\left(\omega_1^2 - \frac{\omega^2}{2}\right) x_1 + \frac{\omega^2}{2} x_2 = \omega_v^2 x_1$$
$$\frac{\omega^2}{2}\frac{m_1}{m_2} x_1 + \left(\omega_1^2 \frac{m_1}{m_2} - \frac{\omega^2}{2}\frac{m_1}{m_2}\right) x_2 = \omega_v^2 x_2 \tag{1.58}$$

This can be solved by finding the eigenvectros with corresponding eigenstates ω_v ($b = \frac{m_1}{m_2}$, $a = \omega_1^2 - \frac{\omega^2}{2}$, and $c = \frac{\omega^2}{2}$):

$$\omega_{v1,2} = \frac{a(b+1)(1 \pm \sqrt{1 - \frac{4ba^2 - c}{a^2(b+1)^2}})}{2} \tag{1.59}$$

These solutions correspond to two modes: 'in phase' and 'out of phase'. Each component of the eigenvector indicates the involvement of one of two ions in the particular mode's motion. Taking $\omega_1 = 1.5$ MHz, $\omega = 0.7$ MHz, Figure 1.10 shows eigenvalues versus the ion mass ratio.

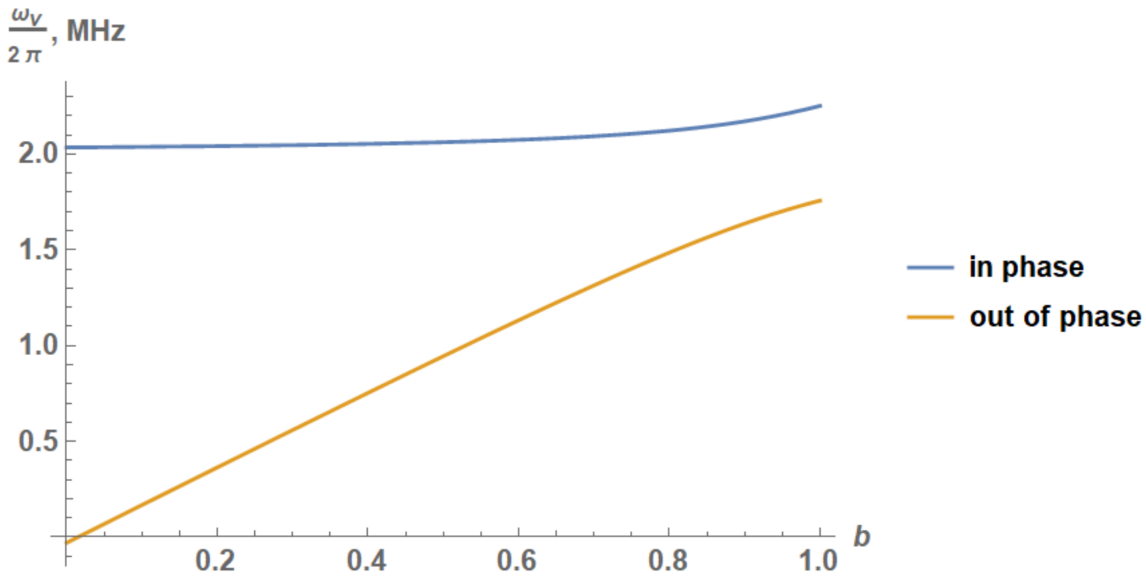

Figure 1.10: Eigenfrequencies corresponding to the transverse direction of motion assuming $\omega = 0.7$ MHz, $\omega_1 = 1.5$ MHz.

The corresponding sets of eigenvectors versus b are shown in Figures 1.12 and 1.11 for the in phase and the out of phase motional modes. One can see the trend here; with

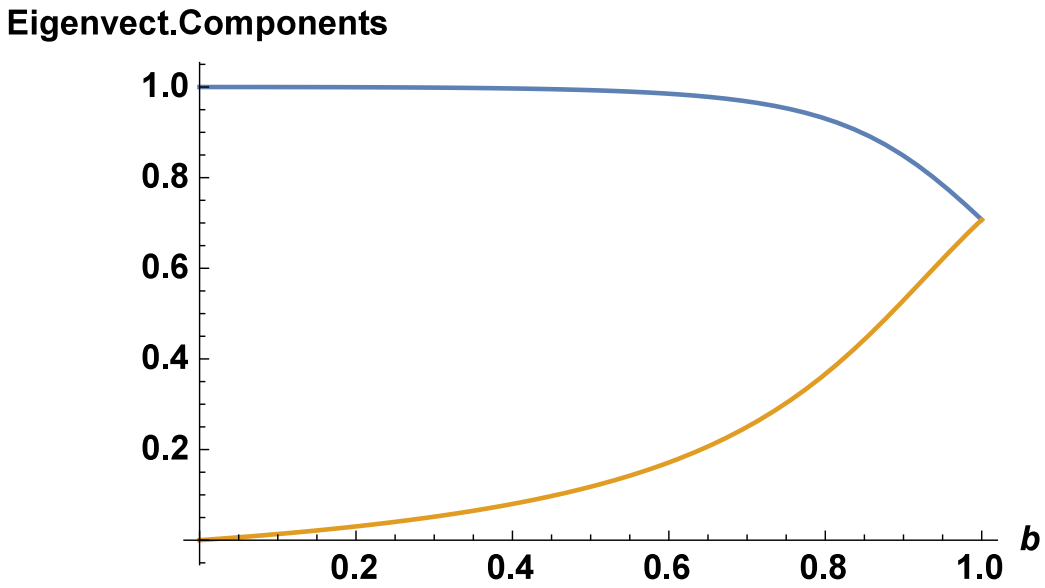

Figure 1.11: Eigenvector components corresponding to the in phase mode, $\omega = 0.7$ MHz, $\omega_1 = 1.5$ MHz. The blue and yellow curves correspond to the amplitudes of motion of the ion 1 and ion 2.

b decreasing, the difference between the motional amplitudes of two ions increases. For example, in Figure 1.11 at b = 0.2, the motional amplitude of ion two equals ≈0.025, whereas motional amplitude of ion one equals ≈1, which means that ion two is hardly involved in the motion.

In case of b = 1, when the two ions have equal masses, they are equally involved in the motion; for the in phase mode the amplitudes are equal to $(\frac{1}{\sqrt{2}}; \frac{1}{\sqrt{2}})$ and for the out of phase motion they are $(\frac{1}{\sqrt{2}}; -\frac{1}{\sqrt{2}})$. One can see that even small deviation of b from unity causes ion to be less coupled to the motional modes. For $^{138}Ba^+$ and $^{171}Yb^+$, b ≈ 0.8, which leads to $(0.9; 0.4)$ in case of the in phase mode.

The analytical approach demonstrated in this section is only valid for two particles. In the case of three or more ions, a numerical approach needs to be implemented. Also, considering the transverse direction of motion in a linear trap, the numbers of modes grow as 2N, where N is the number of ions, which presents a challenge for motional spectroscopy

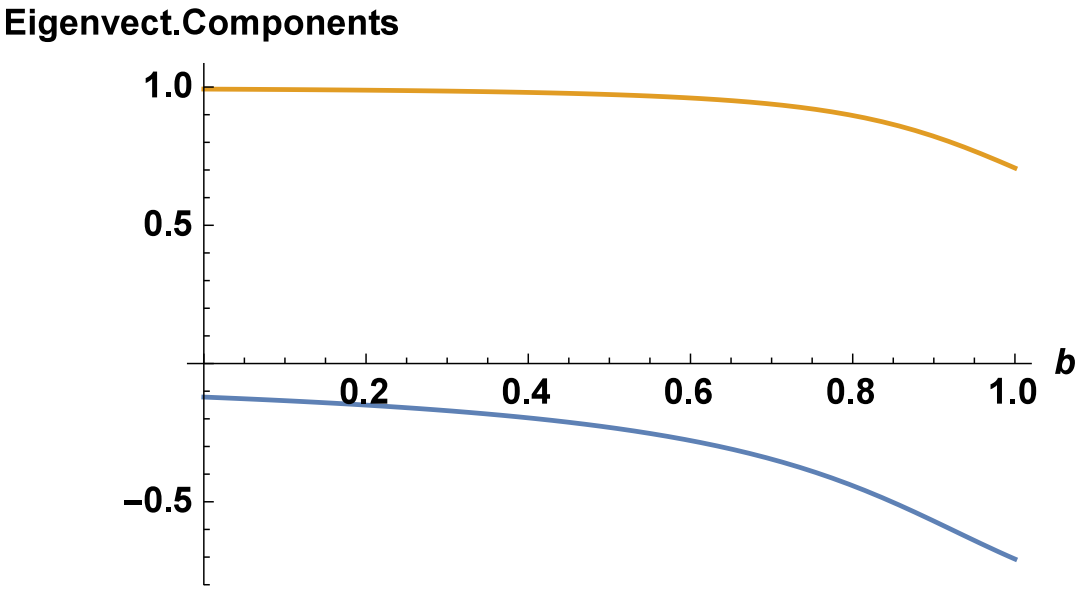

Figure 1.12: Eigenvector components corresponding to the out of phase mode, $\omega = 0.7$ MHz, $\omega_1 = 1.5$ MHz. The blue and yellow curves correspond to the amplitudes of motion for the ion 1 and ion 2.

of hundreds of ions since the spectrum becomes crowded.

Chapter 2

EXPERIMENTAL SETUP AND TECHNIQUES

2.1 Linear RF Trap

The geometry of the ion trap used in this work looks similar to Figure 1.2. The distance between the end-cap needles is 6 mm, whereas the distance between the rods is approximately 800 μm. The diameter of the rods is about 400 μm. All mentioned components are made of tungsten. The voltage can be supplied to each rod and each end-cap needle separately to position ions relative to the RF null (for micromotion compensation [119]) and to move the ion chain axially. These elements are connected to the power supplies by an 8-pins vacuum feed-through. The RF signal amplitude applied to the pair of diagonal rods is about 600 V. All four rods can be connected to the DC power supplies to have more degree of freedom to control ions' position relative to the trap axis. Typical DC voltage applied to the rods to compensate ion's micromotion in this trap does not exceed 500 mV. In order to avoid the RF leakage to the DC power supply, low-pass filters ($\approx$1 MHz) are used. For axial confinement, the voltage in the range of 50-400V can be applied to the end-cap needles. Note that due to the end-cap needles axial misalignment, the change of applied voltage leads to the ion chain axial displacement.

The trap is located inside a vacuum chamber and kept under ultra-high vacuum $\approx 10^{-11}$ torr with a constantly running ion pump and an ion gauge to monitor the pressure. The titanium sublimation pump is also a part of the vacuum system; it is used occasionally (once every couple of months) to remove noble gases. More detailed information about the ion vacuum system can be found in my predecessors' theses [66, 21].

In order to supply a high-voltage radio-frequency signal to the trap, we use a helical RF resonator [29]. This can be seen as a shielded inductor that operates at a certain resonance frequency. For our application, this frequency is in the range of $\approx$10-20 MHz. The helical resonator mainly serves to match the load of the standard 50 Ω impedance of an

RF amplifier and as a band-pass filter. In this work, the quality factor Q of the resonator was ≈150 with a resonance frequency of 18.256 MHz. Note that adding/removing low-pass filters or grounding trap rods affects the resonance frequency. More information about this specific helical resonator can be found here [109].

In this work, the direction of the magnetic field matters. Generally, if no magnetic field is applied, it is still possible to trap ions due to the presence of Earth's magnetic field of ≈ 0.5 Gauss. However, the magnetic field defines a certain quantization axis, which is important for state initialization and spectroscopy. In this work, the magnetic field should be aligned with the 493 nm laser cooling beam, so the main magnetic coil (≈ 40 turns) is placed at 45° to the trap axis along with the cooling and repump laser beams. The other two magnetic coils are used to compensate all magnetic field components that are not aligned with the quantization axis; all three magnetic field vectors are nearly orthogonal. The second magnetic coil (≈ 15 turns) is placed on the top view-port of the vacuum chamber, and the third one (≈ 15 turns) is on the view-port at 90° to the first one. All of these coils are connected to the independent DC current supplies. The magnetic field produced at the trap center is ≈ 3 Gauss.

2.2 Ionization and Isotope Selection

In order to trap ions, first, we need to produce a neutral atomic beam. This is done by resistively heating a small stainless steel tube that contains a sample of metallic barium/ytterbium. A high DC current is applied to the oven that heats the tube to a high enough temperature to emit neutral atoms at the desired rate. In this work, we load both Ba^+ and Yb^+ ions in the same trap. Typical current applied to the Ba oven should not exceed 11-12 A, whereas for the Yb oven, it should not exceed 7-8 A. Higher applied current can cause oven connections failure. For loading ions one-by-one, the applied current should be 2-3 A lower than listed above. When the current source is on and the oven reaches its highest temperature, a slight spike in the pressure reading can be noticed, but it should go back to its initial reading in a minute. A typical rate of ion trapping depends on many factors, not just the intensity of ions flux. If incoming laser beams are aligned optimally, the rate of about ten ions per minute can be achieved at the upper bound of the oven

current. My predecessor, Tomasz Sakrejda, has done all hard work on Ba and Yb neutral atom sources construction; the detailed procedure is well-described here [66, 93].

When sufficient atomic flux is achieved, the next step is ionization. Our research goal requires the possibility to select isotopes. There are many possible ways to remove an electron from the outer atomic shell [56]; two of these methods can be seen in Figure 2.1 that provide isotope selectivity. The method utilizing 337 nm radiation should be avoided if one works with surface-electrode chip-scale trap since electromagnetic radiation below 400 nm can cause ionization of material surrounding ion [43]. This ionization leads to an undesirable stray electric field that causes problems when the ion is $\approx$100 μm away from the trap surface. However, this is not an issue in a macroscopic linear RF trap, and the combination of 791 and 337 nm beams has been successfully used for years to ionize Ba atoms.

The 337 nm wavelength is generated by a Stanford NL100 nitrogen pulsed laser with a pulse length of 3.5 ns and an average power of 3 mW. This is a relatively powerful laser that is used to 'strip' the electron from the $6s6p\,^1P$ state. The repetition rate of these pulses can be adjusted to find a balance between fast ionization and minimization of trap component exposure to UV radiation. An output laser beam has an uneven shape and is about 1 cm in diameter. It is tightly focused by a 25 cm plano-convex lens such that the resulting beam size is comparable to the end-cap needle tip. The maximum possible repetition rate of the laser emission is 20 Hz, whereas the typically applied repetition rate is 5 Hz. Note that long UV exposure still causes a noticeable stray field that can affect laser cooling. It is better to wait and let this stray field decay before collecting data.

The 791 nm laser in this double-stage ionization process ensures isotope selectivity. The 791 nm radiation is generated by a home-made ECDL and provides tunability of $\approx$10MHz. The spectrum of some semiconductor laser diode can have a dispersion of a few nm [4], which is equivalent to hundreds of GHz range and, hence, the diode itself cannot provide isotope selectivity without additional frequency filtering. Moreover, adjusting the current and/or the temperature of the laser diode directly does not grant fine frequency adjustment. The required tunability can be achieved by extending the diode laser internal cavity by adding an additional frequency-selective element such as a diffraction grating. In this scheme, a

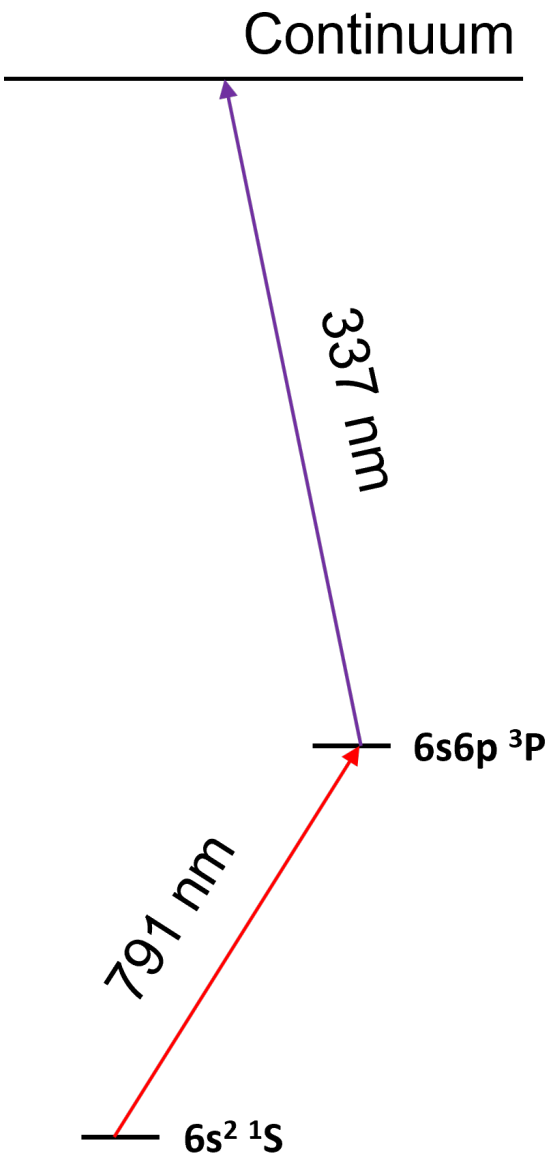

Figure 2.1: The outer electrons states of Ba atom for different ionization schemes discussed in details here [56]. 337, 450, and 791 nm laser emission wavelengths are used to address these transitions.

part of the light is diffracted back to the diode to create an extended cavity between the grating and back facet of the diode. In our setup, we use the Littrow configuration [45], where the diffraction grating can be rotated for fine frequency tuning. The grating provides optical feedback to the laser diode chip. In order to perform fine frequency tuning, the rotation of the diffraction grating is performed by a PZT.

The illustration for frequency selectivity can be seen in Figure 2.2. Intrinsic semiconductor dispersion leads to the broadest gain profile, whereas the external cavity, as expected, has narrower features. The grating serves as a 'sinc-shape' frequency filter to select less than THz range from a periodic gain profile. More details on the origin of this gain profile can be found here [72]. A single-mode operation can be achieved, and it is limited by the selectivity of the external cavity. It is clear that several external cavity modes can have similar gain, which leads to the laser jumping from one cavity mode to another. This is what we often see while working with our 791 nm ECDL. A 'coarse' frequency adjustment can be made by changing the external cavity mode frequencies or the semiconductor profile central frequency in favor of the desired external cavity mode. This can be done in various ways that will be described later.

The ECDL setup for 791 nm light emission consists of several components: the diode laser (Thorlabs L785P090, single-mode 785 nm diode) mounted in a collimating tube, an aspherical collimator (≈6 mm), a diffraction grating, and a PZT. The grating is attached to a mount, which provides vertical and horizontal grating adjustment. The diode emits an elliptical shape beam, a small 'notch' on the diode indicates the junction plane of the laser diode. The collimated beam goes onto the diffraction grating, the 1st order diffracted beam (reference) is directed back to the laser diode, whereas the 0th order diffracted beam is the resulting ECDL output, which is about 80 milliwatts for this particular diode. As one may notice, an initial laser diode central frequency is far off from the desired value. This is not an issue since the diodes have a variation in central frequency ± 3nm; thus, one with the lowest central frequency can be selected. The additional 'coarse' frequency adjustment to get 791 emission can be made by changing the laser diode temperature in the range from room temperature to 70^0C (maximum temperature allowed) without affecting optical alignment. This changes the internal cavity frequency profile. We use LDT-5525B 24W Thermoelectric

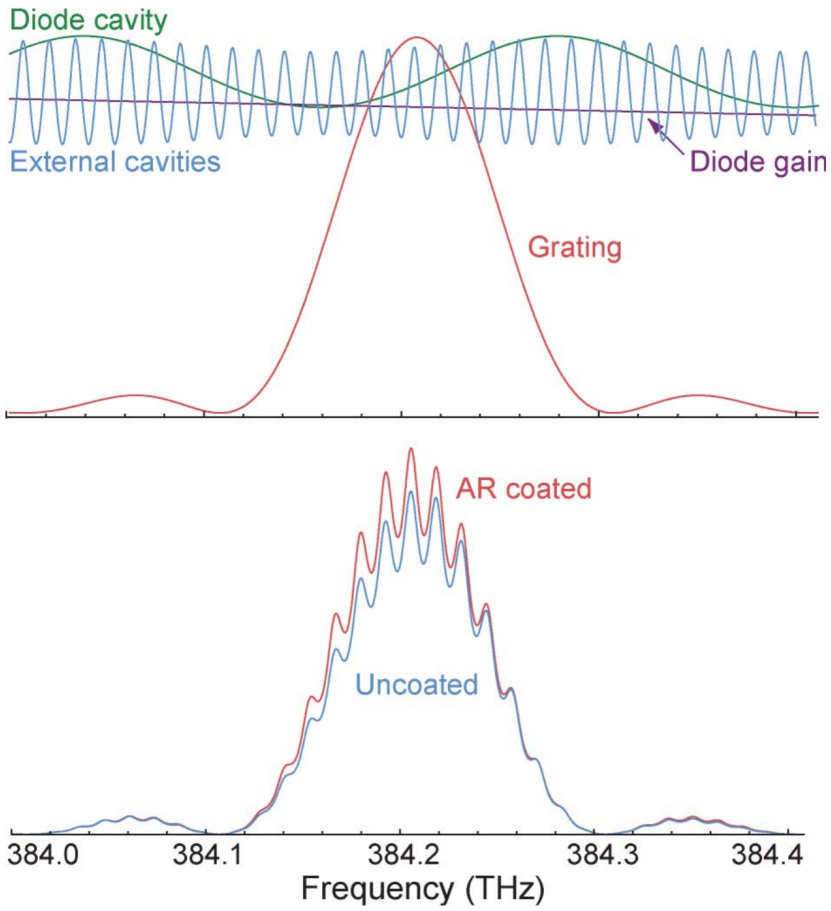

Figure 2.2: Comparison of the diode cavity and the extended cavity gain profiles for a 780 nm diode. For comparison, the selectivity of the diffraction grating (with/without AR coating) is presented. In this example, the grating has 1800 grooves/mm, the extended cavity length is 15 cm, and the internal diode cavity is 0.25 mm long [94].

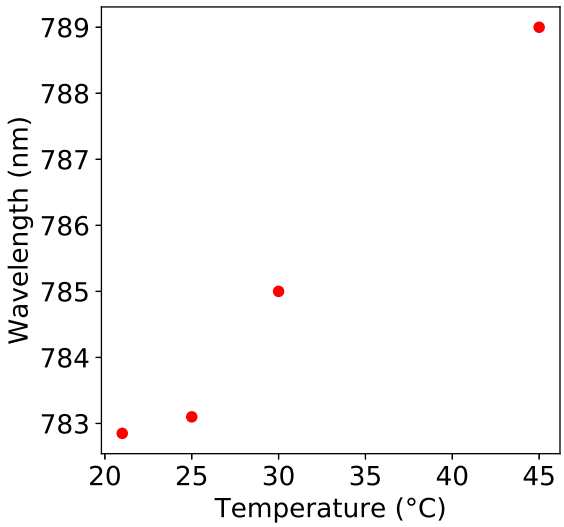

Figure 2.3: Illustration of laser diode emission wavelength vs temperature at constant diode current of 70 mA. The operating temperature of 785 nm diode can go up to 70^{0}C so it provides the tuning range of a dozen of nm. However, not all components of the setup can handle such high temperatures.

Temperature Controller, Newport, that is used for the laser's temperature stabilization; it is typically set at 30°C for the currently used diode. The typical temperature dependence is illustrated in Figure 2.3. Another frequency adjustment is performed by the diode's current control. I found that the current tuning does not provide enough range for the 'coarse' frequency adjustment, and it is not reliable for the fine frequency tuning. The only effect from modest current tuning is increasing/decreasing of the output power. Hence, I usually try to keep the current near the optimal operating current value, which is 120 mA. Finally, fine frequency adjustment $\approx$ 10 MHz can be made by the PZT voltage ranging from 0 to 100 V, provided by the piezo controller. Technically, to ensure the frequency stability during the ionization process, the 791 nm ECDL can be locked to a low-finesse cavity, but I found that the 791 nm ECDL itself performs well. It does not drift significantly in short time intervals ($\approx$ seconds) nor in the interval of the whole trapping process ($\approx$ seconds to 10 min), so there is no need to additionally frequency-stabilizing it. Typically, one milliwatt and a few hundred-micron beam size are enough for efficient ionization. Most of the lasers in the lab are either home-made or Toptica Littrow-configuration ECDLs, so they have similar operating and adjustment procedures.

Loading rates for different Ba isotopes are listed in Figure 2.4, which is taken from [99]. The highest loading rate of $^{138}Ba^+$ is associated with its highest natural abundance of about 71.7%. Luckily, the $^{138}Ba^+$ has the lowest resonance frequency of the $6s^2\ ^1S \rightarrow 6s6p^3P$ transition. By red-detuning the 791 nm ECDL from its resonance transition, the loading rate of the other isotopes can be neglected, and $^{138}Ba^+$ can be trapped solely. The second most abundant isotope that can be trapped with such a scheme is $^{136}Ba^+$, its natural abundance is 7.8%. It is unlikely to trap it unless 791 nm frequency is far off from the resonance. $^{136}Ba^+$ isotopes appear as dark or very dim spots among the bright $^{138}Ba^+$ ions.

Finally, trapping Yb requires a similar scheme (see Figure 2.5). A few milliwatts home-made 399 nm ECDL ensures isotope selectivity, whereas the 337 nm nitrogen laser from the Ba ionization scheme goes for the second stage of the ionization process. In order to reduce the stray field buildup in the trap, a few milliwatts of the 369 nm ECDL (Toptica) for Yb^+ cooling can be used for the second ionization step instead. In this work, we load $^{171}Yb^+$.

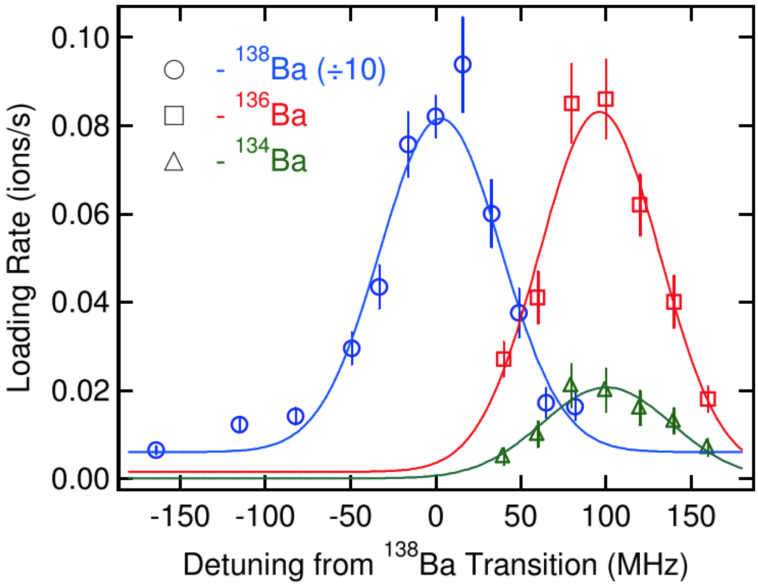

Figure 2.4: Ba^+ isotopes loading rate vs detuning from the $6s^2\ ^1S \rightarrow 6s6p^3P$ $^{138}Ba^+$ transition. $^{138}Ba^+$ has the highest natural abundance, and can be ionized exclusively with high loading rate [99]. Note the different scale for $^{138}Ba^+$ data.

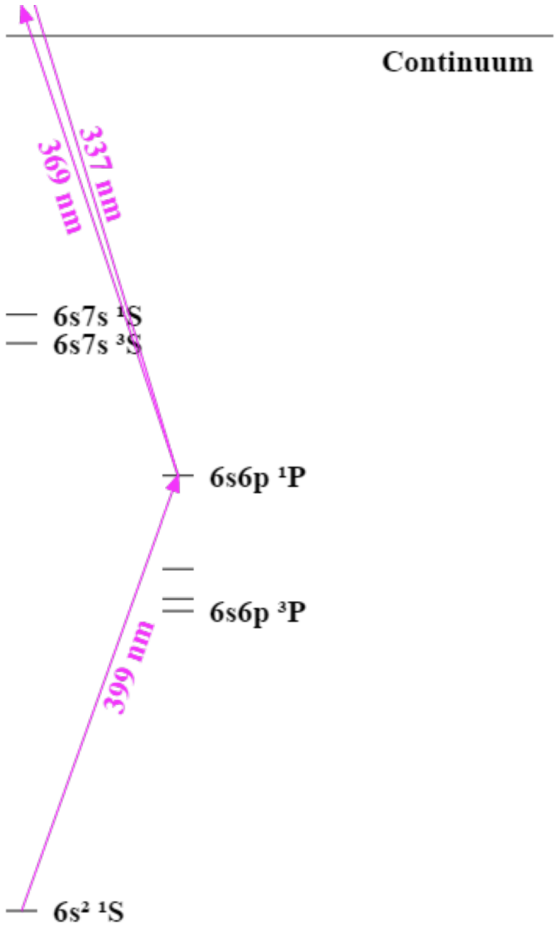

Figure 2.5: The outer electrons states of Yb atom for two different ionization schemes [56]. 337, 369, and 399 nm laser emission wavelengths are used to address these transitions.

For the ytterbium isotopes, natural abundance is quite similar for $^{171}Yb^{+}$-$^{176}Yb^{+}$ so the frequency of isotope-selective laser has to be well-tuned to chosen isotope resonance, which is possible with the presented ionization technique.

2.3 Laser Cooling

In this section, I would like to describe the $^{138}Ba^{+}$ Doppler-cooling procedure and outline the scheme of related setup. As was discussed in Section 1.3.1, Doppler cooling $^{138}Ba^{+}$ requires two laser beams. The 493 nm laser beam provides the cooling force and, due to strong cycling transition, leads to efficient photon scattering. 493 nm photons resonantly scattered by the ions are then collected by the optical system (microscope). Due to the high likelihood of decaying to the $5D_{3/2}$ state, whose lifetime is about 80 seconds, the 650 nm laser, called the 'repump' laser, is used to return the ion back to the cooling cycle. The presence of repump laser and, as a consequence, the third involved transition makes the cooling more complicated. However, as was shown in Section 1.3.1, with the proper detunings and powers of both 650 and 493 nm lasers, temperature of $^{138}Ba^{+}$ can be brought very close to the Doppler limit.

The required fine frequency adjustments can be achieved with ECDLs, whose working principle has been described in Section 2.2. We use 650.7 nm and 986.7 nm Toptica ECDLs with ≈100 mW output power. Half of the 650 and 986 nm laser power is sent to the double-pass AOM systems setup and then to the corresponding optical cavities for frequency stabilization (see Section 2.5). Then, 986.7 and 650.7 nm are sent to the single-pass AOM systems, where the 1st order diffracted beams are sent to the trap, and non-deflected beams are sent to the wavemeter for the frequency reading. Hence, it is important to subtract AOM's modulation frequency to be able to get reliable wavelength reading. Both beams can be turned on/off by switching the RF signal applied to the SPAOM by using TTL RF switches. The on/off switch time is less than 1μs and is suitable for most of our purposes. After single-pass AOM, the 986.7 laser beam is sent to the frequency-doubling waveguide based on potassium niobate crystal $KNbO_3$ that produces the 493.4 nm light. It is important to keep the frequency-doubling crystal at a certain temperature (T = 32.6^{o}) to maximize the output of the 493.4 nm light. Then, the 493.4 and 650.7 nm beams are combined using

a dichroic mirror and coupled to the same single-mode optical fiber. A 15 cm plano-convex lens is used to focus collimated 493.4 and 650.7 nm beams to the trap center. The maximum power that can be sent to the trap is 30 μW and 200 μW for 493.4 and 650.7 nm light, respectively. It is mostly limited by the efficiency of coupling to the single-mode fiber, and, in the case of 493.4 nm, it is limited by the output power of the frequency-doubling crystal.

The outline of our setup is shown in Figure 2.6. Both the 650 and the 986 nm beams first go through the optical isolators to avoid reflected beams going back to the laser diodes. Then they go through the anamorphic prism pairs to make the beam's shape circular. Next, HWPs are used to adjust the ratio of the power going to the DPAOMs and to the trap/wavemeter through PBSs that create two beam paths. Beams that go through DPAOMs are physically separated from the incident beams in the plane perpendicular to the optical table. It allows to pick off the double-passed beams with mirrors (M1 and M2) and send them to the Cavity 1 (650 nm) or Cavity 2 (986 nm). Note that M1 and M2 are set lower in the plane perpendicular to the optical table relative to the beams incoming from the diode lasers. In order to convert 986 nm into 493 nm, the 986 nm goes through the doubling crystal. After passing SPAOM and the doubling crystal, 650 and 493 beams are combined and sent to the trap. Here we omitted some optical elements related to polarization for efficient optical pumping; that will be discussed in the next section.

In this work, we do not Doppler cool ytterbium ions. However, we have a setup for Doppler cooling $^{174}Yb^{+}$ ions; this includes a Toptica 369 nm ECDL for cooling as well as a home-made 935 nm ECDL for repump.

2.4 Wavelength Meter and Frequency Calibration

The ability to perform accurate frequency measurements is crucial for working with atomic systems. In ion trapping, frequency reading is required at all stages, such as ionization, cooling, and qubit operations. Here we perform frequency measurements with a High Finesse WS7-60 wavelength meter. It has an absolute accuracy of 60 MHz and a high measurement speed to constantly monitor frequencies of CW lasers such as 791, 650, and 986 nm. One laser at a time can be monitored, but it is relatively easy and fast to switch between channels.

When ions need to be trapped and cooled during a long run of data taking, the waveme-

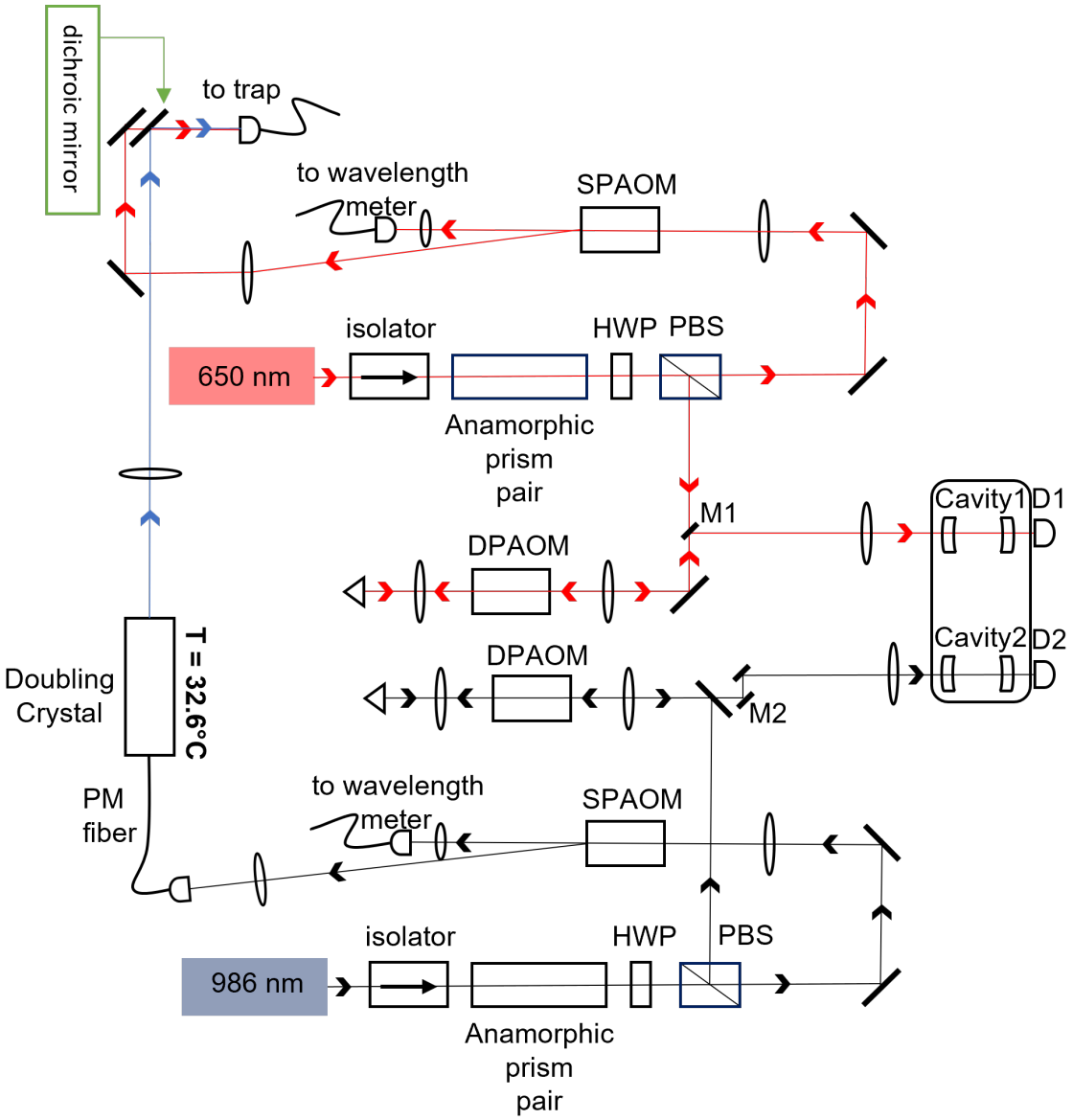

Figure 2.6: The outline of 986 and 650 nm lasers setup. Note that M1 and M2 are set lower in the plane perpendicular to the optical table relative to the beams incoming from the diode lasers.

ter performance might be important. It is known that parameters such as temperature, humidity, etc., affect the wavemeter reading due to their effect on the optics the wavelength meter is made of. We have a day-to-day room temperature fluctuation of about 1^oC due to the daily shut down of the AC system in the building. The internal wavemeter's temperature controlling unit is not capable of properly stabilizing the temperature; eventually, the wavemeter adapts to the room temperature. We performed a set of measurements to indicate how the change of room temperature affects the reading short-term. A stable HeNe laser (632.8 nm) from a Burleigh WA-1650 wavelength meter was plugged into our WS7-60 wavelength meter. The HeNe laser frequency had been monitored while the inner WS7-60 wavemeter temperature reading was being taken. The internal temperature stabilization was turned off. The data has been collected for 50 minutes; see Figure 2.7. The overall temperature change was 0.7^oC, while the frequency reading difference between the maximum and the minimum value was 75 MHz. This deviation of HeNe frequency is within the wavemeter's accuracy.

It is not necessary to get accurate measurements of atomic transition frequencies, but it is crucial to maintain a reliable reference for day-to-day operations. Usually, trapping ions and monitoring ionization, cooling, and repump laser frequencies are the best way to keep track of the long-term change (if there is any) and establish references. If the readings seem to be way off, it is likely that some wavemeter parameters need adjustment. This can be done by re-calibration. The wavemeter measurements strongly rely on applied calibration, which is done with a stable, high-accuracy HeNe laser or any atomic reference. In Prof. Subhadeep Gupta's lab, Yb transition frequencies can be used as a reference. In a vapor cell, Yb $^1S_0 -^1 P_1$ transitions can be addressed with 399 nm light, and the frequency of 399 nm laser can be fine-tuned for each isotope. Some portion of 399 nm light with known frequency tuned to the transition of selected Yb isotope [28] is sent to WS7-60 wavelength meter, and the calibration is performed. The stable HeNe laser from the Burleigh WA-1650 wavemeter can be used for calibration as well. Note that changing the calibration wavelength will change the WS7 frequency reading somewhat. Hence, it is better to use the same calibration wavelength.

In conclusion, it is realistic to use the WS7-60 wavelength meter for the CW laser

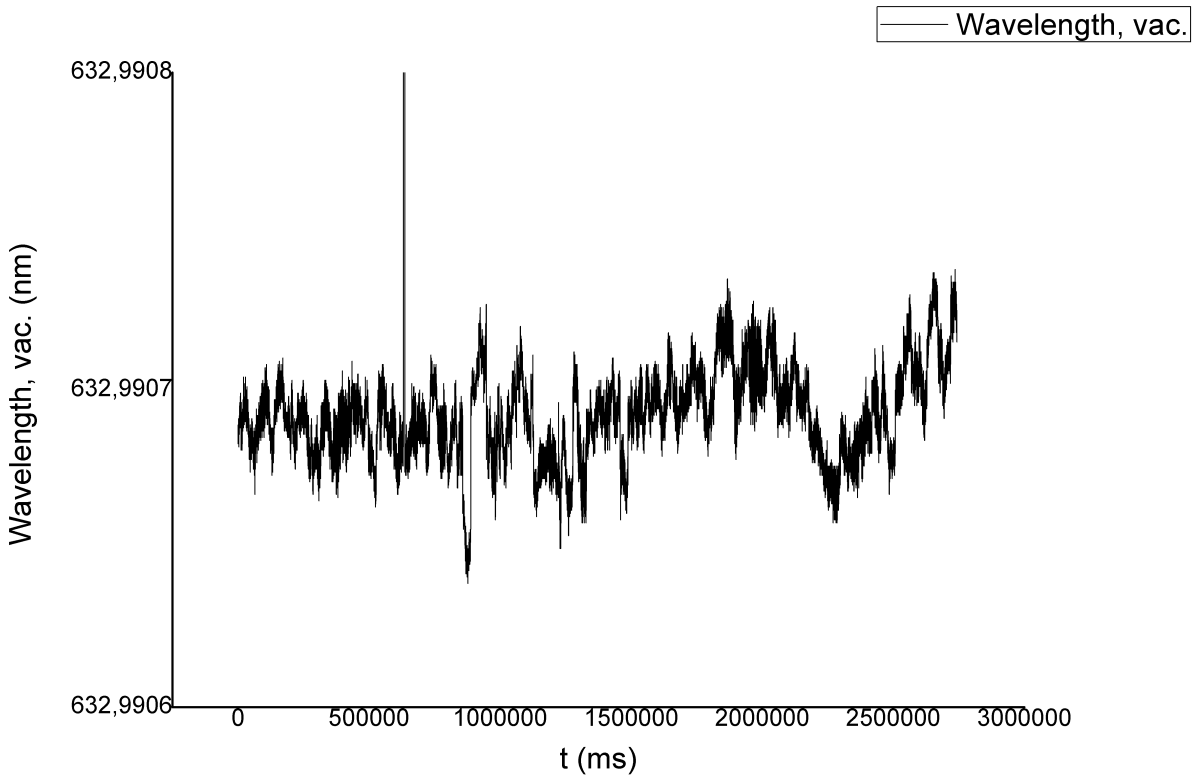

Figure 2.7: Continuous measurements of a stable HeNe laser wavelength over 50 min while the internal wavelength meter's temperature stabilizer was turned off. The 'spike' on the graph corresponds to the short system shut down and was excluded from the analysis.

frequency reading. It has shown good performance even without internal temperature stabilization, and it is possible to have reliable references for 493, 650, and 791 nm frequencies over a long period of time.

2.5 System for Cooling and Repump Lasers Frequency Stabilization

As described above, the wavelength meter provides reliable frequency measurements. However, its accuracy is not enough for any kind of frequency stabilization of the cooling or repump laser since the addressed transition linewidth is typically $< \sim$100 MHz. The cool-

ing or repump outputs themselves have good short-term stability, but data-taking can take more than a few hours, and the central frequencies of the laser drift ∼100 MHz during this time period. This can significantly affect the Doppler cooling efficiency as well as ion's fluorescence rate.

In order to stabilize frequencies of the 493 and 650 nm lasers, we use low-finesse optical cavities as references. The reason for choosing low-finesse over mid- or high-finesse is relative simplicity to couple light into such cavities. Moreover, the broad cavity 'fringes' of the transmission signal make the side-of-the-fringe lock procedure easier. Of course, we do not aim to narrow the laser spectrum but rather to maintain the same central frequencies for the period of data taking.

Part of the 986 and 650 nm beams are sent to the reference cavities. We aim to use the cavity's longitudinal modes and monitor the transmitted signal (see Figure 2.6). This signal from the cavity depends on the wavelength of the incident beam; the transmitted signal has a peak when an integer number of wavelength fits within the length of the cavity L (standing waves). The two cavities are made of concave dielectric-coated mirrors separated by ∼8 cm. These mirrors have non-zero curvatures (R_1 and R_2 for the first and the second mirrors, respectively), so the resonance condition becomes [86]:

$$\nu_{snm} = \frac{c}{2L}\left(s + \frac{1}{\pi}(m+n+1) + Cos^{-1}\left(\sqrt{\left(1-\frac{L}{R_1}\right)\left(1-\frac{L}{R_2}\right)}\right)\right) \tag{2.1}$$

Where s, m, and n are the mode numbers that can take only positive integer values, and c is the speed of light. $R_{1,2}$ can be positive/negative for concave/convex mirrors. The ν_{snm} are the only frequencies that can exist inside the resonator.

The longitudinal, or TEM_{00} modes occur when m = n = 0. This happens when the wavefronts of the incident Gaussian beam match with the mirror surfaces, and the beam is aligned to the optical axis of the cavity. In this case, the beam profile of the transmitted signal is a Gaussian shape as well. The frequency separation between two adjacent TEM_{00} modes ν_{s00} and ν_{s+100} is called the free spectral range of the resonator:

$$\nu_{FSR} \equiv \nu_{s+1,0,0} - \nu_{s,0,0} \tag{2.2}$$

The finesse of the resonator characterizes its performance. The higher the finesse, the narrower the peaks are and the higher the frequency resolution. Define Γ^{FWHM} as the full width at half maximum of each cavity peak. Finesse F depends on the reflectively r of the mirrors; for two mirrors with identical reflectively:

$$F = \frac{\pi\sqrt{r}}{1-r} = \frac{\nu_{FSR}}{\Gamma^{FWHM}} \tag{2.3}$$

Parameters of the optical cavity listed above are sufficient to design the resonator with chosen finesse for different types of laser locking techniques and purposes. In our case, the finesse of the 986 nm cavity is ≈ 20 with FSR = 1.5 GHz and $\Gamma^{FWHM} \approx 75$ MHz. The 986 nm cavity transmission as a function of the laser frequency is shown in Figure 2.8. The laser frequency is scanned over the 1.5 GHz range by modulating the PZT voltage in the laser.

The main function of the laser-lock system is to provide the output signal to, in our case, the PZT or any other transducer that controls the diode laser parameters. In the case when the frequency is a controlled parameter, the output of the laser-lock system forces the diode laser output frequency to the desired value regardless of any external perturbations. The difference between the actual frequency and the desired frequency is called the error signal. The PID parameters of the laser-lock system regulate the response based on the input error signal.

There are two methods to lock the laser using an optical cavity transmission peak as a reference; the side-of-fringe and the top-of-fringe locking methods. The side-of-fringe locking method uses the slope on either side of the transmission peak (negative or positive slope), such that frequency fluctuations cause amplitude fluctuations on the photodetector and, respectively, the error signal changes. Assuming that the laser-lock system responds fast enough to any perturbation, the only limitation is the minimum achievable error signal, which is determined by the internal electric noise, background light, etc. In this work, we use the side-fringe locking method with one of the Toptica PID modules, PID-100, to lock the 986 nm laser. The schematic of the setup is shown in Figure 2.9. Some portion of the laser power is sent to the DPAOM and to the cavity. The transmitted signal from the cavity

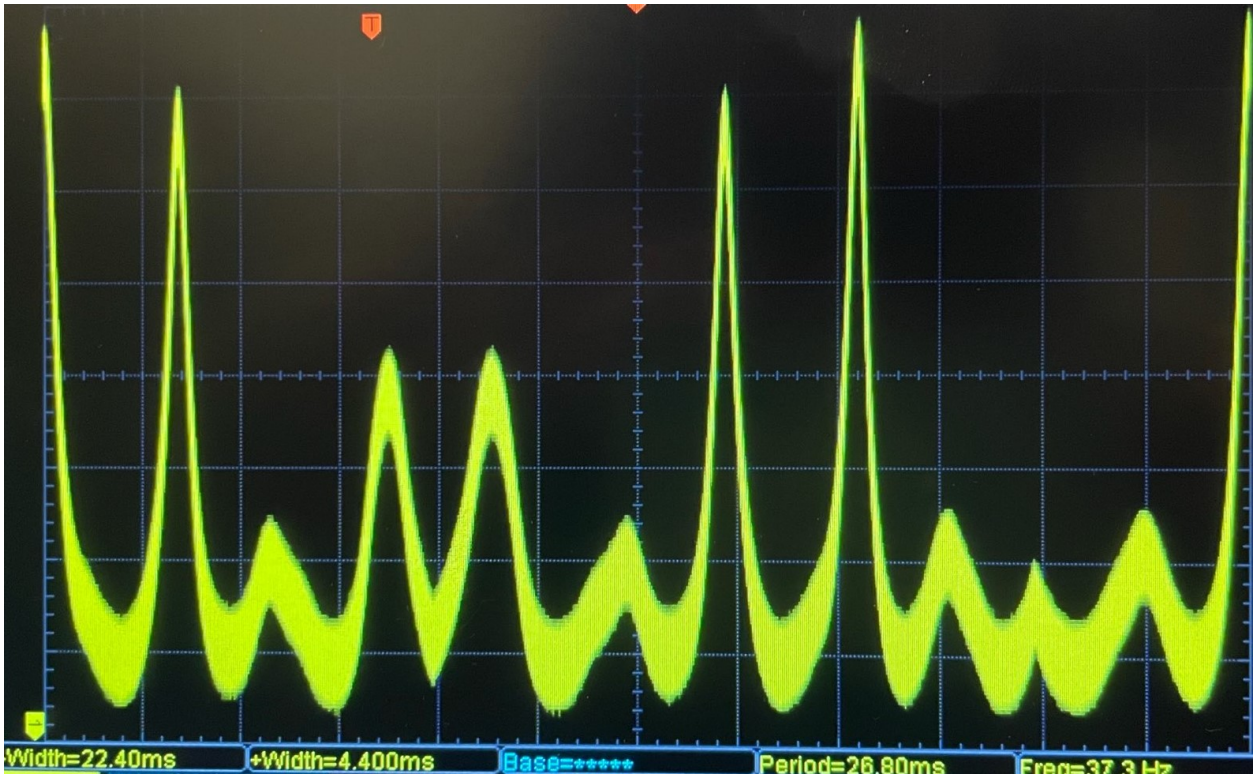

Figure 2.8: The 986 nm cavity transmission as a function of the 986 nm laser frequency. Periodic modulation of 986 nm diode's piezo voltage resulting in frequency sweep of ∼1.5 GHz. This corresponds to the cavity FSR since one can see transmitted patterns reproducing.

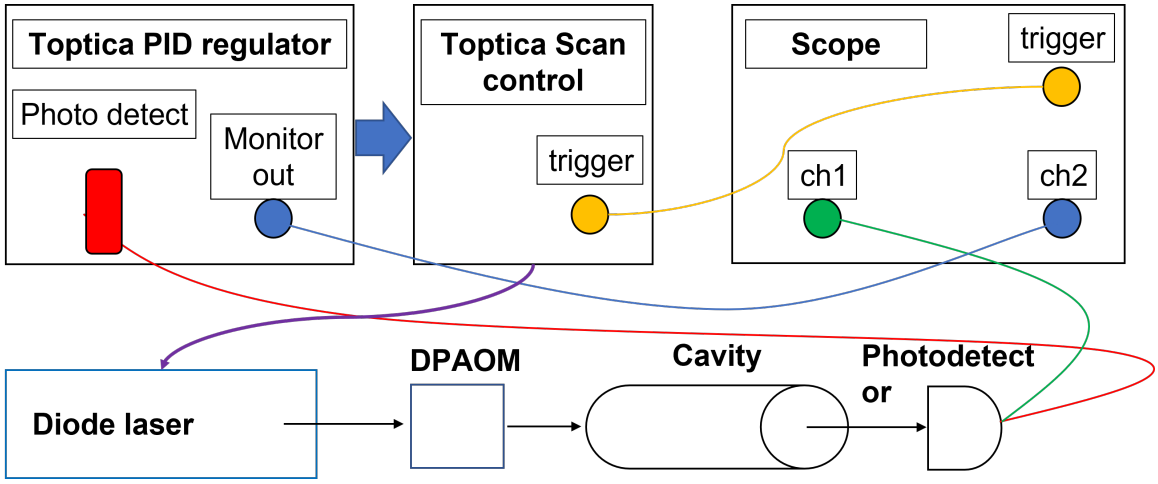

Figure 2.9: Schematic representation of the 986 nm laser-lock system for the side-of-fringe method. The laser is sent through DPAOM for fine frequency adjustment without disturbing the beam path. Then the beam is coupled to the cavity, where the transmission signal is observed with the photodetector. From the photodetector, the signal is sent to the oscilloscope for monitoring, as well as to the PID regulator to produce the error signal. There is an internal connection between the PID regulator module and the Scan control module so that the resulting control signal is sent directly to the laser PZT - this is a benefit from using products from the same company.

is monitored with the Thorlabs PDA55 photodetector. This signal is sent to the oscilloscope for monitoring and to the Toptica PID regulator input ('Photo detect'). The error signal can be monitored ('Monitor out') and minimized by adjusting PID parameters and set point as well as the slope on the transmission peak. Fine frequency adjustments can be made by changing the modulation frequency sent to the DPAOM without changing coupling to the cavity. Both the 650 and 986 nm cavities are located in the vacuum chamber under $\sim$1 torr (see Figure 2.6) and are temperature stabilized. A similar side-of-fringe locking method is used for the 650 nm laser with a New Focus LB1005 High-Speed Servo Controller instead of the Toptica PID-100 regulator.

The locking bandwidth of the current system can be estimated using the information

about the transmission peak one locks to and the resulting minimum error signal. In our case, the minimum error signal (ΔA) is ∼400 mV whether the pk-pk amplitude of the transmission peak is 1.2 V (A), and its linewidth is ∼75 MHz ($\Delta\omega$). Hence, the resulting locking bandwidth is ($\Delta\omega_e$):

$$\Delta\omega_e = \frac{\Delta\omega}{2}\frac{\Delta A}{A} \approx 7.5\ MHz \tag{2.4}$$

Note that by adjusting the DPAOM frequency, the cavity temperature, laser power, sign of the slope, or by locking to another transmission line, the 'local' slope corresponding to the lock points can change drastically. This significantly affects the performance of the side-of-fringe locking method. For all future experiments, I suggest moving to another method.

The top-of-fringe locking method doesn't have any of the issues described above since the error signal is not susceptible to the laser amplitude noise. It requires superimposing RF modulation current onto the laser diode DC-supply current. This can be done by installing a Bias-T PCB to the diode. By directly modulation diode current and an additional PD detector module (Toptica), the top-of-fringe locking method can be applied. The scheme is illustrated in Figure 2.10. PD detector outputs 20 MHz sidebands to the Bias-T and results in desired phase modulation. The top-of-fringe locking method is more robust than the side-of-fringe method, especially in the case of the cavity temperature drift.

2.6 Optical System for Ion Imaging and Improving Image Quality

When ions are trapped and cooled, they undergo strong cycling transitions and emit photons at the rate of $\approx 10^7/s$ (see Section 1.3.1 for details). These photons can be collected, and a diffraction-limited image of an ion can be obtained. In most of my work, I needed to spatially resolve the image of the trapped ions. For this case, I used either EMCCD or TimePix3Cam single-photon sensitive camera. When the image of trapped ions is spatially resolved, one can select the ROI where each ion is located to detect each ion qubit state.

State-dependent fluorescence is used to detect trapped-ion qubit state. It relies on a standard 'bright/dark' discrimination procedure that requires collecting photons from chosen ROI. Typically, photons are collected in a defined time interval called acquisition or

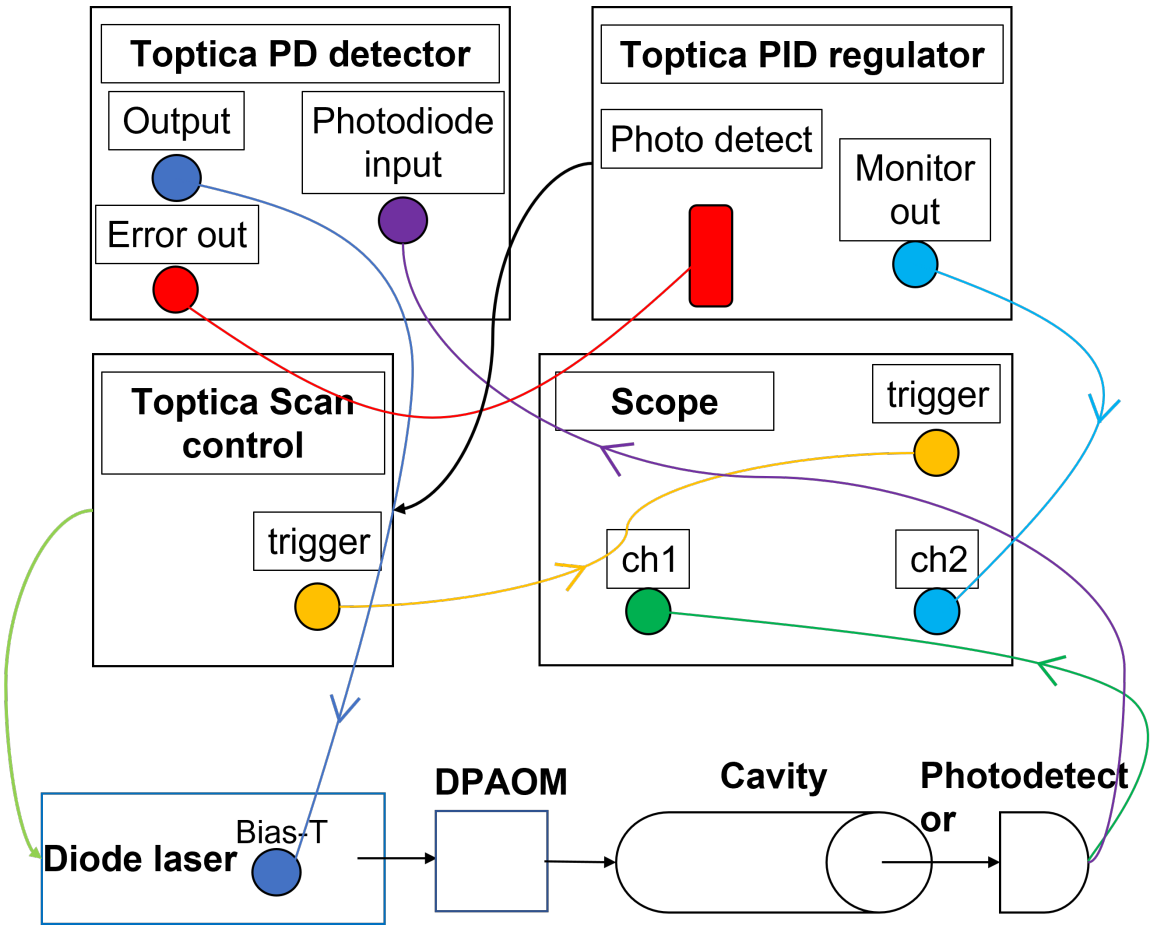

Figure 2.10: Schematic representation of the 986 nm laser-lock system for top-of-fringe method. The laser beam is sent through DPAOM for fine frequency adjustment without disturbing the beam path. Then the beam is coupled to the cavity, where the reflected signal is observed with the photodetector. From the photodetector, the signal is sent to the oscilloscope for monitoring as well as to the PD detector to produce the error signal. Toptica PD detector has an oscillator with 20 MHz output that is applied to Bias-T for phase modulation. The error signal is then sent to the PID regulator. There is an internal connection between all listed Toptica modules.

integration time. In the next few paragraphs, we will discuss the optical setup for photon collection from ions(s) and issues I have been facing with the image quality.

In this work, the optical system consists of 6 main components: a vacuum view-port, an objective lens, an adjustable aperture, a doublet lens, an interference filter, and a detection system. The most recent setup is shown schematically in Figure 4.8. For the detection, the TimePix3Cam camera with the intensifier was used. Instead of this camera, the PMT or EMCCD can be placed. In this setup, fluorescence from ions passing through the vacuum viewport is collected by the objective lens, through the adjustable aperture, and further magnified by the doublet lens. A 493 nm interference filter is used to reduce the background. Finally, the 493 nm fluorescence is imaged onto the detection system. This system acts as a microscope; the magnification of the ions' image can be varied by changing the doublet lens focal length or by changing the position of the detection system. The first stage of this microscope consists of the objective lens, and the rest of it is referred to as the second stage. The objective lens is the main stage for collecting photons. We use an objective camera lens: a 50 mm Nikon lens with a numerical aperture of 0.20. The second stage has an adjustable aperture to filter out stray light. Then, there is and a home-built 25 mm doublet lens. The total magnification of the system is approximately 45.

The performance of the optical system is important to discriminate each ion qubit state with low error. The main parameters contributing to the optical system performance are collection efficiency and the optical crosstalk between ions. To minimize the optical crosstalk, the image quality needs to be improved so that the image of the ions is close to the diffraction-limited performance.

2.6.1 Diffraction Limit

Even if no aberration is present, the ion image has the minimum size due to the diffraction on the spherical aperture. These diffraction patterns are spherically symmetrical and their radial size is determined by the NA of the microscope aperture. The diffraction pattern irradiance I(r) in the case of a uniformly illuminated circular aperture is:

$$I(r) = \frac{A\pi}{\lambda^2(f/\#)^2}\left[2j_0\left(1, \frac{\pi r^2}{\lambda f/\#}\right)\right]^2 \tag{2.5}$$

where f/# is the ratio of the system's focal length to the diameter of the entrance aperture, λ is the wavelength of the incident monochromatic light, A is the total incident power, j_0 is the 0th order Bessel function, and r is the radial distance from the center of the diffraction patterns. Because of the spherical symmetry, this problem can be represented as one-dimensional.

The diffraction patterns in the case of a diffraction-limited image for the optical system described above are presented in Figure 2.11. The diffraction pattern between two the zero-intensity regions is known as the Airy disk. In the case of a perfect optical system, the amount of energy contained within the $\approx 2\mu$m diameter Airy disk in the object plane is about 84%. Optical crosstalk between neighboring ions can be calculated as the power 'leaking' from one ion to the ROI corresponding to the neighboring ion divided by the total power 'stored' in this ROI. If the spacing between ions is 5μm and the selected ROI centered at ion's position is 2x2 μm^2, resulting optical crosstalk from one neighboring ion is 0.06%.

In reality, irradiation beyond the Airy disk becomes significant due to the imperfection and aberrations of the optical system and/or optical alignment, which leads to the larger crosstalk.

2.6.2 Spherical Aberration, Defocus, and Coma

Initially, experiments on ion's state discrimination were conducted with a single plano-convex lens with NA of 0.2 as the first stage of the microscope. The main problem with this setup is the low image quality due to the spherical aberration caused by the singlet lens and, hence, high optical crosstalk. A typical image of the ions with this setup can be found here [93]. It is easier to produce a spherical shape lens, but the further away the incident beam is from the center of the lens, the more it 'bends' and deviates from the optical axis. It can be shown that the radial deviation ϵ of a ray entering the lens with the radius of curvature of R, parallel to the optical axis, is:

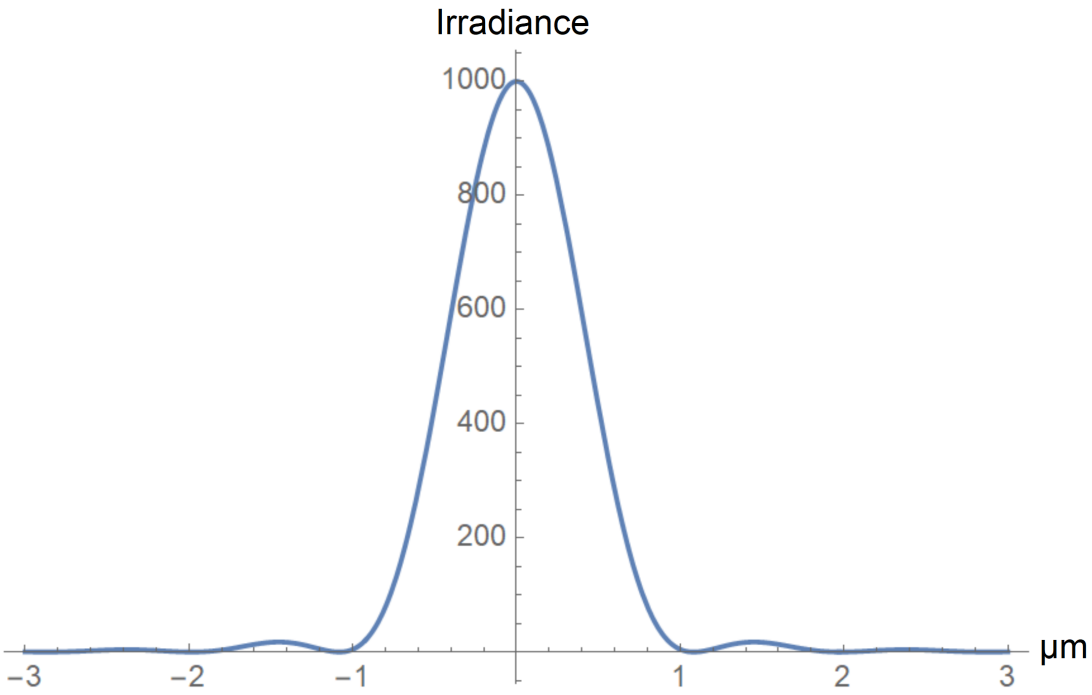

Figure 2.11: Diffraction patterns (1D) of a circular aperture (f/# is 1.8) for wavelength of 493 nm and the total incident power of 1000. The magnification of the optical system is 45.

$$\epsilon \sim \frac{h^3}{R^2} \tag{2.6}$$

Where h is the, height the ray is hitting the lens. An important note here is that the transverse aberration scales with $\frac{h^3}{R^2}$. This implies that increasing the diameter of the lens increases the effect of spherical aberration. One can notice the effect of spherical aberration by observing relative asymmetry of the right defocus image vs. the left defocus image.

Technically, this problem can be solved by decreasing the NA of the lens by, for example, placing a smaller aperture in front of it. There were a few attempts to do that, and the results are shown in Figure 2.12. However, this significantly reduces the collection efficiency, which affects the detection fidelity and forces us to increase the acquisition time for the state readout. Another solution is to use a high a NA aspherical lens. An aspherical lens with NA of 0.1 one that is suitable for our system (available for purchase from Thorlabs) has a very narrow working distance range (∼1mm) and requires a shorter distance (∼40mm) between the viewport and the trap for adequate operation.

The next common problem with the ion image is the coma. The coma occurs when some of the optical elements are off-axis. A distinctive feature of the coma is image elongation in one direction, similar to the images shown in Figure 2.12 (A). In order to properly align the optical system and minimize the coma, I disconnected the second and the first stage of the microscope setup to add an extra degree of freedom to place all elements on the same optical axis. In order to adjust the angle, the objective lens mount can be tilted as well; this and the translation of the first stage relative to the second one helps with 'merging' the optical axes.

It is important to understand how the diffraction patterns change in the case of spherical aberration and defocus. Apart from visual recognition of the flaws in the optical setup, this helps to perform a quantitative analysis. The wavefront emerging from the lens/system of lenses is rather complex. However, a well-assembled setup has only a few noticeable well-recognized patterns corresponding to different types of aberrations. Mathematically, this can be described as a wavefront expansion as the power series in the four coordinates, such as the two exit aperture coordinates and the two paraxial image coordinates. Considering

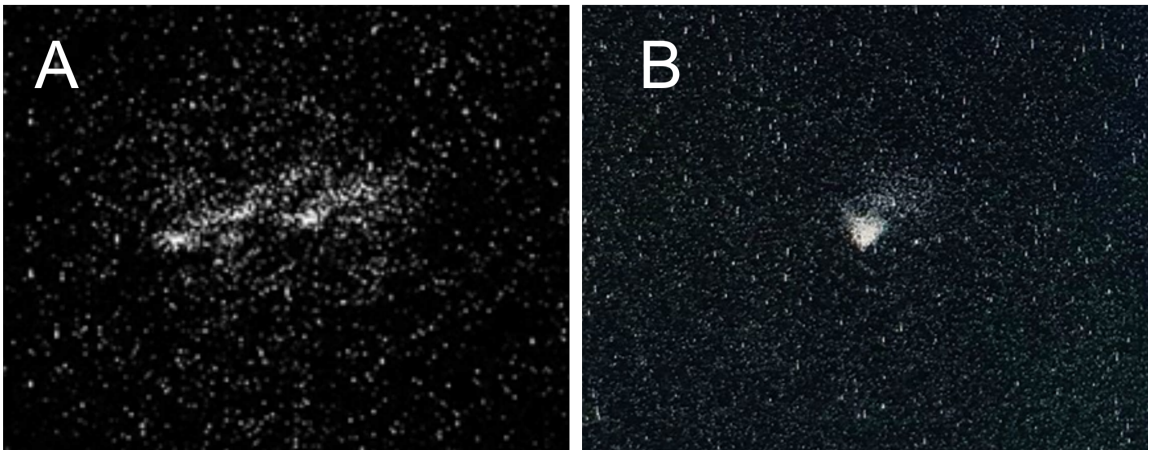

Figure 2.12: Ion(s) image with a single plano-convex lens [93]. A) Image of two ions representing severe spherical aberration and coma. B) Image of one ion when a smaller aperture was placed on the top of the vacuum chamber's viewport in front of the objective lens. The coma was reduced as well by moving the second stage of the microscope relative to the first stage.

rotational symmetry about the axis of the light propagation, this expansion takes a form stated by Welford in 1974 [107]. Normalized polar coordinates are used to rewrite the wavefront expansion. Defocus and spherical aberration are spherically symmetric aberrations corresponding to $\sim \rho^2$ and ρ^4 terms in this expansion, where ρ is the position on the aperture. Coefficients W_{020} and W_{040} in front of ρ^2 and ρ^4 terms represent the severity of the aberration and the defocus. In case of these types of aberration, the irradiance (Eq. 2.5) transforms into:

$$I(r) = \frac{A\pi}{\lambda^2(f/\#)^2} \left| \int_0^1 S(\rho) j_0 \left(0, \frac{\pi r}{\lambda(f/\#)}\rho\right) \rho \, d\rho \right|^2, \tag{2.7}$$

Where

$$S(\rho) = exp\left[i\frac{2\pi}{\lambda}\left(W_{040}\rho^4 + W_{020}\rho^2\right)\right]. \tag{2.8}$$

Here, ρ is a normalized radial coordinate that is equal to 1 at the edge of the aperture,

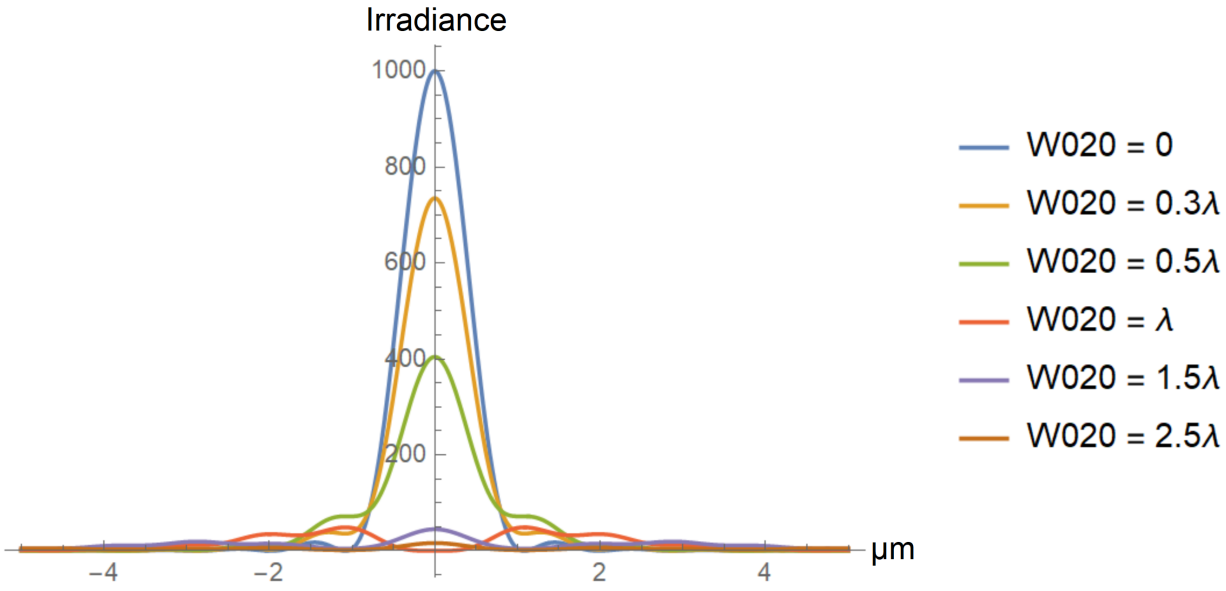

Figure 2.13: Irradiance in the presence of defocus.

$r = \sqrt{x^2 + y^2}$ is the radial image coordinate, A is the total power, the rest of the parameters were defined previously.

In figures 2.13 and 2.14 one can see the effect of defocus and spherical aberration on the ion's image quality. The redistribution of the irradiance over the larger area leads to higher crosstalk between ions and, consequently, to the low ion's state detection fidelity. The effect is more pronounced when two of these optical system's flaws come into play. As an example, in figure 2.15 one can see the combined effect of 0.3λ defocus and 0.4λ spherical aberration; the irradiance at the center of the image is more than ten times smaller than in the pure diffraction-limited case.

After somewhat successful attempts to compensate spherical aberration and coma with the methods described above and trying to achieve the best focus, the result can be seen in figure 2.16. This is not the diffraction-limited case, but the qubit state readout can still be performed with reasonable integration time and high fidelity, see Sections 3 and 4.1. In order to understand what stands in our way to diffraction-limited image, I decided to

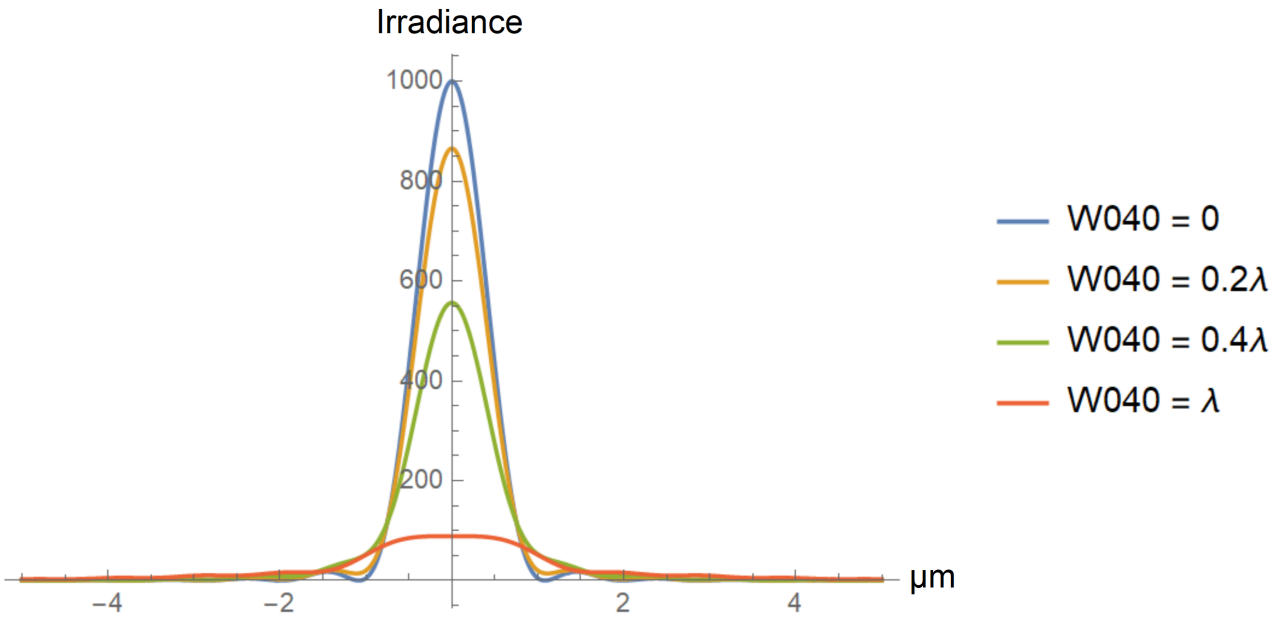

Figure 2.14: Irradiance in the presence of spherical aberration.

simulate the imaging optics and look at the output image of the point source. It turned out that Zeemax is a great tool to do this; the next paragraph is dedicated to it.

2.6.3 Zeemax for Optimizing Imaging Setup

Zemax is software that helps us simulate the impact of each optical element on the final ion's image. Customized optical elements can be placed in Zemax's optical system layout. In figure 2.17 one can see a two-stage microscope comprised of a double-Gauss objective lens and a doublet secondary lens. Zemax traces rays from point sources to the image plane.

First of all, we tried to reproduce the simplest case of aberration. We introduced point sources that are off-axis, which ideally should lead to coma. The offset was ≈0.5 μm. The location of the rays on the image plane can show how the position of the point source can affect the image, see Figure 2.18. A good indicator of the quality of the point source image, in this case, would be an RMS image spot size. Using optimization in Zemax, one can customize the optical setup to achieve the smallest image spot size (or other chosen

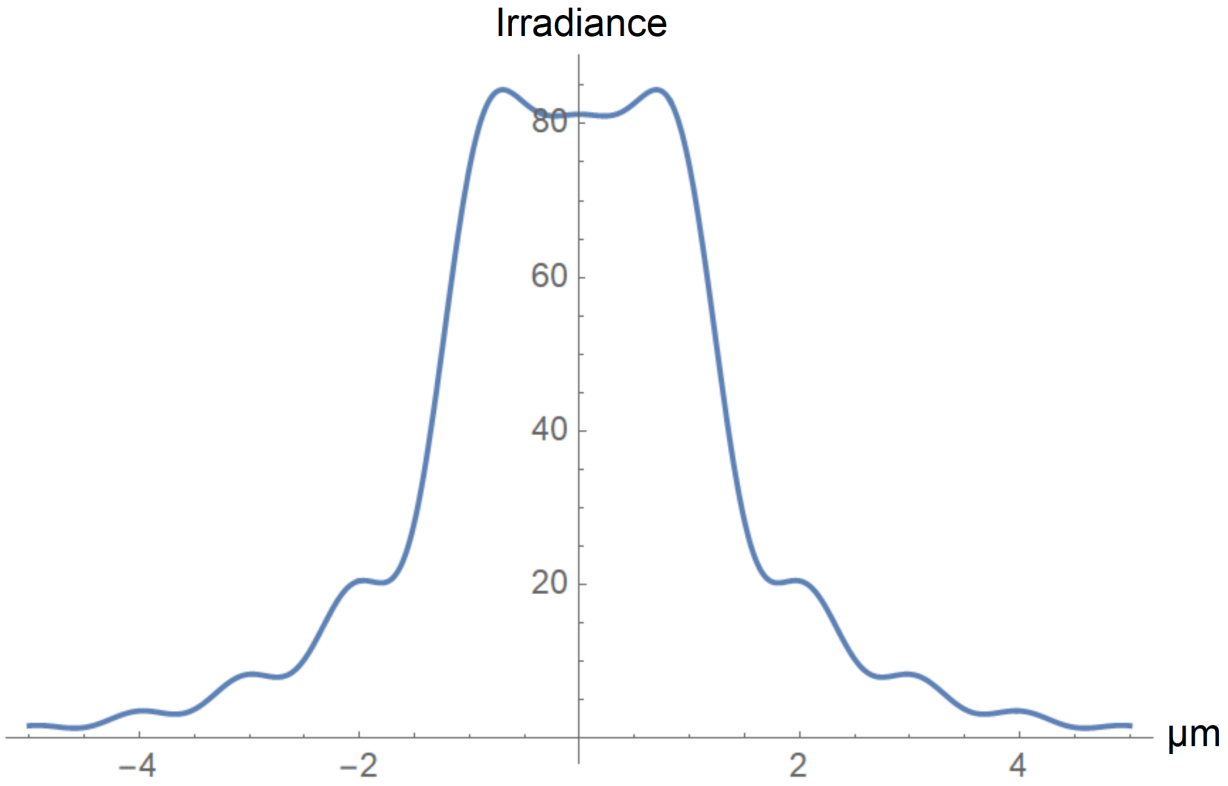

Figure 2.15: Irradiance in the presence of spherical aberration (0.4λ) and defocus (0.3λ).

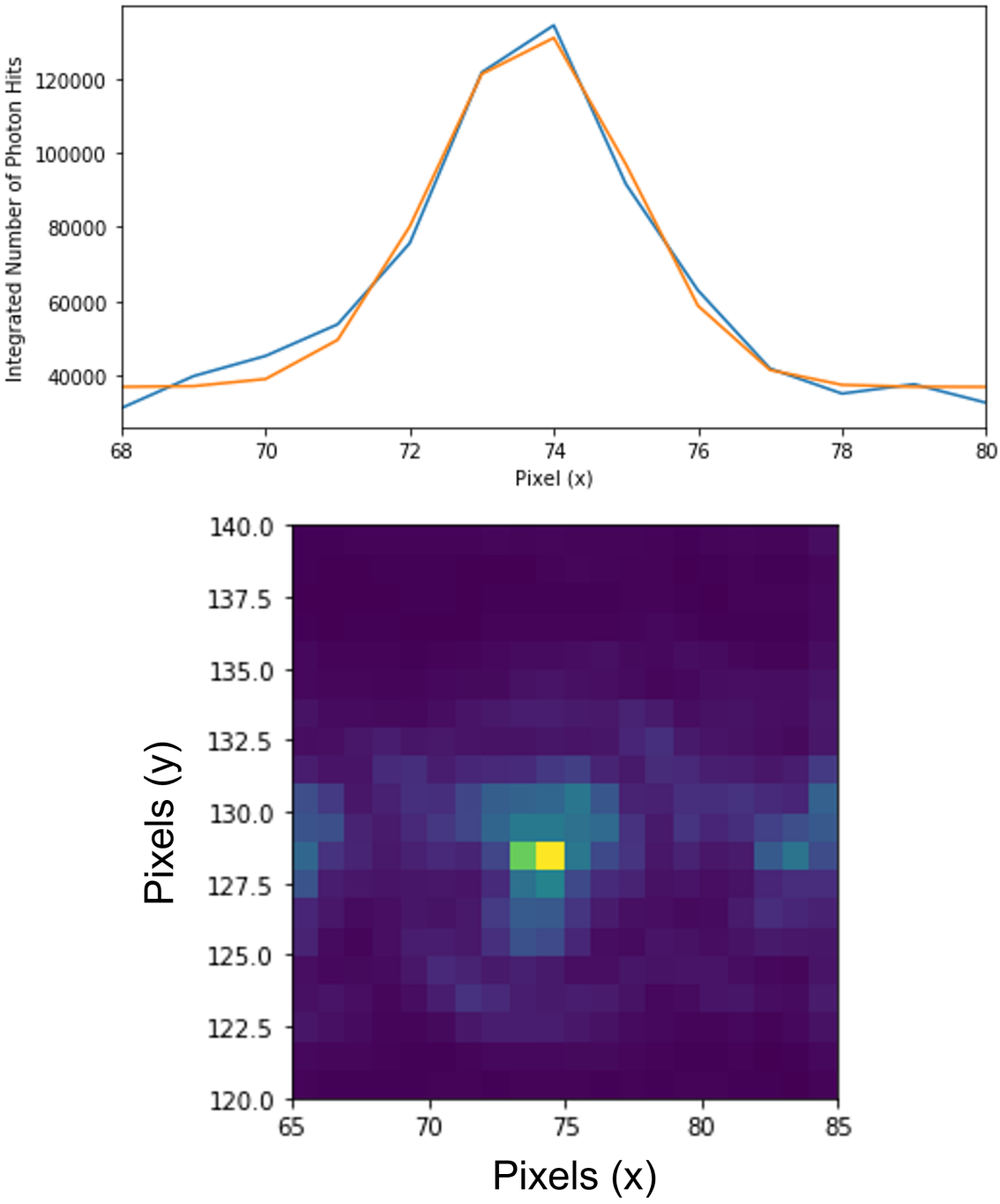

Figure 2.16: Top: the 1D profile of the ion image surrounded by neighboring ions using TimePix3Cam camera (0.9 pixel = 1 micron). Blue and Orange curves correspond to the data and Gaussian fit, respectively. Bottom: image of the ion. The diffraction patterns can be seen, but the first disk is larger in size than in the diffraction limited case, see figure 2.11.

parameters). Optimization in Zemax means minimizing the so-called Merit function. The Merit function takes a set of variables (distances between objects, lens curvatures, and thickness, etc.) and returns a real, non-negative number. The smaller the number returned by the merit function, the better the system meets the goal. Finding a suitable optical system design depends in large part on how well the merit function is set up. In our work, we mostly used the 'spot size' merit function for the optimization.

Another common parameter to quantify the performance of the imaging system is the Strehl ratio. In the case of a truly diffraction-limited image, the Strehl ratio is 1. An optical system with a Strehl ratio larger than 0.8 is considered to be diffraction-limited. We tried to optimize this parameter; however, it turned out that our computation time exceeds limits even for a small number of optical objects. What we did instead of it is demonstrating how the point source displacement affects the Strehl ratio, see figure 2.19. In this figure, we consider a double-Gaussian lens with NA of 0.18 and no viewport; the image stays diffraction-limited at the displacement close to 0.3 mm. However, if the viewport glass is present, this number reduces to less than 0.02 mm. This observation tells us that the glass viewport drastically affects the quality of the image. Moreover, introducing more complexity to the optical layout to get closer to the real setup may enhance this effect. There may be no possibility to meet such constraints while aligning the optical system. Perhaps the effect of the viewport and the restraint it creates can be compensated. Zemax would be a perfect tool to study this further.

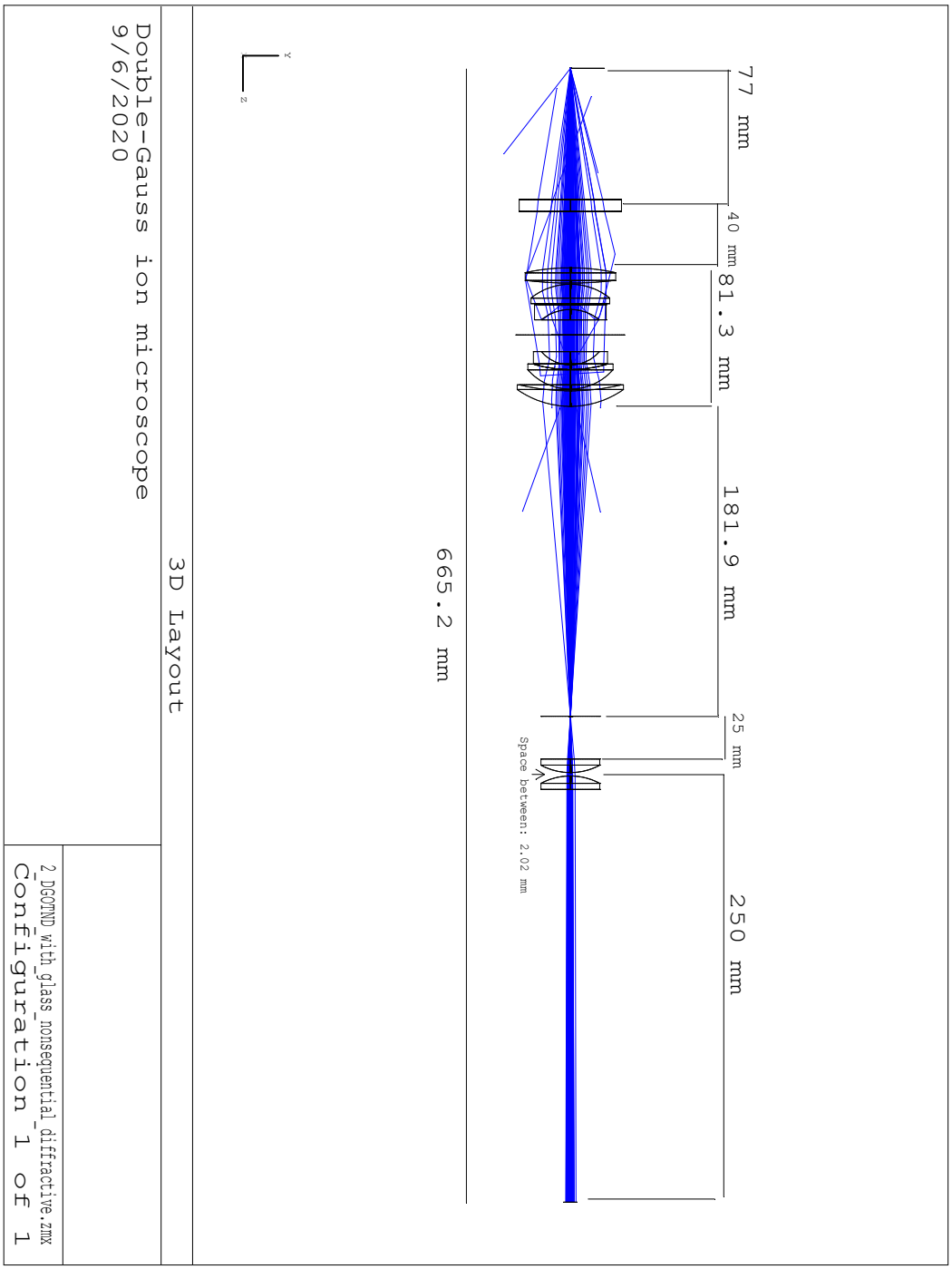

Figure 2.17: Current optical system layout in Zeemax. Five objects presented here: a point source (an ion), viewport glass, a double-Gauss lens (consists of multiple elements), an iris, and a doublet lens. Credits: Kurt Delegard.

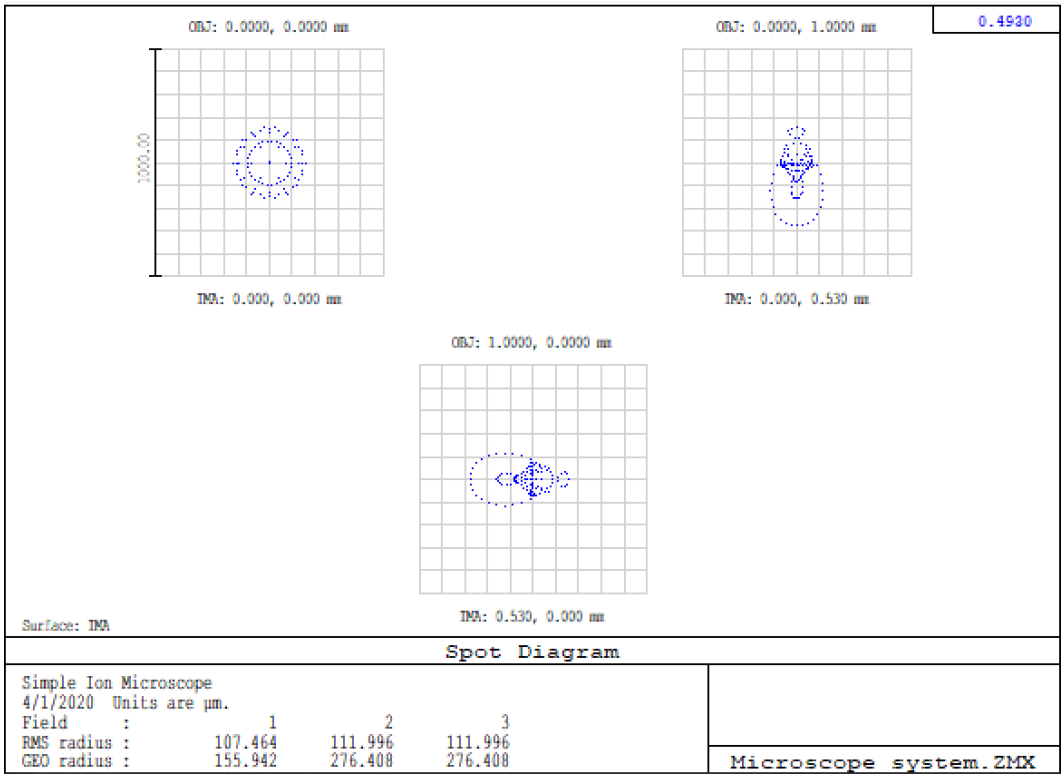

Figure 2.18: The location of the rays from the point source on the image plane. The top left figure demonstrates a point source being on the optical axis. The top right and bottom figures represent the point source offset by ≈ 0.5 μm from the optical axis along different axes, which leads to image distortion related to coma. Credits: Kurt Delegard.

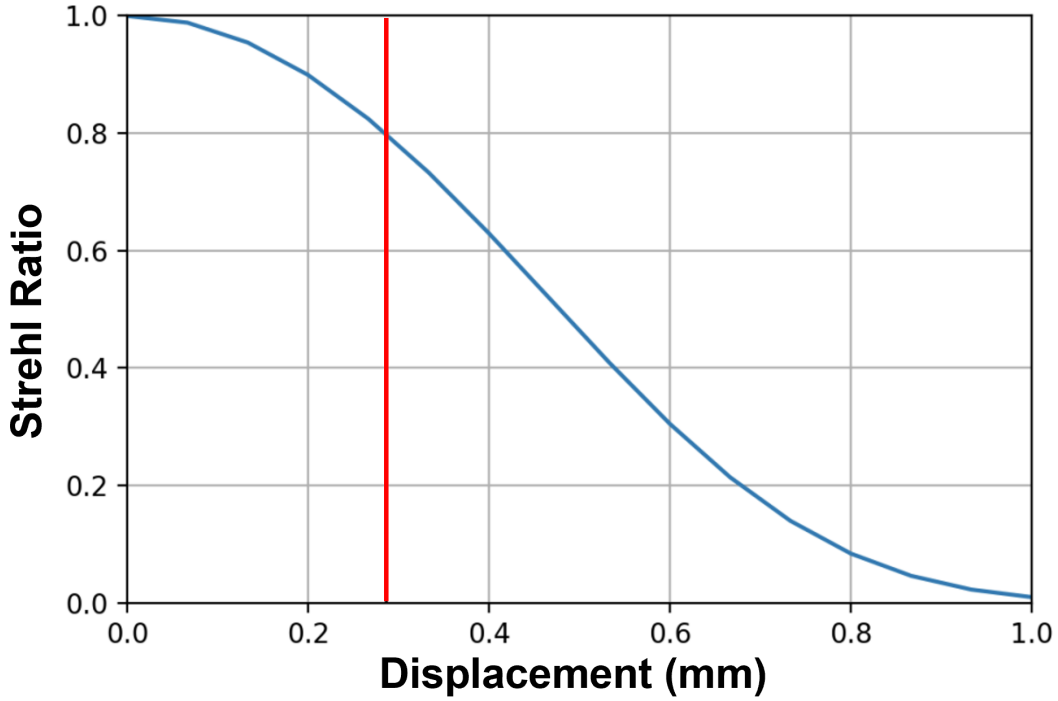

Figure 2.19: Strehl ratio vs. the point source displacement off the optical axis. The diffraction-limited case (Strehl ratio > 0.8) is 0.3 mm with NA $= 0.18$ (see vertical red line) and no glass viewport in front of the first stage microscope objective.

Chapter 3

SYMPATHETIC COOLING OF MIXED-SPECIES BA-YB ION CHAIN

3.1 Motivation

The biggest challenge for trapped-ion-based platform is scalability. Currently, there are two approaches to address this issue. One of them is a modular trap architecture where all ion-trap modules are connected via photonic links [75]. Another approach limits the quantum interactions to multiple small ion crystals in a cryogenic surface trap and includes physical splitting and rearranging those crystal into new crystals, where further interaction occurs [37]. Both of these methods require mixed-species chain because single species trapped ion quantum processors run into several difficulties. First, most high-fidelity Coulomb gates with ions require to keep the ions to be cold [25]. This is not possible with a single species during the crystal transport from the 'state preparation' trap module to the 'readout' module because cooling of these species will interfere with the information encoded in the qubit. Similar issue occurs when photonic link interferes with the information stored in the the neighboring qubits. For example, in some architectures, Bell-measurement schemes are used for entanglement between separate ion traps [73, 75]. These schemes involve repeated excitation of some of the ions in the chain with intense, resonant laser pulses, which leads to decoherence of the neighboring ions. To avoid these complications, mixed-species chains of the trapped ions can be used [20]. In a mixed-species scheme, one ion type can be used as the "utility" species, while the other as the "logic" species. The former is used for cooling the entire ion chain and establishing the remote entanglement, and the latter is used for the quantum information storage and manipulation.

Same-element mixed species schemes using differing isotopes have been proposed [91, 100, 15], but off-resonant scattering of the cooling laser light by the logic species is significant [36], so using different elements is preferable [39]. However, if species of two different

elements are used, the large mass difference can cause the normal mode couplings to become small. This effect has been demonstrated in Section 1.5 on the example of two ions with different masses. Repeating this procedure in the case of more Ba and Yb ions lead to the same trend. Weak coupling of the normal modes impairs sympathetic cooling and entanglement swapping [112]. Barium (Ba) and ytterbium (Yb) atomic ions represent a promising choice of the "utility"/"logic" ion pair. Their relative mass difference is fairly small at approximately 25%. However, as shown in [112] and in Section 1.5, even this small mass difference is sufficient to potentially significantly reduce the radial mode coupling. Thus, a careful experimental study of the regimes that influence modes' coupling is justified.

For scaling to larger trapped ion quantum processors, radial modes are preferred to axial modes for local gates [69, 118]. Using these modes offers several advantages: higher frequencies allow faster gate speeds, performing operations with lasers perpendicular to the ion chain axis makes it easier to address single ions, and gate infidelity due to the ions' thermal motion is reduced by a factor up to $(\frac{\omega_r}{\omega_a})^6$, where the ω_r is the radial center-of-mass (COM) mode frequency, and ω_a is the the axial COM mode frequency [12]. Unfortunately, in the case of mixed species chains radial modes' coupling is small for typical trapping parameters due to the species' mass difference [112]. This coupling can be characterized by the largest eigenvector component for each species in a given mode, $\max(\beta_{ij})$, where β_{ij} is the eigenvector component of the jth ion in the ith mode. The coupling is important for cooling, as the rate of sympathetic cooling scales as $\max(\beta_{ij})$ [59].

In this chapter, I demonstrate efficient sympathetic cooling and good radial vibrational mode coupling in four-ion barium-ytterbium ion chains confined in a linear RF trap [38]. Analytical approach for four ions chain presents difficulty, but measuring four ions chain temperature using one of the ion as a thermometer, is doable. We use the barium ion as a thermometer and as a coolant ion and we find that the coupling for each normal mode depends strongly on the trap aspect ratio. In the strongly coupled case, the measured mode temperatures are consistent with the Doppler cooling limit, while in the weakly coupled case they are one to two orders of magnitude higher.

3.2 Theory

In the mixed-species ion chain only one ion species undergoes direct laser cooling operations. The second species is cooled by the collective motion of the whole chain. Thus, sufficiently strong coupling of the second species ions to all normal modes of motion is necessary for efficient sympathetic cooling. The strength of the ions' coupling to the motional modes is characterized by the normal modes vectors' components, which can be numerically calculated. The cooling rates of each radial mode of our mixed barium-ytterbium ion chain may be calculated analogously to [112]. For Doppler cooling, the cooling rate of the ith mode is:

$$\frac{dE_i}{dt}\Big|_{cool} = \hbar k^2 \cos^2\theta \frac{I}{I_0} \frac{2\Delta\Gamma}{(1 + I/I_0 + (2\Delta/\Gamma)^2)^2} z_i^2 \beta_{ij}^2 \omega_i^2, \tag{3.1}$$

where k is the wavevector, θ is the angle between the wavevector and the mode axis, I and I_0 are the laser and saturation intensities, Δ is the detuning, Γ is the linewidth, z_i is the normal mode amplitude, and ω_i is the secular frequency for that mode.

The average occupation number for each radial mode can then be determined from a steady-state equilibrium condition between the heating and cooling mechanisms. When external heating is low and photon recoil dominates, the Doppler limit might be achieved. The estimated heating rate of a single ion $\dot{\bar{n}}$ due to the absorption and emission of the 493 nm photon is of order 10^5 quanta/second for the secular trap frequency of 1 MHz. The measured external heating rate of a single ion in our trap when cooling lasers are shuttered is of order 2500 quanta/second, which is smaller than diffusion heating.
In the opposite case when external heating due to random electric field fluctuations of the patch potential on the trap electrodes dominates [92], photon heating can be neglected. Ignoring a summation over the eigenvector components which is of order unity for our chains of up to 4 ions, the temperature limit for a given radial mode can be written in terms of the normal mode occupation number as:

$$\bar{n}_i = \max_{\beta_{ij}} \frac{q^2 S_E \Gamma (1 + (2\Delta/\Gamma)^2 + I/I_0)}{16\beta_{ij}^2 |\Delta| \hbar^2 \omega_i k^2 \cos^2\theta \, I/I_0}, \tag{3.2}$$

where S_E is the spectral noise density in the trap at the ion site, and q is the charge of a single ion [112].

In our experiments we extract chains' radial motional occupation numbers by measuring the strength of the $\Delta n = 1$ radial motional sidebands of Ba^+ narrow $6S_{1/2} - 5D_{5/2}$ "shelving" transition near 1762 nm (see Figure 3.1), relative to the strength of the carrier transition. The Rabi frequency Ω_{ij} for the $\Delta n = 1$ sideband of ith normal mode for the jth ion in the chain is:

$$\Omega_{ij} = \sqrt{n_i + 1}\beta_{ij}\eta_i\Omega_j, \tag{3.3}$$

where n_i is the radial motional occupation number for the ith mode, η_j is the Lamb-Dicke parameter, and Ω_j is the carrier Rabi frequency (we allow for spatial dependence of the carrier Rabi frequency due to variation in the laser's beam intesity). Each ordering of ions has a different normal mode decomposition, with both different eigenvectors and different frequencies, so a particular order is maintained for the full duration of an experiment.

To extract the average occupation numbers of different radial modes in the ion chain of N ions, we calculate the transition probability P_j for ion j using the Rabi frequency from eqn. 3.3, and sum over over both the full occupation number distribution and over all radial normal modes in the spectrum. Assuming a thermal state, we have:

$$P_j = \sum_{i=1}^{2N} \sum_{n_i=0}^{\infty} \frac{1}{\bar{n}_i + 1} \left(\frac{\bar{n}_i}{\bar{n}_i + 1} \right)^{n_i} \sin^2(\Omega_{ij} t/2), \tag{3.4}$$

where $\bar{n}_i$ is the given mode's average occupation number and t is the 1762 nm laser exposure time.

To estimate normal mode occupation numbers, we calculate the vibrational mode structure of our chains. We numerically calculate the normal mode frequencies and eigenvectors for each unique ordering of the ions in the chain. To find the radial normal modes frequencies we first consider only the axial direction (z-axis). We minimize the potential energy of the ions to find the equilibrium ion positions in axial direction assuming x and y position of the chain to be zero. One might worry about incorrectly restricting the chain to one dimension, but we can observe and avoid the zig-zag transition in our calculation because it is marked by the softening of the lowest transverse vibrational mode to zero frequency. Once we find the equilibrium positions, we expand the full trap potential around these

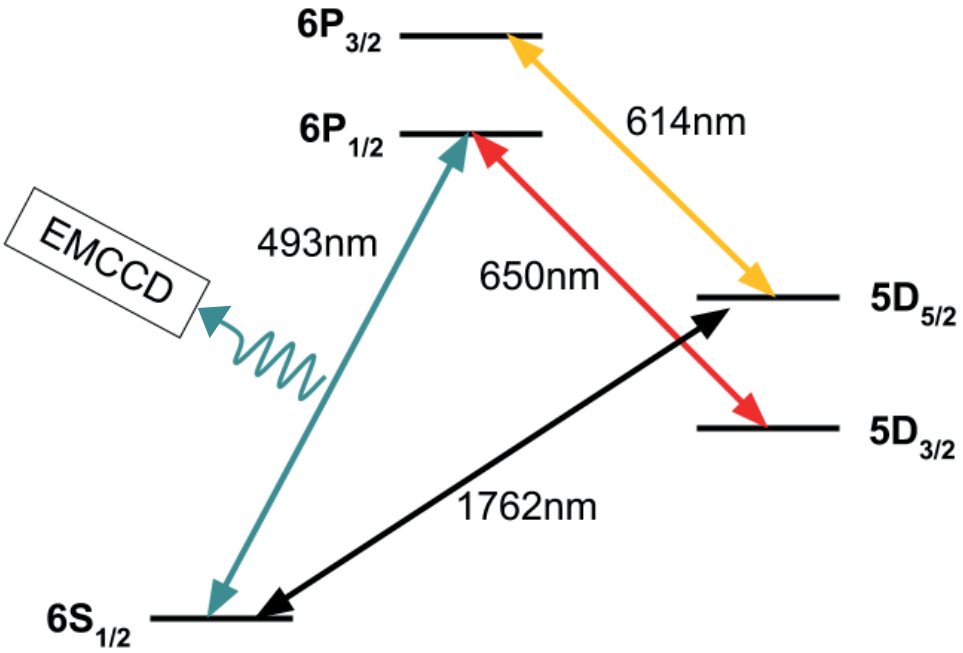

Figure 3.1: (Color online) Ba^+ energy level diagram. The 493 nm fluorescence from the ions is imaged onto the EMCCD camera. The ion decays from the $6P_{1/2}$ excited state to the $5D_{3/2}$ metastable state with a branching fraction of 0.25, and the 650 nm is used to quickly repump from this long-lived state. The 1762 nm laser coherently drives the ion into the $5D_{5/2}$ state where it is "shelved" and does not participate in the cooling cycle. The 614 nm laser is used to quickly de-shelve the ion.

equilibrium ion positions to find the normal mode frequencies and eigenvector magnitudes.

An example of the numerical calculation for the eigenvector magnitudes as a function of the trap aspect ratio in a chain of two barium and two ytterbium ions is shown in Figure3.2. Here the chain order is Ba-Yb-Ba-Yb (BYBY), and we plot the eigenvector magnitudes for the second barium ion x-direction (see Figure 3.2,a). The strong dependence of the normal mode coupling on the trap aspect ratio can be seen. The eigenvector magnitudes approach 0.5 (which, for a four-ion chain, corresponds to the maximum coupling) when aspect ratio decreases. The same trend is seen for ytterbium ions. The table in Figure 3.2,b summarizes

the eigenvector magnitudes of the first ytterbium ion and the second barium ion in the BYBY ordering for the trap aspect ratios of 2.9 and 5.5. These numerical results lead to the important conclusion: better coupling can be achieved by lowering trap aspect ratio. Thus, measuring radial mode occupation numbers at different trap aspect ratios is of interest.

3.3 Apparatus, and Experimental Procedure for Motional Spectroscopy

The mixed species chain measurements are carried out in a linear RF trap similar to that described in [32]. Species-selective photoionization techniques are used to load both $^{138}Ba^{+}$ and $^{174}Yb^{+}$, where barium is Doppler cooled on the $6S_{1/2} - 6P_{1/2}$ transition with a 986 nm Extended Cavity Diode Laser (ECDL) frequency doubled to produce 493 nm light. The $6P_{1/2}$ level decays to the metastable $5D_{3/2}$ level with a branching ratio of 0.25, so a 650 nm ECDL is used to pump the population out of this state. An applied 5 gauss magnetic field prevents the creation of dark states. All relevant transitions and energy levels of Ba^{+} are shown in Figure 3.1. Ytterbium is not directly laser-cooled, but sympathetically cooled by Coulomb interactions with the cold barium ions in the chain.

All temperature measurements are performed on barium ions using a 1762 nm fiber laser (Koheras Adjustik) stabilized to a Zerodur-spaced reference optical cavity with a free spectral range of 500 MHz and finesse of 1000. A complete description of the apparatus can be found in [32, 109].

While the short-term linewidth of the 1762 nm laser is of order 100 Hz [77], slow frequency drifts result in a 5 kHz linewidth. This is consistent with the locking system being incapable of stabilizing the laser frequency to better than a few kHz, while the laser itself has a narrow linewidth. Our frequency scans take tens of minutes to a few hours and are thus broadened, so features separated by <15 kHz are not well resolved.

The 1762 nm laser is aligned perpendicular to the trap z-axis, and at roughly 45 degrees to the x- and y-axes. Thus, only the radial sidebands are present in the frequency scans. The laser is focused to a 30 μm Gaussian spot size centered at the ion chain, driving all ions with comparable Rabi frequencies. Polarization control of the 493 nm cooling laser beam with a Pockel's cell is used to optically pump barium ions to the same $6S_{1/2}$ Zeeman state at the start of each run. After the 1762 nm laser exposure, we detect the state of each

a)

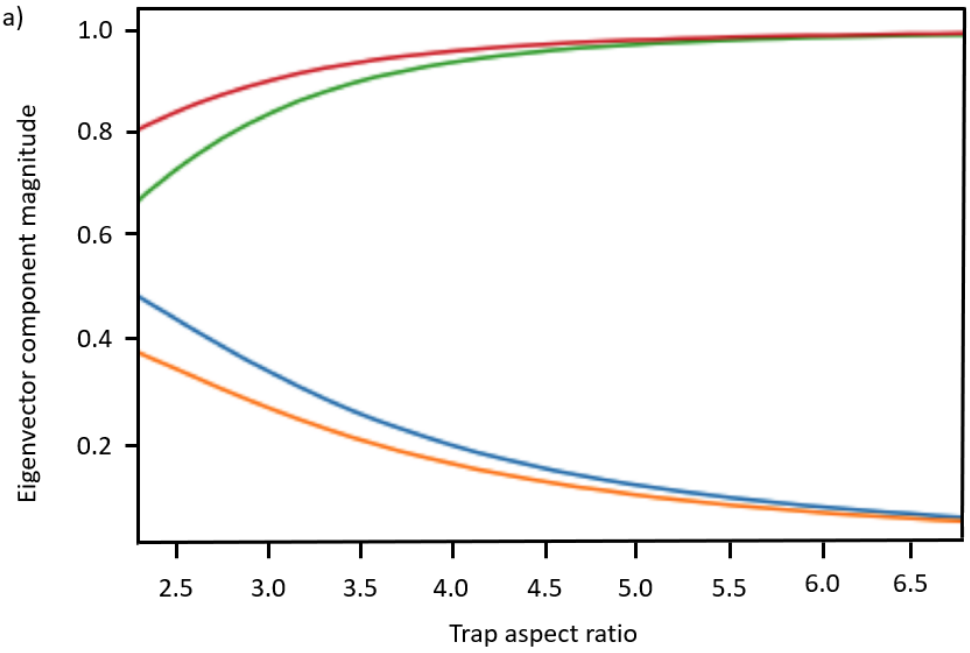

b)

	Aspect ratio of 5.5		Aspect ratio of 2.9	
	Ba	Yb	Ba	Yb
Mode 1	0.1006	0.9921	0.3572	0.9069
Mode 2	0.0933	0.0048	0.2903	0.2449
Mode 3	0.9712	0.0847	0.8163	0.1869
Mode 4	0.1947	0.0926	0.3491	0.2873

Figure 3.2: (a) Eigenvector components of the second Ba^+ ion in the BYBY chain in all four radial modes along the x principal axis of the trap. The left cutoff is the edge of the zig-zag transition. The two normal modes with larger eigenvectors (two upper lines) couple more strongly to the motion of the lighter Ba ions, while the two normal modes with smaller eigenvectors (two lower lines) couple weakly. As the trap aspect ratio decreases, eigenvector magnitudes with values lower than 0.5 increase and those with values higher than 0.5 decrease. (b) Eigenvector magnitudes of the first ytterbium and the second barium ions for all four radial modes in x-direction at the aspect ratios of 5.5 and 2.9. All four ions are in the same BYBY configuration.

barium ion simultaneously with an Electron-Multiplied Charge-Coupled Device (EMCCD) camera (Andor Luca) by imaging light scattered by the ions on the cooling transition. If the $6S_{1/2} - 5D_{5/2}$ transition took place, then the ion appears dark; otherwise the ion appears bright. At the end of each experimental run, a short pulse of 614 nm laser light from a frequency-doubled ECDL near 1228 nm returns the barium ions to the ground state. While changing trap aspect ratio we keep axial trapping potential constant and vary RF-potential.

We use LabVIEW in order to integrate all hardware devices presented in this work. RF TTL switches are used for the fast control of the SPAOMs located on the path of each laser beam. All TTL switches are connected to the digital ports of the NI-PXI machine. The outputs on these ports are controlled by users through the LabVIEW interface. RIGOL Arbitrary waveform generator's signal in the frequency range of $\approx$ 80-90 MHz is sent to the SPAOM on the beam path of 1762 nm laser. Frequency scan of 1762 nm to find the carrier and/or sidebands of $6S_{1/2} - 5D_{5/2}$ transitions can be performed by changing the output RIGOL frequency. After passing SPAOM, the 1st order 1762 nm laser beam is fiber-coupled and sent to the trap. The beam needs to be tightly focused; this can be achieved by using the beam expander and 15 cm plano-convex lens. With the following setup, I got about 1 mW of laser power with the beam size of $\approx 40\mu$m is at the trap center.

The experimental sequence is as follows. We Doppler cool the barium ions with the 493 nm and 650 nm lasers for approximately 50 ms with the Pockel's cell turned to 60 V. Then we discharge the Pockel's cell to circularly polarize the 493 nm laser. The switching time of the Pockel's cell is approximately 1 ms, so we wait for 5 ms to ensure full optical pumping. The 493 nm and 650 nm laser beams are then extinguished successively, and a 1762 nm pulse is applied. Afterward, the 493 nm, 650 nm, and Pockel's cell are turned on for 50 ms to read out the states of the barium ions. The readout fidelity is limited due to the optical crosstalk between neighboring ions; in this experiments with 50 ms readout time it is 97.8%. After the readout is performed, 614 nm laser pulse with the duration of 5 ms is applied to de-shelve the ion(s). The experiment is repeated, varying either the frequency of the 1762 nm during sideband scans, or the duration of the pulse during Rabi flop experiments. Detailed pulse sequence of Pockel cell, 650 and 493 nm lasers prior to applying 1762 nm laser pulse is shown in Figure 3.3.

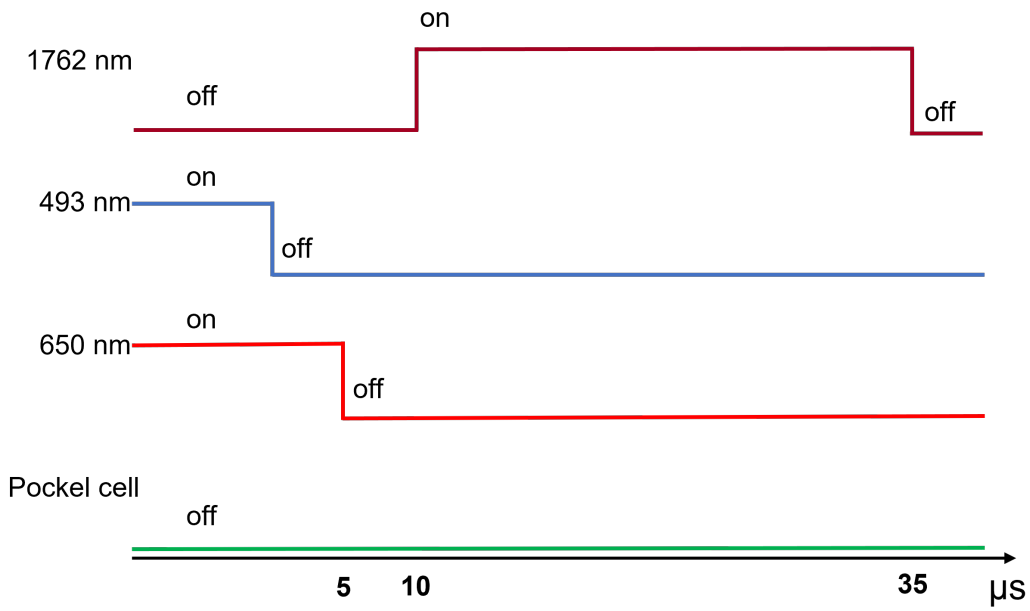

Figure 3.3: Experimental sequence controlled by RF TTL switches. Prior to this sequence Pockel cell is turned off for 5 ms while 650 and 493 nm lasers are on to ensure full optical pumping. To avoid broadening of the $S_{1/2} - 5D_{5/2}$ transition, 493 and 650 nm lasers are turned off before applying 1762 nm laser pulse. The red laser stays on 5 μs longer to avoid the ion being shelved in the $5D_{3/2}$ state. In this case 1762 nm laser pulse is 35 μs long that corresponds to Pi/2 pulse of one of the $6S_{1/2} - 5D_{5/2}$ transitions. This experimental sequence is then followed by the readout and de-shelving with applying 614 nm laser.

During the experiment the chain sometimes spontaneously reorders, due to either background gas collisions or high chain temperature. When we detect reordering, we discard the experimental cycle and re-establish the chain order by performing melting and crystallization cycles induced by shuttering and unshuttering the Doppler cooling lasers.

3.4 Results

We perform weak excitation sideband scans over all radial modes of all possible configurations of two barium and two ytterbium ions. The results are summarized in Figure 3.4. The normal mode decompositions are used to generate the data fits, as the peak frequencies are the frequencies of the radial eigenmodes, and the relative peak amplitudes on different ions are given by the eigenvector components and the average occupation numbers (see eqn. 3.4). The 1762 nm carrier Rabi frequency at each ion position is measured in a separate experiment by performing the carrier Rabi flops with a chain of four barium ions. The Doppler limit for the secular frequency modes between 0.5-0.9 MHz corresponds to an $\bar{n}$ of $16 - 30$ for a $^{138}Ba^{+}$. The peak sizes are proportional to the associated $\bar{n}$'s, the eigenvector component β_{ij}'s, and the exposure time, which is not displayed in the Figure, but is adjusted to stay in the weak excitation regime. In the bottom scan, a squeeze potential is applied to the trap's RF rods, which pushes the radial mode frequencies apart and changes the eigenvector component sizes along the two axes.

The data from our earlier experiments (which can be found in [109] and are not shown in Figure 3.4) indicated the $\bar{n}$ to be 50 to 2000 times higher than the Doppler limited $\bar{n}$ for some of the normal modes, which meant that chains under those conditions could not be used successfully for sympathetic cooling or inter-species quantum logic gates. Analysis of that data revealed a correlation [109] between the maximum eigenvector component of the cooled ion species and the measured $\bar{n}$. Noting the correlation, we searched for trap and chain configurations for which the eigenvector components would be large for the cooled species in all modes. Using the numerical normal mode structure calculation tool described in the theory section, we found that lowering the trap aspect ratio from 5.5 (used in [109]) to 2.9 increases the normal mode eigenvector component values above the expected 0.05 "threshold "value regardless of chain ordering. Some chain orderings were found to be

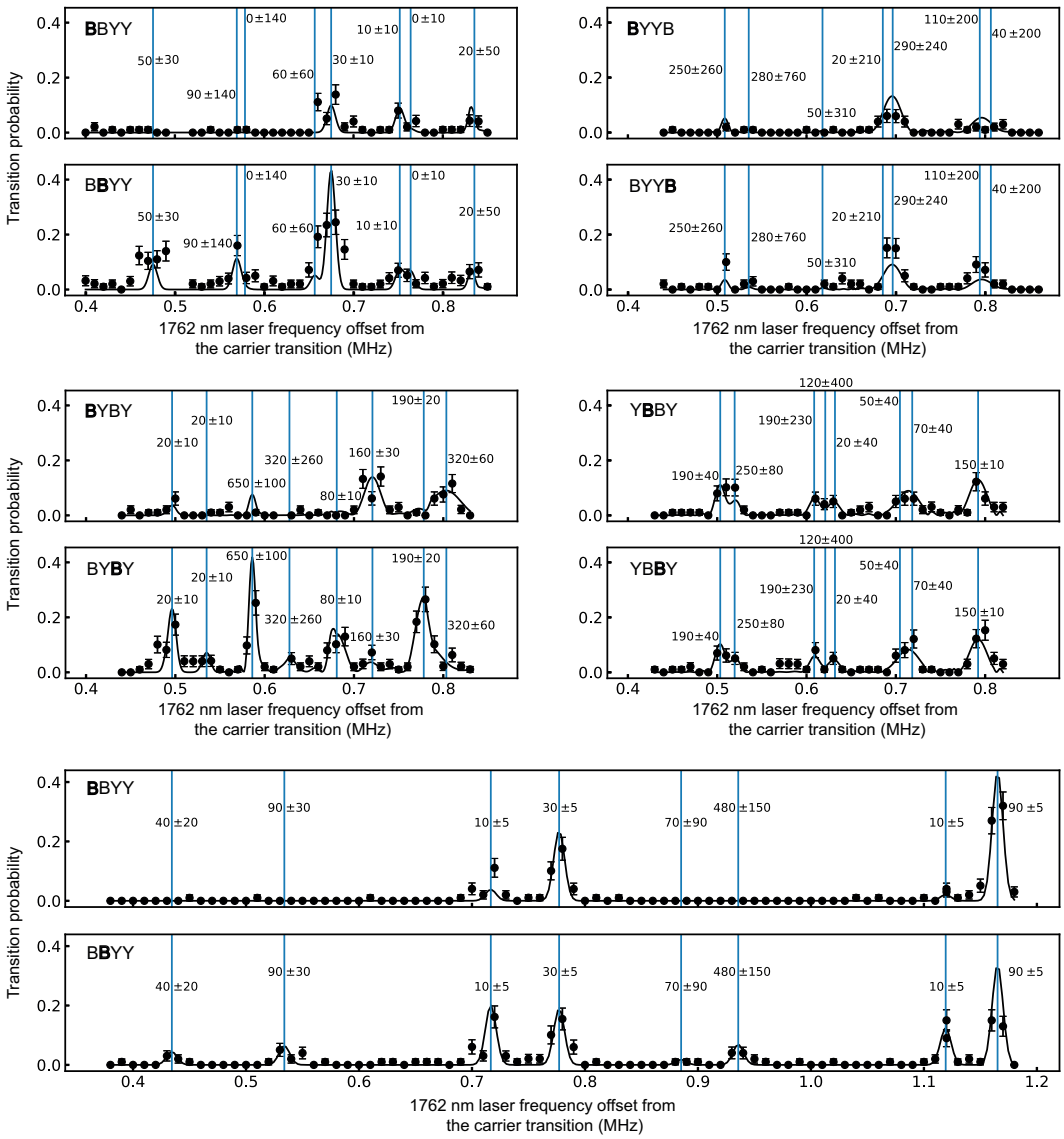

Figure 3.4: 1762 nm laser scans showing $\Delta n = 1$ sideband transitions. Two sets of radial mode peaks are present in each scan. Bold font is used to indicate which Ba^+ in the chain the spectrum was taken from. Radial mode occupation numbers are extracted from the peak amplitudes. The vertical lines indicate the calculated frequencies of the normal modes, and the associated radial mode occupation numbers are printed close by. The error bars on the measured occupation numbers are statistical.

better cooled than the others. For example, in the BYYB configuration, the maximum eigenvector component is at least 30% lower than the maximum eigenvector component in any other configuration.

We summarize our measurements of the radial mode $\bar{n}$ as a function of the maximum eigenvector component for both the old set [109] with trap aspect ratio of 5.5 and the new set of data with trap aspect ratio of 2.9 in Figure 3.5. We find very large reduction in $\bar{n}$ for maximum eigenvector component above approximately 0.05. These values of $\bar{n}$ correspond to normal mode temperatures between the Doppler limit for a single trapped barium ion and about 40 times that Doppler limit. These values are consistent with the technical difficulties of achieving the Doppler cooling limit in a lambda system such as Ba^+ [55]. At low intensities of the cooling and repump lasers, the rate of heating from residual micromotion balances the cooling rate well above the Doppler limit, while at high intensities the combination of power broadening and interference effects between the cooling and the repump transitions causes the minimum temperature to also increase well above the Doppler limit. In order to achieve Lamb-Dicke regime for many ions system additional EIT cooling is suggested. [68]

3.5 Conclusions

We studied the sympathetic cooling of barium-ytterbium chains in a linear RF trap in which only barium is directly laser cooled. We found that reducing the aspect ratio of the trap reduced the measured ion temperature in all normal modes. The ion chain has been cooled from a factor of 50 to 2000 the Doppler limit (well outside the Lamb-Dicke regime) to within a factor of 1 to 40 the Doppler limit, which is consistent with the cooling limitations in our setup. Our measurements show that the radial normal mode temperature is strongly dependent on the size of the maximum normal mode component of the cooled species. We conclude that in order to achieve efficient sympathetic cooling and interspecies quantum logic gates using radial vibrational modes, harmonic traps with lower aspect ratios are desirable.

The next step for accurate study of Ba-Yb sympathetic cooling will be the separation of the cooling and the 'probe' species. As it was discussed previously, Ba ions underwent

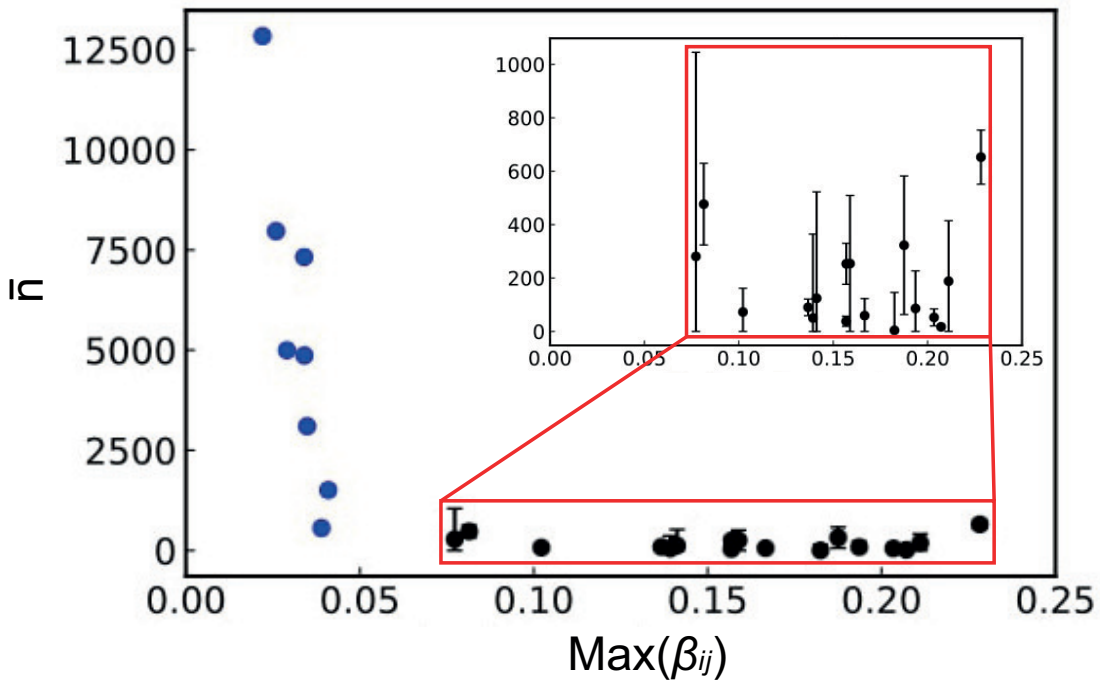

Figure 3.5: The $\bar{n}$ values vs maximum eigenvector component. The normal mode occupation number shows threshold-like behavior. All new data in the eigenvector component range $\beta_{ij} > 0.05$, shown in black, were taken at an aspect ratio of 2.9 except for the last set of data in Figure 3.4 corresponding to the Ba-Ba-Yb-Yb configuration. Data in the range $\beta_{ij} < 0.05$, shown in blue, are taken from [109] and are not presented in Figure 3.4. These data do not have uncertainty displayed because the measured temperatures are outside the Lamb-Dicke regime.

Doppler cooling and served as an indicator of the chain temperature. Optical pumping, shelving and state detection while performing Doppler cooling of Ba ions can lead to a chain heating so it should be minimized or avoided. In the future sets of experiments, these roles can be separated since we have necessary equipment for Yb Doppler cooling.

Chapter 4

DIRECT OBSERVATION OF TRAPPED ION MICROMOTION AND MULTI-QUBITS STATE DETECTION WITH A TIMEPIX3CAM SINGLE-PHOTON SENSITIVE CAMERA

In this chapter we demonstrate the use of Tpx3cam, a novel single-photon sensitive camera, in trapped ion experiments. We perform detection of multiple-qubit state as well as observation of micromotion in a linear ion chain.

4.0.1 Direct observation of trapped ion micromotion

The motion of trapped ions in radiofrequency (RF) traps can be described as a superposition of a slower harmonic motion, called the secular motion, and a faster, driven motion at the frequency of the applied electric field, called micromotion. Excess micromotion may lead to significant frequency modulation of the laser light interacting with the ions, reducing the efficiency of laser cooling [24] and quantum logic gates [41]. Second-order Doppler shifts caused by micromotion can adversely affect trapped ion clocks [57]. Thus, detection, monitoring, and compensation of excess micromotion is crucial for high-precision applications such as quantum computing and frequency standards. Micromotion detection and compensation is especially important in chip-scale surface-electrode ion traps because the ions are close to the trap surfaces and, thus, are more susceptible to the stray DC electric fields that shift the trapping position away from the RF null and cause excess micromotion.

Several techniques for micromotion detection have been developed, including the photon correlation technique and micromotion sideband spectroscopy [13, 102], high-finesse optical cavity [23], and parametric resonance detection [51]. All methods for micromotion detection listed above are indirect, require additional optical setup, and typically rely on ion fluorescence rate or spectrum changes caused by the ion motion. Another technique [57] provides stroboscopic micromotion measurements of multiple ions with an intensified CCD camera using a specially designed pulse generator for imagining synchronized with the trap

RF source. This method offers approximately 10 ns time resolution, limited by the trigger pulse duration, and thus, it may not provide enough positional data in the case of lower trap frequencies.

Here the direct observation of the trapped ion micromotion is presented using a time-resolving, single-photon sensitive camera that provides both fluorescence and position data for each ion on a nanosecond time scale. With this technique, both the micromotion amplitude and phase for each ion in the crystal can be measured individually. This can provide information about the tilts and shifts of the ion chain from the null of the radiofrequency quadrupole potential in a linear trap. The high spatial resolution makes this method suitable for micromotion studies in more complex ion configurations, including two-dimensional geometries [54]. Another advantage of this method is its simplicity: no additional equipment, such as time-to-digital converters (TDCs) or high-finesse cavities are required, and no modulation of the trap voltages or lasers is necessary.

4.0.2 Experimental Setup and Methods

In this section the experimental setup and methods are described in detail. This includes the linear RF trap and the Timepix3 fast camera used for measurement.

An 8-ion chain of Ba^+ ions is stored and Doppler-cooled in a "five-rod" linear RF trap [32], schematically shown in Figure 4.1a. The ions are laser cooled on the $6S_{1/2} - 6P_{1/2}$ transition near 493 nm, a process which produces the fluorescent photons used in the measurement of micromotion. The cooling laser is directed at 45 degrees to the axis of the trap. A 650 nm laser is used to repump ions from the long-lived $5D_{3/2}$ metastable state. The ion fluorescence is collected by a lens with numerical aperture of 0.20 along the direction perpendicular to both the trap axis and the cooling laser. The trap RF frequency is $\Omega = 2\pi \cdot 18.2516$ MHz at approximately 400 Vpp applied to the pair of the trap rods labelled "RF" in the Figure 1a. A "squeeze" voltage of 6 V is applied to the other pair of rods (labelled "DC" in Figure 1a) to lift the secular frequency degeneracy. The endcap electrodes are at 130 V, resulting in trap secular frequencies $(\omega_x, \omega_y, \omega_z) = 2\pi(1.27, 0.98, 0.25)$ MHz. Adjustable DC bias voltages may be applied to any of the trap rods to intentionally shift the

ions away from the RF null and induce micromotion, or to compensate excess micromotion as the ions are shifted toward the RF null.

The ions are imaged with a single-photon sensitive camera, Tpx3Cam [40, 117, 1], with high spatial and temporal resolution. Figure 4.1b shows the image of eight Ba^+ ions in the trap as a two-dimensional distribution of their positions measured by the camera. The camera technology allows direct position detection of single photons on a time scale that is much faster than the 54.79 ns period of the ion micromotion. Multiple photon source position measurements taken over the period of micromotion provide displacement data for individual ions to be analyzed and mapped. Fitting position data for each ion over time to a sinusoidal function gives a direct estimate of the ion micromotion amplitude and phase.

The Tpx3Cam camera has an optical sensor with high quantum efficiency (QE) [78] which is bump-bonded to Timepix3 [87], a readout chip with 256×256 pixels of 55×55 μm^2. The electronics in each pixel process incoming signals to measure their time of arrival (ToA) if a predefined threshold with 1.56 ns precision is crossed. The information about time-over-threshold (ToT) is stored together with ToA as time codes in a memory inside the pixel. The ToT information is related to the deposited energy in each pixel. The Timepix3 readout is data driven so the signal storage and readout proceed only after the pixel signal exceeds the threshold. The pixel dead time is 475 ns + ToT allowing for multi-hit functionality in each pixel, independent from the other pixels. The SPIDR readout system supports fast, 80 Mpix/sec bandwidth [104].

The camera was calibrated to equalize the response of all pixels by adjusting the individual pixel thresholds. After this procedure, the effective threshold to fast light flashes is $600 - 800$ photons per pixel, depending on the wavelength. A small ($\approx 0.1\%$) number of hot pixels were masked, i.e. pre-programmed in Timepix3 to stay inactive during the data collection. This prevents saturating the readout bandwidth with useless data since the pixel deadtime is only a few microseconds.

The camera can also accept and time stamp an external pulse, independently of the Timepix3 operation. In our experiments, these pulses were produced by a generator with frequency of about 100 kHz providing an additional time reference for registered photons. The granularity of the time-stamping for the external pulses is 0.26 ns.

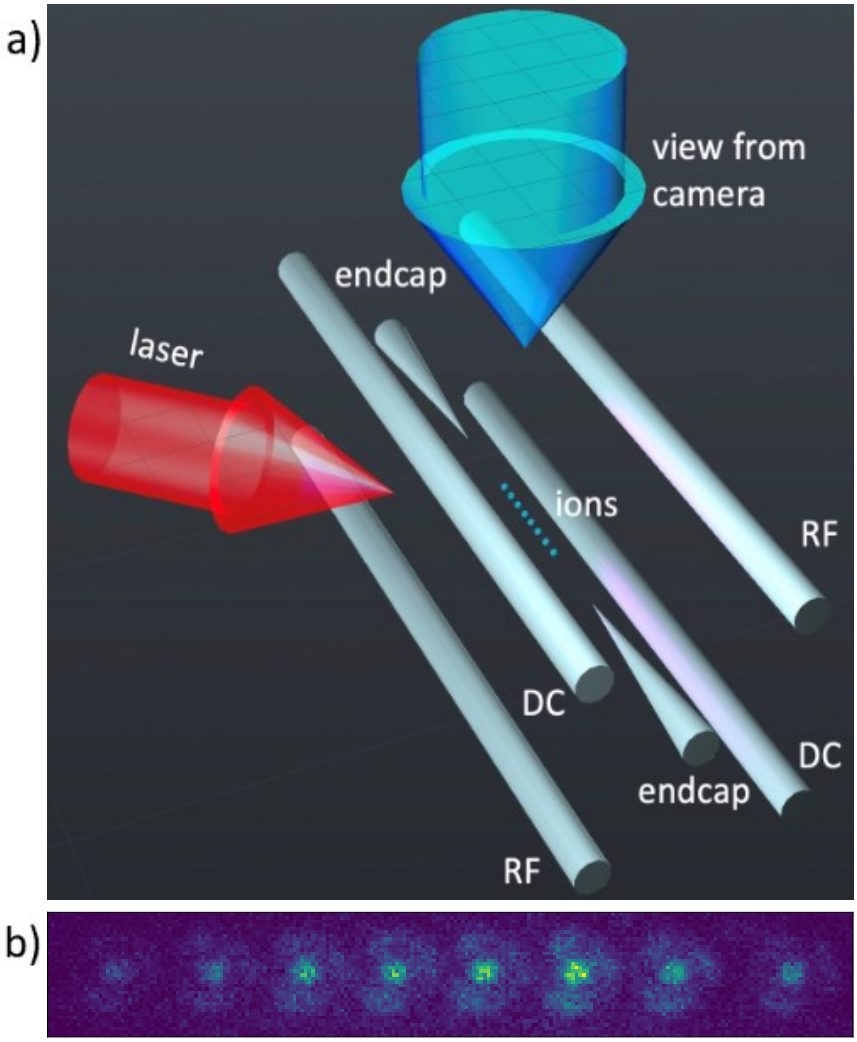

Figure 4.1: (a) Diagram of the experimental setup with ions in a linear RF trap formed by four rods and two needle endcap electrodes. DC bias voltages may be applied to any of the four rods to compensate the micromotion. The cooling laser (red arrow) is applied at 45 degrees to the trap axis and the ion string is imaged from above. (b) Image of eight Ba^+ ions taken with the Tpx3Cam camera over a 20 s integration period. The ion brightness variation is due to the Doppler cooling beam profile. The distance between the middle ions is approximately 5 μm.

For the single photon operation, the signal is amplified with the addition of an image intensifier. The image intensifier is a vacuum device comprised of a photocathode followed by a micro-channel plate (MCP) and fast scintillator P47. The hi-QE-green photocathode in the intensifier (Photonis [2]) has QE of about 20% at 493 nm and dark count rate of about 200 Hz over the full area (18 mm diameter). The MCP in the intensifier has an improved detection efficiency close to 100%. The intensifier is packaged with an integrated power supply and relay optics to project the light flashes from the intensifier output window directly on to the optical sensor in the camera. Similar configurations of the intensified Tpx3Cam were used previously for trapped ion imaging [120], characterization of quantum networks [50, 80], quantum target detection [116, 101], single photon counting [81] and lifetime imaging [97] studies.

4.0.3 Analysis

This section provides information on the offline post-processing of the data.

After sorting data by time, the pixels are grouped into "clusters" using a recursive algorithm. Clusters are small collections of pixels adjacent to each other that were triggered within a predefined time window of 300 ns. Each cluster corresponds to an individual photon. Since all hit pixels measure ToA and ToT independently and provide the position information, it can be used for centroiding to determine the coordinates of single photons. The ToT information is used to form a weighted average, giving an estimate of the x, y coordinates for the incoming single photon. The timing of the photon is estimated by using the recorded ToA of the pixel with the largest ToT in the cluster. The above ToA is then adjusted for the so-called time-walk, an effect caused by the variable pixel electronics time response, which depends on the amplitude of the input signal [103, 117]. With this correction a 2 ns time resolution (rms) has been previously achieved for single photons [50].

Data was collected for 300 seconds. The average photon detection rate per ion is approximately 1000/s; however, due to the nonuniform cooling laser beam profile, the emission rate varies between the ions.

The photon emission rate for ions in a trap oscillates with the RF period because of

the varying Doppler shift as the velocity of the ions change with respect to the laser beam due to micromotion. During data collection, external reference signals were provided to the camera by a pulse generator that was running synchronously with the trap RF, generating a pulse every 185th RF period, at a rate of approximately 100 kHz. This time reference was used to measure the oscillations by forming the time difference between the photon emission time and reference signal. Figure 4.2a shows the distribution of the time differences for the whole period of the reference pulses, 10,136 ns, and Figure 4.2b shows it for a subset of nine oscillations. The oscillations are well described by a periodic function with period of 54.79 ns, which is exactly the period of the trap RF.

There are 185 fluorescence rate oscillations during the 10,136 ns cycle of the reference pulse. To sum the statistics in all oscillations, the distribution from Figure 4.2a was folded into a single oscillation accounting for the measured period of 54.79 ns. This provides a composite distribution of the ion fluorescence rate during a single micromotion cycle, shown in Figure 4.2c. It represents the probability of the fluorescence during a single RF cycle, and can be correlated with the measured position of the ions to determine the ion micromotion since the ion position time dependence is already measured.

Time-stamping of photons and external pulses is performed independently from each other during data collection, and the analysis described above is done offline during post-processing. The same time information for the ions would be accessible from the individual pixel time-stamps so a similar analysis could have been done without any need of external pulses. However, it is an efficient technique to accumulate the time difference statistics without prior knowledge of the oscillation frequency. It allows to determine the oscillation period promptly, in real time, and can be used for fast online monitoring of the micromotion.

4.0.4 Results

The presented optical setup allows imaging of ion motion in the plane perpendicular to the camera direction of view, spanned by the axis of the trap and the radial direction perpendicular to the optical axis of the camera. No significant micromotion was observed along the trap axis (see figure 4.3), since in this trap the RF field is mostly radial near

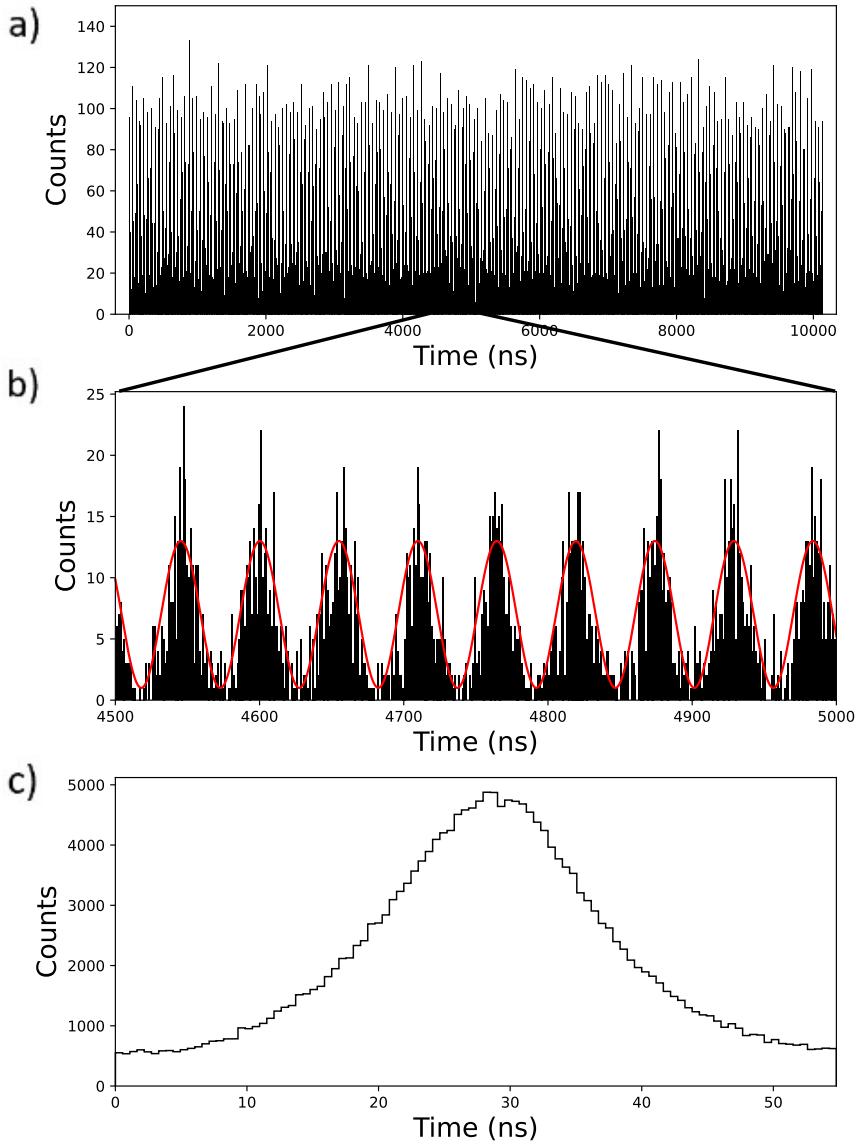

Figure 4.2: (a) Distribution of the time difference between the fluorescent photons and the periodic external signal for the whole period of 10,136 ns. (b) Zoomed-in section of the same distribution for a subset of nine oscillations. The oscillations are well described with a sine function with a period of 54.79 ns (red line), which is exactly the period of the trap RF. (c) Time distribution of the entire data set in (a) after applying the data folding procedure over the oscillation period as described in the text. The resulting distribution represents the probability of a photon emission during the micromotion period.

the trap center. All further presented results correspond to ion motion along the radial direction. The measurement of the ion positions was performed by time-slicing the full oscillation period into multiple bins ("snapshots") and determining the ion coordinates in each time bin. As an example, Figure 4.4a shows such snapshots of the sixth ion from Figure 4.1b during the full period of the micromotion oscillation. Here six images are separated by 9 ns, and the image statistics corresponds to a 3 ns time integration at the time stamp of the bin. Both the displacement of the ion and the modulation of its fluorescence due to the Doppler shift are clearly visible. In the Supplemental Material at the "snapshot" of 8 ions at 30 ns from of the 54.79 ns micromotion period as well as the animation of both the ions' displacements and fluorescence modulation due to the Doppler shift are provided. Figure 4.4b shows the measured y-position of the sixth ion as a function of the time in 3 ns bins. The data is well described by a sinusoidal function

$$y = A\sin[2\pi(t + t_0)/T] \tag{4.1}$$

with a period $T = 54.79$ ns, amplitude $A = 0.37 \pm 0.03$ μm and time offset $t_0 = 1.0 \pm 0.4$ ns. The time offset is proportional to the phase of the micromotion. The period was determined as described in Section 'Analysis' while the amplitude and phase are fits to the data.

The amplitudes and time offsets for all eight ions in the crystal are determined by performing the analysis individually for each ion. The results are shown in Figure 4.5. All ions have similar values for amplitude and time offset, which agree well within the measurement uncertainties, implying their near identical micromotion. This indicates that the ion chain was shifted from the RF null of the trap without a tilt, as expected in our setup. An animation of the micromotion dynamics of the entire 8-ion chain is provided in the Supplemental Material by using ion chain snapshots.

By applying compensation DC voltage to the trap rods (Figure 4.1a), the ion position along one of the radial axes can be shifted either toward or away from the trap RF null and, thus, can increase or decrease the micromotion amplitude in this direction. Figure 4.6 shows the micromotion of the sixth ion for two cases: without any DC compensation voltage (0V) and with 0.44V, which corresponds to 550 V/m, applied to one of the trap rods. In the latter case there is a considerable reduction of the micromotion amplitude from

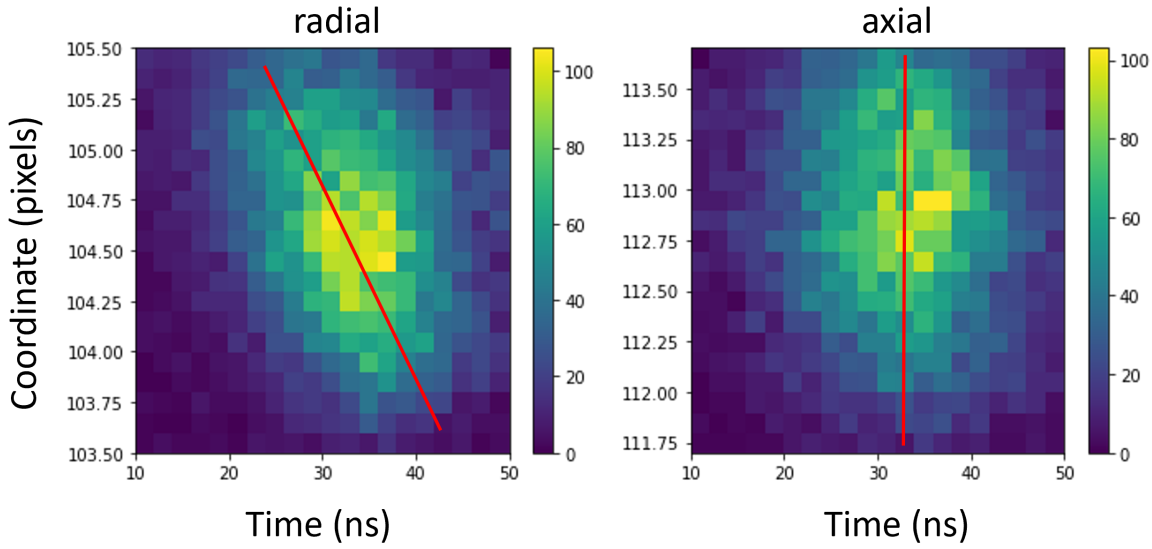

Figure 4.3: Correlations between ion's fluorescence, it's coordinate (pixels) and time (ns) within the RF period of 54.7 ns along the radial and the axial trap axes. Red line is used as a guide to demonstrate correlation between time and ion's position. There is correlation between ion's position along radial axis and time, and no such correlation for the axial position.

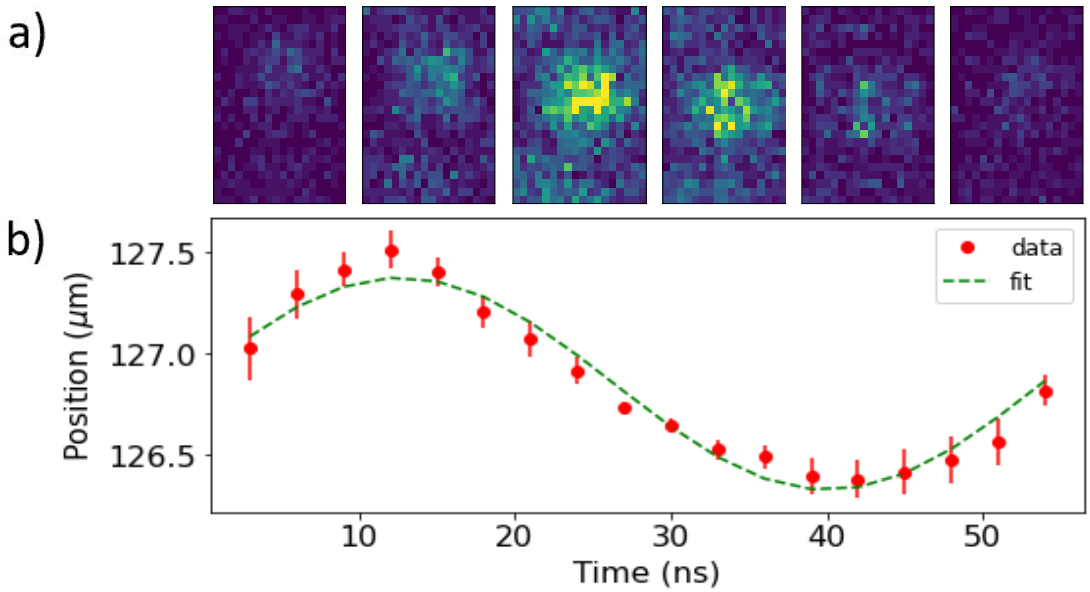

Figure 4.4: Direct observation of the ion micromotion. a) Snapshots of the sixth ion during micromotion oscillation in six time bins separated by 9 ns each. The shown statistics corresponds to 3 ns time integration around the midpoint of the bin. b) Position of the sixth ion over time. The data is shown in red dots; the error bars come from fitting the ion image to a Gaussian function. The dashed green line is a sinusoidal fit to the data with a period $T = 54.79$ ns, amplitude $A = 0.37 \pm 0.03$ μm and time offset $t_0 = 1.0 \pm 0.4$ ns.

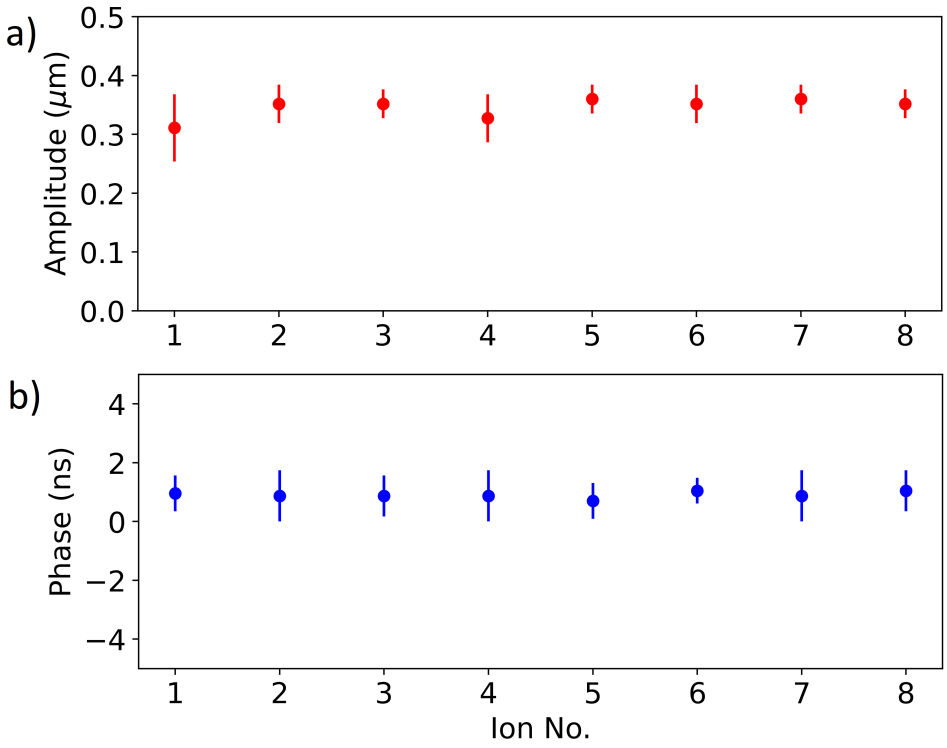

Figure 4.5: Amplitudes (a) and time offsets (b) of the individual ions. Error bars are determined from the fit parameters.

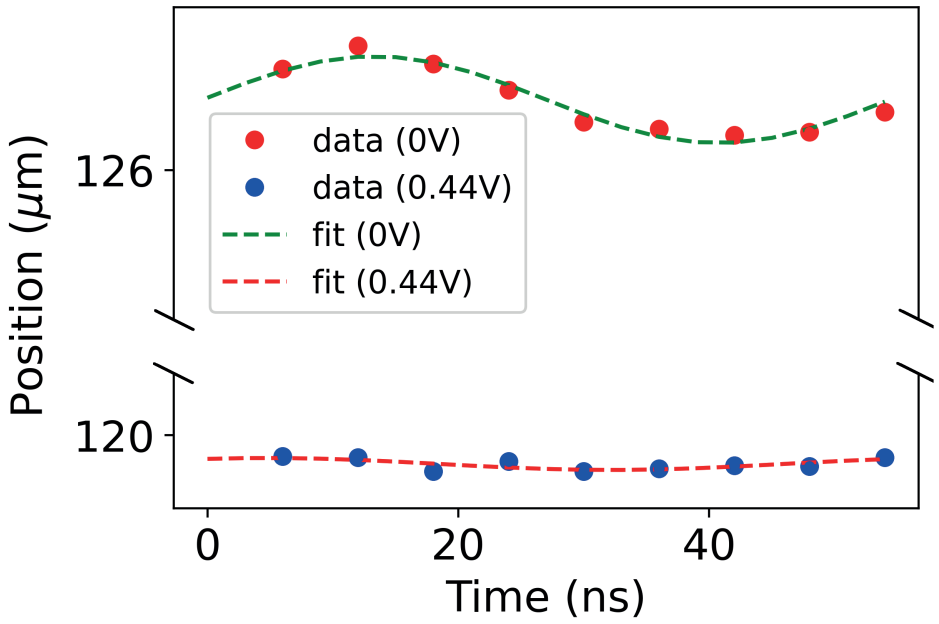

Figure 4.6: The micromotion of the sixth ion without the DC compensation voltage (red dots with green dashed line fit) and with 0.44V, which corresponds to DC electric field of 550 V/m, applied (blue dots with red dashed line fit). The error bars are smaller than the dot size.

0.37 ± 0.03 μm to 0.07 ± 0.03 μm. There is also a 7 μm displacement of the ion position caused by the applied voltage due to the changed electrostatic field configuration.

In addition to using the position information for micromotion measurement, time histograms like in Figure 4.2c provide velocity information for each ion through the Doppler-shifted scattering rate. As ions undergo micromotion, the component of their velocity along the direction of the incident laser beam causes the frequency of the laser to be Doppler shifted in the reference frame of the ions proportional to the instantaneous velocity. The red-detuned Doppler cooling laser becomes less (more) detuned from the atomic resonance as the ion moves toward (away from) the laser, resulting in the increase (decrease) of the photon scattering rate [13]. This modulation provides an independent way to estimate the component of micromotion along the direction of the laser beam, which can be used to

estimate ion micromotion. This well-known technique has previously been implemented in many experiments by time-correlating single photons detected by a photomultiplier tube (PMT) with the RF phase using a TDC [13, 89]. However, the PMT lacks spatial resolution so the old method only works for single ions. With the spatial resolution of the Tpx3Cam, precision determination of every ion's micromotion should be possible but here we limit our discussion to the novel direct micromotion detection technique.

Both techniques rely on the excellent time resolution of the camera, however the direct measurement technique also relies on the precise reconstruction of ion positions, so it requires good coordinate resolution of the camera and a diffraction limited optical system with high light collection efficiency and low aberrations.

To investigate the limits of the presented technique, we estimate the minimum ion displacement that is possible to measure with this method. This provides the minimum detectable micromotion amplitude, which, in turn, can be used to calculate the minimum detectable stray DC electric field for any trap geometry, since it depends only on the spatial resolution of the camera. In this work, the upper limit of the spatial resolution can be estimated using the value of the standard deviation of the measured micromotion amplitude, which is about 50 nm. We believe that this limit could be improved by increasing the photon collection time, as well as by improving the quality of the ion image with a higher N.A. imaging optics.

4.0.5 Conclusions

This paper demonstrates the direct simultaneous measurement of the micromotion of eight ions in a linear RF trap using a single photon sensitive camera with nanosecond timing resolution that provides both time and position measurements for each detected photon. Amplitudes and time offsets of each ion's micromotion were determined and found to be consistent with a translation of the linear ion crystal away from the RF nodal line. Excess micromotion compensation was demonstrated to below 0.1μm. The new technique does not require prior knowledge of the cooling laser parameters or addressing narrow atomic transitions. No special modifications of the trap, lasers or imaging apparatus is necessary,

since the same Tpx3Cam camera used in this work to observe the micromotion is also used as the regular imaging tool for setting up the trap, and can also be used as a fast and sensitive detector for high-fidelity trapped ion qubit state readout [120]. In conjunction with a high numerical aperture objective lens, this method may be used to detect the micromotion component along the direction parallel to the imaging axis by analyzing the ion image defocusing [42], thus providing a full 3-dimensional picture of the micromotion. This technique is also applicable to more complex ion configurations such as two-dimensional ion crystals.

4.1 Multi-qubits State with a TimePix3Cam Single Photon Sensitive Camera

Trapped ions are among the most promising candidates for practical quantum computing due to a combination of unique properties, including very long coherence times, high fidelity qubit state initialization, manipulation and detection, and prospects for scaling up [74, 14]. State-dependent fluorescence is used to detect trapped ion qubit state. It relies on the existence of a cycling transition, which includes one of the qubit states (called the "bright" state) and excludes the other (the "dark" state) [108]. A single ion scatters a large number of photons when in the bright state, which are collected and detected. An ion in the dark state does not scatter any photons. Simple discrimination between of the number of detected photons provides single-shot measurement of the qubit state. Scaling up the trapped ion system requires counting the number of photons individually for each ion. Thus, an optical system and a photon-counting detector with sufficient spatial resolution is necessary.

Fidelity of multi-qubit state detection in a trapped ion chain depends on the integration time, photon collection efficiency, performance of the optical system, instrumental noise, and detection crosstalk. Single ion qubit state detection fidelity of up to 0.99971(3) has been demonstrated in $^{133}Ba^{+}$ using a photomultiplier tube (PMT) [22]. Simultaneous detection of multiple ions requires spatially-resolving detectors. Electron-multiplying charge-coupled device (EMCCD) cameras are commonly used [8, 76]. A single $^{40}Ca^{+}$ qubit readout error as low as $0.9(3)\times10^{-4}$ using an EMCCD was demonstrated, limited by the 1.168(7) s spontaneous emission life time of the qubit [18]. Similar camera has been used to measure the state of a 53-ion qubit register [114] with nearly 0.99 single-qubit detection efficiency.

However, the serial interface of a CCD camera is slow. Segmented multi-anode PMTs offer fast, on-demand detection with some degree of spatial resolution. However, due to crosstalk between the PMT channels, multi-qubit state detection fidelity is lower than the product of the single-qubit fidelities. For example [71], a single-qubit detection fidelity of 0.994 was observed in a 5-qubit system using a segmented PMT, while the 5-qubit state detection fidelity was only 0.957, which is noticeably lower than 0.970 expected from the independent error model. To lower the crosstalk, superconducting nanowire single photon detectors (SNSPDs) have been used for state detection of two ions [26] with average qubit state detection time of 11 μs and average fidelity of 0.99931(6). However, scaling up the number of SNSPDs to tens and hundreds is challenging.

Here we demonstrate simultaneous detection of four $^{138}Ba^{+}$ ion qubits. The qubit is spanned by the $6S_{1/2}$ ground state and the $5D_{5/2}$ metastable state (spontaneous emission life time $\tau = 31.2(0.9)$ s [7]) of the ions. Ion detection was done with a time-stamping, single-photon-sensitive camera Tpx3Cam [40, 79, 119]. The camera has a high quantum efficiency (QE) back-side illuminated optical sensor [78], bump-bonded to the Timepix3 [87], an application-specific integrated circuit with 256×256 pixels measuring 55×55 μm^2 each. Electronics in each pixel processes the incoming signals to measure their time of arrival (ToA) for hits that cross a predefined threshold with 1.56 ns temporal granulation. Information about time-over-threshold (ToT), which is related to the deposited energy in each pixel, is stored together with ToA as time codes in a memory inside the pixel. The Timepix3 operation is data-driven, with pixel dead time of only 475 ns + ToT allowing for independent multi-hit functionality for each pixel with 80 Mpix/sec total bandwidth.

4.1.1 Apparatus

For the single photon operation, the signal is amplified using a Cricket^{TM} adapter with integrated image intensifier and relay optics to project light flashes from the intensifier output window directly on the optical sensor of the camera. The image intensifier is a vacuum device comprised of a photocathode followed by a micro-channel plate (MCP) and fast scintillator P47. The hi-QE-green photocathode in the intensifier has QE of about 20%

at 493 nm. The MCP in the intensifier had an improved detection efficiency close to 100%. Similar configurations of the intensified Tpx3Cam were used before for characterization of quantum networks [50, 80], quantum target detection [116, 101], single photon counting [81] and for lifetime imaging [97].

After ordering in time, pixels are grouped into "clusters" using a recursive algorithm [117]. Clusters are small collections of adjacent pixels within a predefined 300 ns time window. Since all hit pixels measure ToA and ToT independently and provide position information, they can be used for centroiding to determine the coordinates of single photons. ToT information is used for the weighted average, giving an estimate of the x and y coordinates for the incoming single photon. The timing of the photon is estimated by using ToA of the pixel with the largest ToT in the cluster. This ToA is then adjusted for the so-called time-walk, an effect caused by the variable pixel electronics time response, which depends on the amplitude of the input signal [103, 117].

The 4-ion chain of $^{138}Ba^{+}$ was stored in a "five-rod" linear RF trap [**?**]. To Doppler-cool ions, $6S_{1/2} - 6P_{1/2}$ transition near 493 nm was used. A 650 nm laser repumped ions from the long-lived $5D_{3/2}$ metastable state. A 1762 nm fiber laser was used to coherently drive the $6S_{1/2} - 5D_{5/2}$ quadrupole transition, which is the qubit transition in this experiment [110]. In this work, $5D_{5/2}$ and $6S_{1/2}$ are referred to as the dark and the bright states, respectively. The ion does not couple to the cooling/repump lasers when in the $5D_{5/2}$ state, so no fluorescence is detected; when in the $6S_{1/2}$ state, the ion scatters $\sim 10^7$ photons/s. Relevant energy levels and transitions in $^{138}Ba^{+}$ are shown in Figure 4.7(b).

The optical system is shown schematically in Figure 4.7(a). It consists of an objective lens (50 mm Nikon lens with numerical aperture 0.20), an adjustable aperture to filter out stray light, and a secondary lens (home-built 25 mm doublet). A 493 nm interference filter suppressed the background light. The magnification of the system is approximately 45, and its collection efficiency is approximately 1.3%.

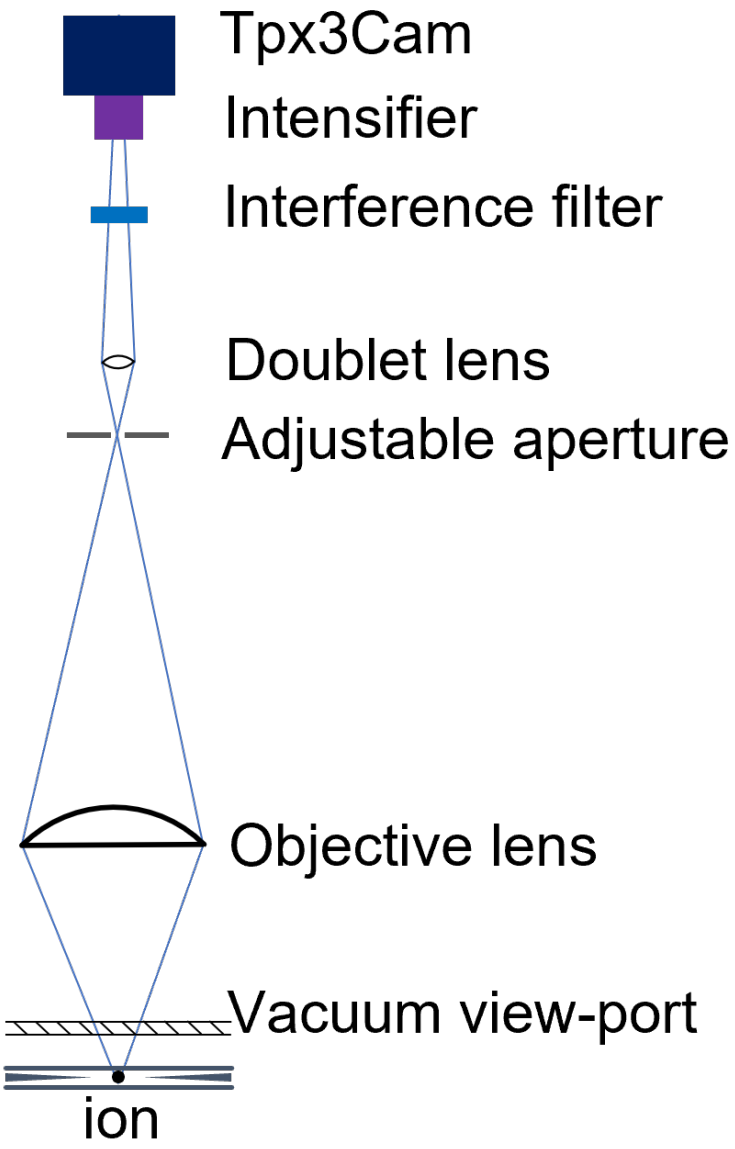

Figure 4.7: Optical setup: fluorescence from ions passing through the vacuum view-port is collected by the objective lens, through the adjustable aperture and further magnified by the doublet lens. An 493 nm interference filter is used to reduce the background. Finally, the 493 nm fluorescence is imaged onto the intensifier, which is connected to the Tpx3Cam camera.

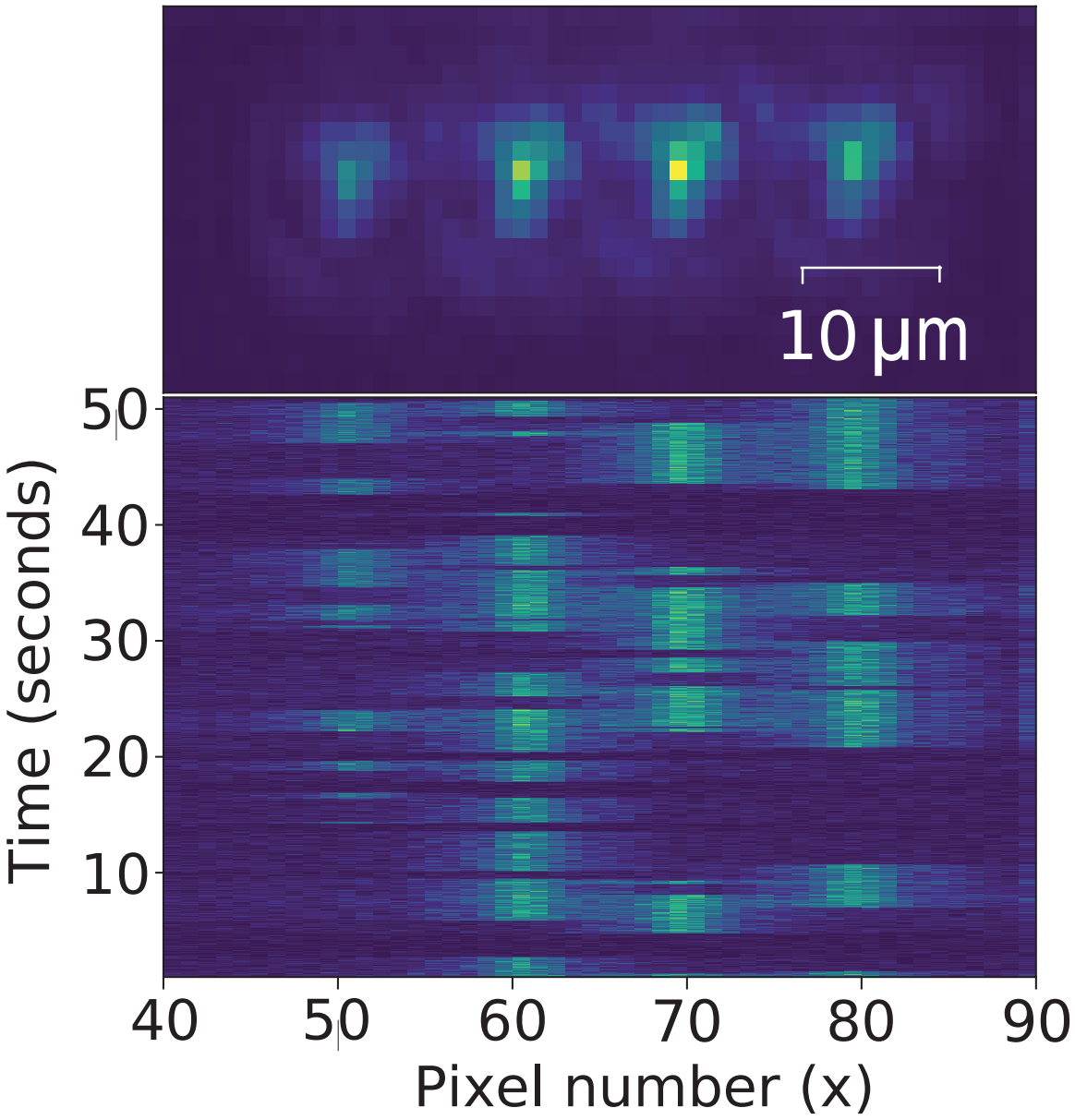

Figure 4.8: Image of 4 laser-cooled $^{138}Ba^{+}$ ions in a linear trap taken with an intensified Tpx3Cam camera, with a typical time sequence of all 4 ions undergoing quantum jumps shown directly below. The ion separation is approximately $10\mu m$.

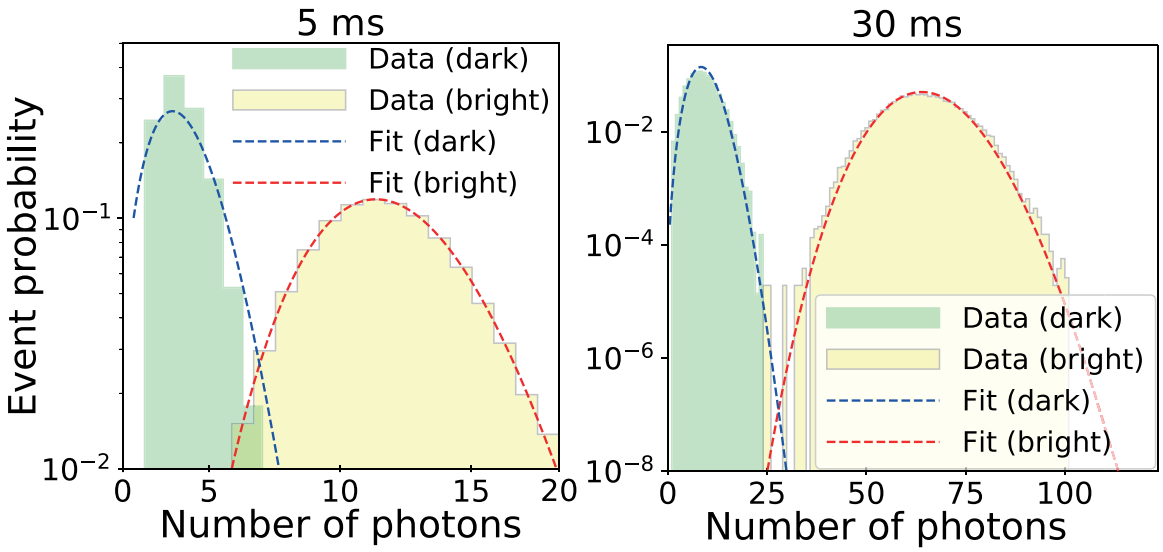

Figure 4.9: The bright and dark state histograms for the second ion from the left for two integration times. The probability to register a certain number of photons during the integration interval is plotted versus the number of photons, separately for dark and bright qubit states. The dashed curves are Poissonian fits to the data.

4.1.2 Analysis

We use threshold analysis method [18, 58] to calculate the qubit state detection error. We count the number of detected photons for each ion during a set time interval called the integration time, with n_b being the number of photons for the bright state and n_d for the dark state. n_d and n_b are random variables whose probability distribution functions (PDF) are well approximated Poisson distribution. The threshold method is based on setting a specific value n_{tr}, such that if the number of detected photons is greater than n_{tr}, then the ion state is bright, while if the number is lower than n_{tr}, then the ion state is dark. The optimal value of n_{tr} is near the intersection of dark state and bright state PDFs, where the value of the state detection error reaches its minimum. The detection error is defined as $(\epsilon_d + \epsilon_b)/2$, where ϵ_d is the probability to misidentify a dark state as bright and ϵ_b is the probability to misidentify the bright state as dark.

Data was collected with frequency and intensity of the 493 nm and 650 nm lasers set

to efficiently Doppler-cool the ions. The top panel in Figure 4.8(a) shows an image of four $^{138}Ba^{+}$ ions in the bright state. The 1762 nm laser was turned on at a low intensity, such that the ions underwent quantum jumps between the bright and dark states at a rate of approximately 1 per second or less. Note that due to slight misalignment of the 1762 nm laser beam the rate of quantum jumps was different for the four ions, as is evident from Figure 4.8(a), where the rate is greater for the leftmost ion. This difference, however, does not affect the results presented in this work.

Analysis was performed on several data sets of four ions undergoing the quantum jumps, amounting to 12 hours in total. We performed data post-selection to identify the state of each ion, making use of individual photon detection with reliable time of arrival. Time delays between the detected photons differ significantly between the dark and bright ion states. For this experimental setup, the average time between photons is approximately 0.5 ms for the bright state and 3.5 ms for dark state. Transitions between states can be identified by an increase or decrease of time delays between the detected photons. We set two temporal thresholds for identifying the transitions. If the time delay between two consecutive photons exceeds the upper threshold, the ion is in the dark state; if the time between consecutive photons is less than the lower threshold, the ion is in the bright state. Time delays that lie between the two thresholds do not provide enough certainty of the ion state and are excluded from analysis. A qubit transition has occurred in between the detection of two photons if the time delays of each photon lie on either side of the established thresholds. To confirm that a transition has indeed occurred, we check that the time delays for the next three photons after the detected transition correspond to the expected qubit state. If the time delay between any of the three consecutive photons appears to be between the two thresholds, the following dark or bright qubit state period is also excluded from the analysis. Time periods corresponding to the dark and the bright ion state were then evenly divided into time intervals equal to the desired integration time. Only periods that contain multiple integration time intervals were used in the analysis. During the time interval selection we specified that the neighbouring ions must be in the bright state to maximize the negative effect of the optical crosstalk and estimate the upper bound of the qubit state detection error.

After selecting the time intervals of the dark and bright states, we plotted the histograms for different integration times and obtained corresponding PDFs. In Figure 4.9, the bright/dark state histograms for the second ion from the left are plotted for 5 ms and 30 ms integration times. Only the photons detected within the 9×9 pixels square region of interest (ROI) were used. The size of the ROI was chosen to maximize the photon counts while minimizing the optical crosstalk. For each integration time, at least 5×10^4 time intervals were used for each ion.

There is a small but non-zero probability of spontaneous decay from the $5D_{5/2}$ dark state to the bright state during the integration time. This probability increases with increasing integration time, which could affect the overall detection fidelity if the photon number discrimination method is used. In presence of decay the dark state PDF becomes:

$$p_d = \frac{\tau - t_{int}}{\tau} P(n, \bar{n}_d) + \frac{t_{int}}{\tau} \frac{\Gamma(\bar{n}_b, n+1) - \Gamma(\bar{n}_d, n+1)}{\bar{n}_b - \bar{n}_d}, \tag{4.2}$$

where n is the number of photons, $P(n, \bar{n}_d)$ is the unperturbed Poisson distribution, $\bar{n}_b$ and $\bar{n}_b$ are the average numbers of detected photons, $\Gamma(\bar{n}_{d,b}, n+1)$ is the gamma distribution function, and t_{int} is the integration time. For the 30 ms integration time the decay probability is 0.00096, which would lead to an additional error of $\sim 4\times10^{-6}$ to incorrectly identify the dark state as bright. Since we selected pure bright/dark state intervals, the possibility of spontaneous emission occurring during the integration time is excluded in our estimation of the bright/dark state discrimination error. We separately calculate the qubit state detection error due to spontaneous emission and add it to the bright/dark state discrimination error.

There are multiple possible sources of the erroneous photon counts for an ion in the dark state, including the laser scattered from the trap surface, the intensifier dark counts, and optical/instrumental crosstalk. We found that the influence from the first two sources was negligible since the spatially uniform background/dark count rate was below 1 count/s within the ROI. Optical crosstalk was significant, with approximately 5.5% of the fluorescence of a bright ion falling into the ROI of the neighboring ion in the chain. Due to the astigmatism of the optical system, there is a slight variation of the crosstalk due to the

left neighboring ion compared to the right neighboring ion for each ion in the chain. This crosstalk leads to an increase in the average number of photon counts for the dark state histograms when the neighboring ions are in the bright state. Optical crosstalk leads to the broadening of the dark state histogram and increases the detection error. We estimate that in the case of the diffraction-limited optics, the corresponding light leakage would be 0.4%. Optical crosstalk can be significantly reduced by using optics with higher numerical aperture; for example, in [26] a diffraction-limited objective lens with numerical aperture of 0.6 was used. A higher numerical aperture optics both reduces the size of the Airy patterns leading to a lower optical crosstalk, and increases the total collection efficiency.

The instrumental crosstalk is caused by MCP afterpulsing in the intensifier of the camera. Electron avalanches in the MCP could result in the secondary electrons or ions producing independent hits in the vicinity of the primary hit [83, 82]. The time difference between the main hit and the afterpulse is small, so we can easily identify these cases as pairs of photons detected at the same time, looking at the time delay between photons detected from two neighboring bright ions. Figure 4.10 shows the time difference distributions between such photon detection events for two different time ranges.

The probability of detecting a fake hit due to the MCP afterpulses of 0.15% was determined from the data by estimating the number of events in the peak at $\Delta T = 0$ and normalizing it to the total number of registered photons. Since all the detected photons have time-stamps, this source of crosstalk can be removed by ignoring hits at the dark ion location in a 50 ns window around the time when another photon was registered at the neighboring bright ion location. In our case, the contribution of this crosstalk source is very small, at the level of only about 0.7 photons/s on average, and we did not apply this post-selection in our analysis.

4.1.3 Results

The summary of the single qubit state detection error for the second ion from the left is plotted as a function of the integration time in Figure 4.11. The data follow the expected trend for discriminating two random variables with Poisson distributions. The dark/bright

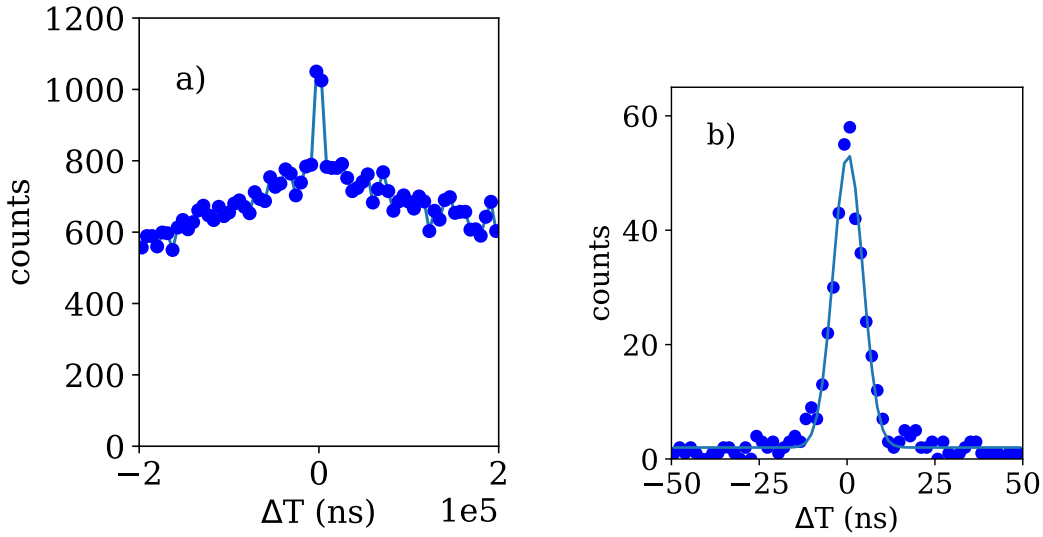

Figure 4.10: Time difference distribution for two time ranges, ±0.2 ms (a) and ±50 ns (b). The peak at $\Delta T = 0$, which corresponds to the MCP afterpulses, is fit to a Gaussian with a width $\sigma = 4.2$ ns.

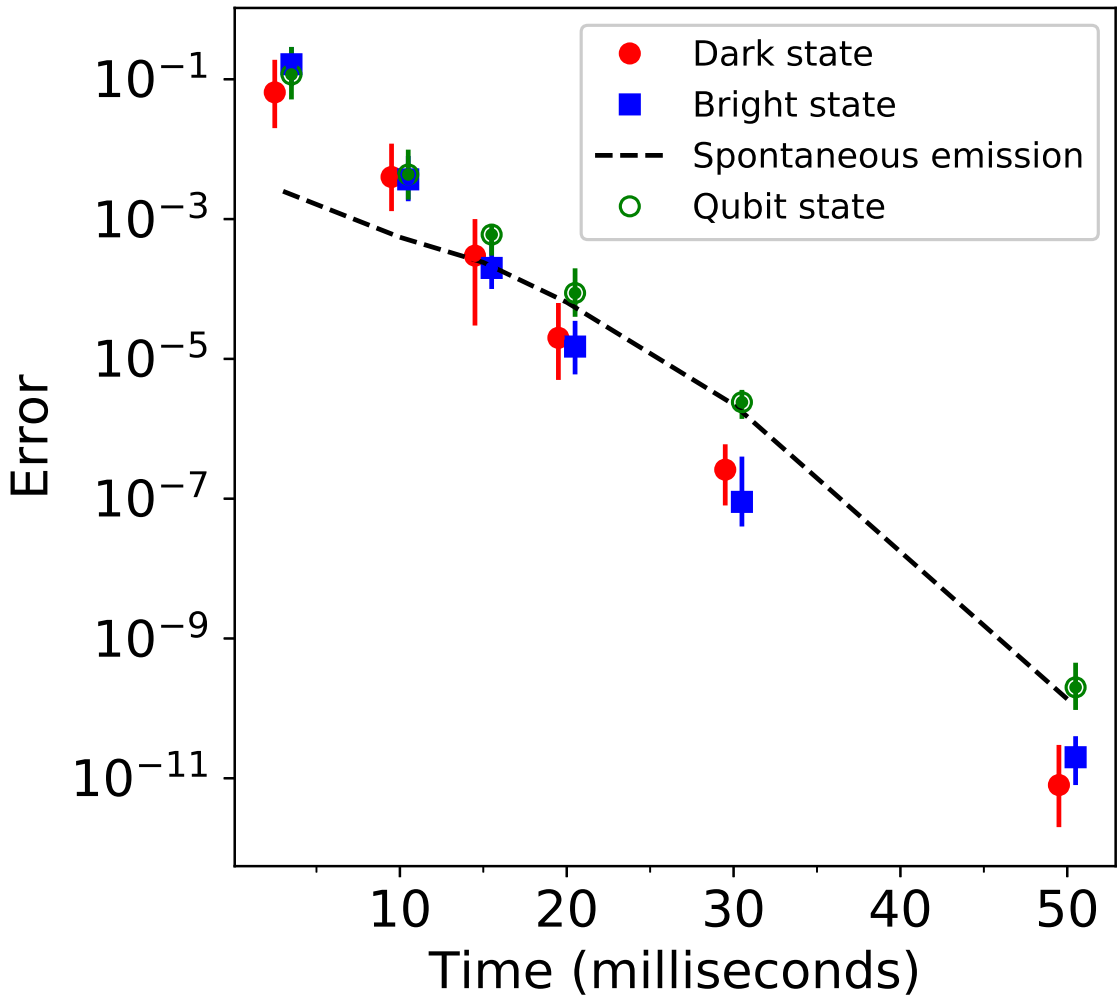

Figure 4.11: Detection errors as a function of integration time. Solid squares (circles) represent the data for the bright (dark) state discrimination errors. The optimal threshold value n_{tr} is set by calculating where two Poisson curves corresponding to dark/bright ion states cross by extrapolating the curves, and rounding this value to an integer. The error bars are calculated by setting the threshold to $n_{tr}\pm1$. Horizontal offset of $\pm$ 0.5 ms between dark and bright detection errors was introduced for clarity. The dashed line is the error due to the $5D_{5/2}$ spontaneous decay, calculated using Eq. 1. The combined error, shown in open circles, is the qubit state detection error that takes into account the bright/dark state discrimination error and the error due to spontaneous emission.

state errors are somewhat different due to the choice of n_{tr}. The average of the two errors is used to calculate the qubit state detection error for each ion. The fidelity of detection of the N-qubit state is calculated as a product of the single qubit fidelities $\Pi(1-\epsilon_i)$, where ϵ_i is the detection error of the i-th ion.

The average bright/dark state discrimination error at 30 ms integration time varies between $7(6)\times10^{-9}$ for the outer two ions, where the optical crosstalk is lower, and $5.8(3.8)\times10^{-7}$ for the inner ions. The additional error due to the qubit spontaneous emission is $5.4(0.4)\times10^{-6}$ for the outer qubits and $3(1)\times10^{-6}$ for the inner ones, the difference being due to the different values of n_{tr}. The single qubit state detection error averaged over all four qubits is 4.2(1.5) ppm, and the total detection error for the 4-qubit state is 17(2) ppm.

4.1.4 Conclusions

In summary, we demonstrated simultaneous detection of four $^{138}Ba^{+}$ ion qubits in a linear chain achieving a qubit state detection error of 4.2(1.5) ppm for a single ion in the presence of bright neighbouring ions with a 30 ms detection time, considerably improving previous results. The detection error of the four-qubit state was 17(2) ppm. The qubit state detection fidelity is limited by the lifetime of the $5D_{5/2}$ qubit state, which for barium ion is approximately 32 s, by far the longest of all ion qubit candidates, making it suitable for the highest qubit state detection fidelity. Further reduction of the detection error can be achieved by improving the collection efficiency of the optical system and reducing the crosstalk between neighboring ions. We conclude that the fast time-stamping camera used in the experiments offers a straightforward route for scaling up the number of simultaneously detected qubits in a linear ion chain. It can be increased to about 30 qubits in the present linear configuration with 10-pixel spacing between the ions, and to 60 qubits with reduced optical magnification giving a 5-pixel ion spacing. In the two-dimensional trap setup [54], the number of simultaneously detected qubits can easily be a few hundred. Even with a few kHz photon detection rate per ion, the total photon rate will still be below the maximum allowed rate of about 10^7 photons/s. The camera data can be promptly analysed in real time providing input for the error correction algorithms.

Chapter 5

ONGOING RESEARCH PROJECTS

5.1 Interaction Effect On Quantum Jump Rate In Linear Ion Chain

The collective effect of superradiance was first studied by Dicke in 1954 [31] and implies the coherence of absorption and emission of electromagnetic radiation for a group of atoms. The necessary condition for the superradiance phenomenon is a small inter-atomic distance; the inter-atomic distance has to be comparable to the wavelength of light. Superradiance has been observed for atomic clouds, for example, here [88] as well as for two 2 Ba^+ ions [30].

A few experimental groups studied the collective behavior in trapped atomic ions. Some of these groups reported no observation of collective effect on lifetime or quantum jump rate of ions [34, 52, 53]. On the other hand, some groups have reported observations of enhanced quantum jumps rate [95, 16]. The Dicke super- and sub-radiance was observed in a case of 2 Ba^+ ions, where the inter-atomic distance was to be comparable to the wavelength of light [30]. In some reported results, however, the inter-atomic distance was much larger than the wavelength of light, which cannot be explained by the theory of superradiance.

In this work, we study the collective effect on quantum jump rate in a linear ion chain paying attention to such experimental details as the quantum jump rate of individual ions, the number of ions, and the ion-ion separation relative to the relevant atomic transition wavelength.

We use single-photon sensitive camera TimePix3Cam, which was described in details in Sections 4.1 and 4.0.1. We believe that based on the difference of neighboring photons' arrival time (Dt), we can distinguish dark/bright state of an ion and find the exact moment when the ion undergoes a quantum jump. A similar technique has already been applied here [120]. An illustration of state determination of individual ion is shown in figure 5.1. Quantum jump rate can be determined as the number of dark-bright and bright dark transitions divided by the total time of the experiment. I believe that this is the only apparatus

that provides the necessary time resolution and has a spatial resolution to determine the moment of the quantum jumps for each ion in the chain.

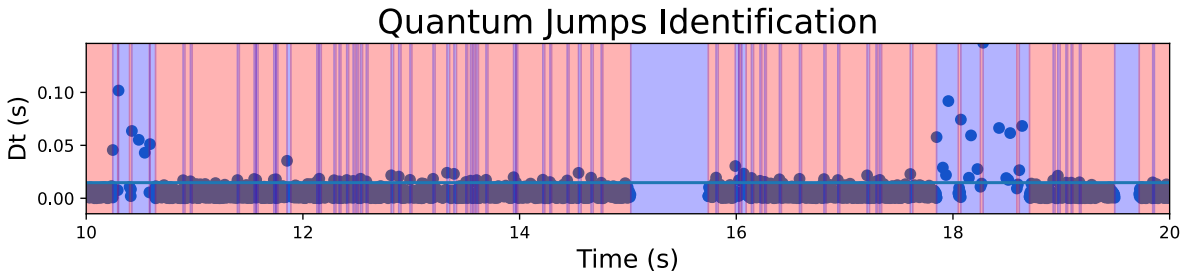

Figure 5.1: Representation of identified locations of quantum jumps. Blue shaded regions represent the dark state which does not fluoresce 493 nm photons. Red Shaded regions represent the brights state which fluoresces 493 nm light relatively quickly. Dt represents time interval between arriving photons.Credits: Sarah Edwards and Maverick Millican.

An important part of the analysis is setting a time threshold to distinguish between dark and bright ion states. By analyzing the distribution of Dt values individually for the ions in a data set, a threshold can be established that acts as a guide for identifying the state of the ion. It is shown (see figure 5.2) that the time difference distribution fits closely to an exponential distribution function, as expected. It was chosen to define the Dt threshold for state identification at the 2σ point of the exponential fit. This statistical value was determined because of the trend seen that the collected data begins to differ from the exponential fit consistently at this 2σ point. The deviation from the exponential fit is explained by the ion's dark state. In this state, no 493 nm photons are emitted, and therefore larger Dt values are observed when the ion is excited to this state.

I have taken data of multiple ions undergoing quantum jumps. The number of ions varies from two to ten, and the distance between them was in the range of $\approx$3 to 10 μm whether the wavelength of chosen transition is 1.72 μm. A few datasets were taken with various average quantum jump rates. After careful analysis, we found out that slower initial

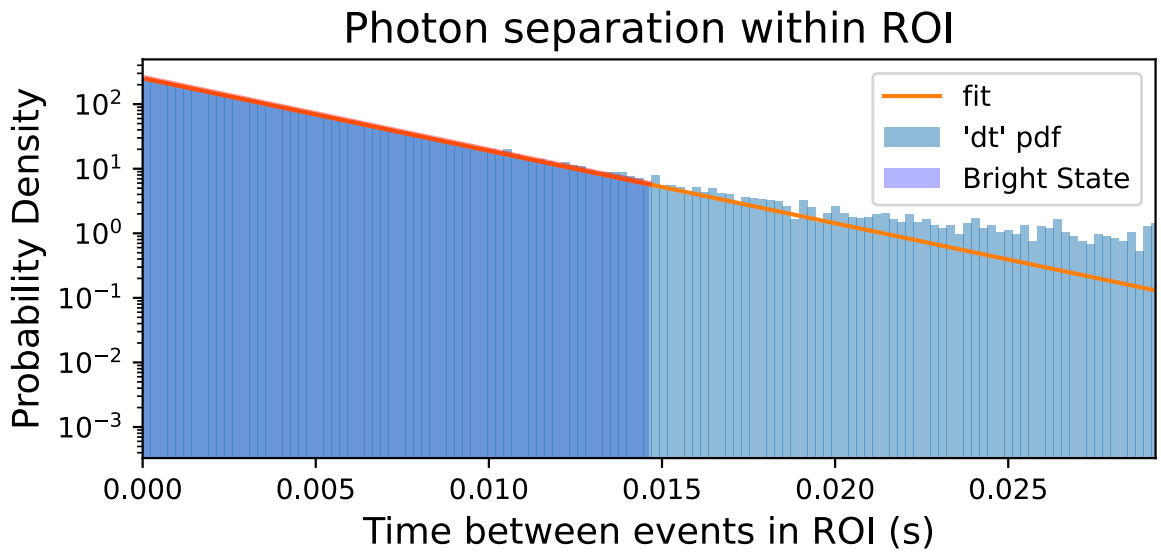

Figure 5.2: Histogram of time separation between photon hits from a single ion in the chain on a logarithmic plot. The dark shaded region represents the 2σ integration point which generally describes the point of divergence from the exponential fit and has been chosen as the threshold between the ground and excited states. The orange line describes the exponential fit to the data. Credits: Maverick Millican.

quantum jumps (≈1/sec) are preferable due to the ease of state determination and various available methods to do it (see details in 4.1). Currently, we are at the stage of careful data analysis, where for each data set with the various number of ions and the ion-ion distance, the data taking time was more than 60 minutes. This allows us to have ≈ 3600 trials to obtain the necessary statistical significance. I believe the results of this work will help to shed the light on the collective effect happening (or not happening) in the linear ion chain.

5.2 Qutrit

Toward the end of my Ph.D., I started working on the realization of the qutrit in $^{138}Ba^{+}$. We choose two states of $6S_{1/2}$ and any of the states from the $5D_{5/2}$ manifold to span the

qutrit. Qutrit operational basis will consist of σ_x, σ_y and σ_z operators between S and D states. The setup will be similar to one described in chapter 3 except a radio-frequency pulse, or multiple pulses will be added to the pulse sequence.

The first step toward qutrit demonstration would be an evaluation of the individual performance of the operations between two of the S-states ($S-S$ transitions) and between S and D states ($S-D$ transitions). $S-S$ transitions occur between two of the Zeeman levels whose degeneracy is lifted by an external magnetic field. Previously, it was demonstrated [109] that the coherence of these transitions does not decay with time as intensely as it does in the case of the optical $S-D$ transition. The coherence of the Zeeman transition is determined by the stability of the external magnetic field that splits the S-levels.

My recent goal was to check and, if necessary, improve the coherence time of the $S-D$ optical transitions. A simple test for this is varying the duration of the 1762 nm laser pulse and observing the shelving probability. Ideally, this should be a sinusoidal curve, but we will observe the decay of contrast due to either non-zero ion temperature or frequency instability of the 1762 nm laser.

The contrast of the Rabi oscillation of the $6S_{1/2}-5D_{5/2}$ is related to the coherence of these transitions. This limits the depth of the circuit that can be implemented using qutrit. Currently, the coherence can be improved by building a stronger trap, sending more RF power to the current trap, or performing sub-Doppler cooling.

Chapter 6

SUMMARY AND OUTLOOK

In this thesis, I have demonstrated multiple finished research projects, including studying the mechanics of sympathetic cooling and its efficiency in a linear harmonic trap, utilizing TimePix3Cam single-photon sensitive camera for high fidelity detection of qubit register and micromotion detection. Obtained information about trap parameters for efficient sympathetic cooling can be utilized for designing harmonic traps in such places as Honeywell and IonQ. There, the same Ba-Yb ion species are used. TimePix3Cam single-photon sensitive camera appeared to be novel for ion trappers. Due to its low instrumental noise, we demonstrated the highest readout fidelity of the trapped ion qubit register. For all future projects utilizing $^{138}Ba^{+}$ as qubit species and its $6S_{1/2}{-}5D_{5/2}$ transition to span a qubit, it is beneficial to use this camera. Due to the excellent spatial and time resolution of TimePix3Cam, we directly observed the micromotion of 8 ions in a linear trap. This method can be easily scaled to the larger number of ions and applied to non-linear trap geometries.

BIBLIOGRAPHY

[1] www.amscins.com, 2020.

[2] www.photonis.com/products/crickettm, 2020.

[3] https://dlmf.nist.gov/28, 2021.

[4] https://www.toptica.com, 2021.

[5] N. Akerman, Y. Glickman, S. Kotler, A. Keselman, and R. Ozeri. Quantum control of $^{88}Sr^{+}$ in a miniature linear paul trap. *Applied Physics B.*, 107:1167–1174, 2012.

[6] Carolyn Auchter, Chen-Kuan Chou, Thomas W. Noel, and Boris B. Blinov. Photon entanglement and bell inequality violation with $^{138}Ba^{+}$. *J. Opt. Soc. Am. B*, 31(7):1568–1572, Jul 2014.

[7] Carolyn Auchter, Thomas W. Noel, Matthew R. Hoffman, Spencer R. Williams, and Boris B. Blinov. Measurement of the branching fractions and lifetime of the $5D_{5/2}$ level of Ba^{+}. *Phys. Rev. A*, 90:060501(R), Dec 2014.

[8] A. Avella, I. Ruo-Berchera, I. P. Degiovanni, G. Brida, and M. Genovese. Absolute calibration of an EMCCD camera by quantum correlation, linking photon counting to the analog regime. *Optics Letters*, 41(8):1841, Apr 2016.

[9] M. D. Barrett, B. DeMarco, T. Schaetz, V. Meyer, D. Leibfried, J. Britton, J. Chiaverini, W. M. Itano, B. Jelenković, J. D. Jost, C. Langer, T. Rosenband, and D. J. Wineland. Sympathetic cooling of $^{9}Be^{+}$ and $^{24}Mg^{+}$ for quantum logic. *Phys. Rev. A*, 68:042302, Oct 2003.

[10] C. Barthel, D. J. Reilly, C. M. Marcus, M. P. Hanson, and A. C. Gossard. Rapid single-shot measurement of a singlet-triplet qubit. *Phys. Rev. Lett.*, 103:160503, Oct 2009.

[11] Jan Benhelm. PhD thesis, University of Innsbruck, 2008.

[12] C D B Bentley, A R R Carvalho, and J J Hope. Trapped ion scaling with pulsed fast gates. *New Journal of Physics*, 17(10):103025, 2015.

[13] D. J. Berkeland, J. D. Miller, J. C. Bergquist, W. M. Itano, and D. J. Wineland. Minimization of ion micromotion in a paul trap. *Journal of applied physics.*, 83:5025–5033, 1998.

[14] R. Blatt and D. Wineland. Entangled states of trapped atomic ions. *Nature*, 453:1008–1015, 2008.

[15] B. B. Blinov, L. Deslauriers, P. Lee, M. J. Madsen, R. Miller, and C. Monroe. Sympathetic cooling of trapped Cd^+ isotopes. *PRA*, 65(4):040304, April 2002.

[16] Block, M., Rehm, O., Seibert, P., and Werth, G. $3d\ ^2D_{5/2}$ lifetime in laser cooled Ca^+: Influence of cooling laser power. *Eur. Phys. J. D*, 7(3):461–465, 1999.

[17] Ivan A. Boldin, Alexander Kraft, and Christof Wunderlich. Measuring anomalous heating in a planar ion trap with variable ion-surface separation. *Phys. Rev. Lett.*, 120:023201, Jan 2018.

[18] A. H. Burrell, D. J. Szwer, S. C. Webster, and D. M. Lucas. Scalable simultaneous multiqubit readout with 99.99 single-shot fidelity. *Phys. Rev. A*, 81:040302(R), Apr 2010.

[19] Y. Castin, H. Wallis, and J. Dalibard. Limit of doppler cooling. *J. Opt. Soc. Am. B*, 6(11):2046–2057, Nov 1989.

[20] J.-S. Chen, S. M. Brewer, C. W. Chou, D. J. Wineland, D. R. Leibrandt, and D. B. Hume. Sympathetic ground state cooling and time-dilation shifts in an $^{27}Al^+$ optical clock. *Phys. Rev. Lett.*, 118:053002, Jan 2017.

[21] Chen-Kuan Chou. PhD thesis, University of Washington, 2017.

[22] Justin E. Christensen, David Hucul, Wesley C. Campbell, and Eric R. Hudson. High-fidelity manipulation of a qubit enabled by a manufactured nucleus. *npj Quantum Information*, May 2020.

[23] Boon Leng Chuah, Nicholas C. Lewty, Radu Cazan, and Murray Douglas Barrett. Detection of ion micromotion in a linear paul trap with a high finesse cavity. *Optics express*, 21 9:10632–41, 2013.

[24] J. I. Cirac, R. Blatt, P. Zoller, and W. D. Phillips. Laser cooling of trapped ions in a standing wave. *Phys. Rev. A*, 46:2668–2681, Sep 1992.

[25] J. I. Cirac and P. Zoller. Quantum computations with cold trapped ions. *Phys. Rev. Lett.*, 74:4091–4094, May 1995.

[26] S. Crain, C. Cahall, G. Vrijsen, E. Wollman, M. Shaw, V. Verma, S. W. Nam, and J. Kim. High-speed low-crosstalk detection of a $^{171}Yb^{+}$ qubit using superconducting nanowire single photon detectors. *Communications Physics*, 2, 2019.

[27] C. Crocker, M. Lichtman, K. Sosnova, A. Carter, S. Scarano, and C. Monroe. High purity single photons entangled with an atomic qubit. *Opt. Express*, 27(20):28143–28149, Sep 2019.

[28] Dipankar Das, Sachin Barthwal, Ayan Banerjee, and Vasant Natarajan. Absolute frequency measurements in yb with 0.08 ppb uncertainty: Isotope shifts and hyperfine structure in the $399-\text{nm}\ ^1s_0 \rightarrow ^1 p_1$ line. *Phys. Rev. A*, 72:032506, Sep 2005.

[29] K. Deng, Y. L. Sun, Z. T. Xu, J. Zhang, Z. H. Lu, and J. Luo. Design and construction of helical resonators for ion traps. In *2013 Joint European Frequency and Time Forum International Frequency Control Symposium (EFTF/IFC)*, pages 898–900, 2013.

[30] R. G. DeVoe and R. G. Brewer. Observation of superradiant and subradiant spontaneous emission of two trapped ions. In *Quantum Electronics and Laser Science Conference*, page QWH2. Optical Society of America, 1996.

[31] R. H. Dicke. Coherence in spontaneous radiation processes. *Phys. Rev.*, 93:99–110, Jan 1954.

[32] M. R. Dietrich, N. Kurz, T. Noel, G. Shu, and B. B. Blinov. Hyperfine and optical barium ion qubits. *Phys. Rev. A*, 81:052328, May 2010.

[33] Matthew Dietrich. PhD thesis, University of Washington, 2009.

[34] C. J. S Donald, D. M Lucas, P. A Barton, M. J McDonnell, J. P Stacey, D. A Stevens, D. N Stacey, and A. M Steane. Search for correlation effects in linear chains of trapped Ca^{+}ions. *Europhysics Letters (EPL)*, 51(4):388–394, aug 2000.

[35] Jürgen Eschner, Giovanna Morigi, Ferdinand Schmidt-Kaler, and Rainer Blatt. Laser cooling of trapped ions. *J. Opt. Soc. Am. B*, 20(5):1003–1015, May 2003.

[36] D. Hucul, et al. Modular entanglement of atomic qubits using photons and phonons. *Nature*, 2015.

[37] J. Pino, et al. Demonstration of the trapped-ion quantum ccd computer architecture. *Nature*, Feb 2021.

[38] T. P. Sakrejda, et al. Efficient sympathetic cooling in mixed barium and ytterbium ion chains. *Quantum Information Processing*, May 2021.

[39] Y. Wang, et al. Single-qubit quantum memory exceeding ten-minute coherence time. *Nature*, 2017.

[40] M. Fisher-Levine and A. Nomerotski. Timepixcam: a fast optical imager with time-stamping. *Journal of Instrumentation*, 11(03):C03016 (2016).

[41] J. P. Gaebler, T. R. Tan, Y. Lin, Y. Wan, R. Bowler, A. C. Keith, S. Glancy, K. Coakley, E. Knill, D. Leibfried, and D. J. Wineland. High-fidelity universal gate set for $^{9}Be^{+}$ ion qubits. *Phys. Rev. Lett.*, 117:060505, Aug 2016.

[42] Timm F. Gloger, Peter Kaufmann, Delia Kaufmann, M. Tanveer Baig, Thomas Collath, Michael Johanning, and Christof Wunderlich. Ion-trajectory analysis for micromotion minimization and the measurement of small forces. *Phys. Rev. A*, 92:043421, Oct 2015.

[43] Yasushichi Gosho, Manabu Yamada, and Masamori Saeki. Static charge elimination of charged matter using UV lamp. *Japanese Journal of Applied Physics*, 29(Part 1, No. 5):950–951, may 1990.

[44] M. Gross and S. Haroche. Superradiance: An essay on the theory of collective spontaneous emission. *Physics Reports*, 93(5):301–396, 1982.

[45] C. J. Hawthorn, K. P. Weber, and Robert E. Scholten. Littrow configuration tunable external cavity diode laser with fixed direction output beam. *Review of Scientific Instruments*, 72:4477–4479, 2001.

[46] D. Hayes, D. N. Matsukevich, P. Maunz, D. Hucul, Q. Quraishi, S. Olmschenk, W. Campbell, J. Mizrahi, C. Senko, and C. Monroe. Entanglement of atomic qubits using an optical frequency comb. *Phys. Rev. Lett.*, 104:140501, Apr 2010.

[47] J. P. Home, M. J. McDonnell, D. J. Szwer, B. C. Keitch, D. M. Lucas, D. N. Stacey, and A. M. Steane. Memory coherence of a sympathetically cooled trapped-ion qubit. *Phys. Rev. A*, 79(5):050305, May 2009.

[48] D. Hucul, I. V. Inlek, G. Vittorini, C. Crocker, S. Debnath, S. M. Clark, and C. Monroe. Modular entanglement of atomic qubits using photons and phonons. *Nature Physics*, 11:37, Nov 2014.

[49] H. Häffner, C.F. Roos, and R. Blatt. Quantum computing with trapped ions. *Physics Reports*, 469(4):155 – 203, 2008.

[50] Christopher Ianzano, Peter Svihra, Mael Flament, Andrew Hardy, Guodong Cui, Andrei Nomerotski, and Eden Figueroa. Fast camera spatial characterization of photonic polarization entanglement. *Scientific Reports*, 10(1), Apr 2020.

[51] Y. Ibaraki, Utako Tanaka, and Shinji Urabe. Detection of parametric resonance of trapped ions for micromotion compensation. *Applied Physics B*, 105:219–223, 2011.

[52] Wayne M Itano, J C Bergquist, Randall G Hulet, and D J Wineland. Precise optical spectroscopy with ion traps. *Physica Scripta*, T22:79–84, jan 1988.

[53] Wayne M. Itano, J. C. Bergquist, and D. J. Wineland. Photon antibunching and sub-poissonian statistics from quantum jumps in one and two atoms. *Phys. Rev. A*, 38:559–562, Jul 1988.

[54] Megan K. Ivory, Alexander Kato, A. Hasanzadeh, and Boris B. Blinov. A paul trap with sectored ring electrodes for experiments with two-dimensional ion crystals. *The Review of scientific instruments*, 91 5:053201, 2020.

[55] G. Janik, W. Nagourney, and H. Dehmelt. Doppler-free optical spectroscopy on the Ba^+ mono-ion oscillator. *J. Opt. Soc. Am. B*, 2(8):1251–1257, Aug 1985.

[56] Hans T. Karlsson and Ulf Litzén. Revised BaI and BaII wavelengths and energy levels derived by fourier transform spectroscopy. *Physica Scripta*, 60:321–328, 1999.

[57] J. Keller, Heather L. Partner, Tobias Burgermeister, and Tanja E. Mehlstaubler. Precise determination of micromotion for trapped-ion optical clocks. *Journal of Applied Physics*, 118:104501, 2015.

[58] Anna Keselman, Yinnon Glickman, Nitzan Akerman, Shlomi Kotler, and R. Ozeri. High-fidelity state detection and tomography of a single-ion Zeeman qubit. *New Journal of Physics*, 13:073027, 2011.

[59] D. Kielpinski, B. E. King, C. J. Myatt, C. A. Sackett, Q. A. Turchette, W. M. Itano, C. Monroe, D. J. Wineland, and W. H. Zurek. Sympathetic cooling of trapped ions for quantum logic. *Phys. Rev. A*, 61:032310, Feb 2000.

[60] D. Kielpinski, C. Monroe, and D. J. Wineland. Architecture for a large-scale ion-trap quantum computer. *Nature*, 417:709, June 2002.

[61] D. Kienzler, Y. Wan, S. D. Erickson, J. J. Wu, A. C. Wilson, D. J. Wineland, and D. Leibfried. Quantum logic spectroscopy with ions in thermal motion. *Phys. Rev. X*, 10:021012, Apr 2020.

[62] G Kirchmair, J Benhelm, F Zähringer, R Gerritsma, C F Roos, and R Blatt. Deterministic entanglement of ions in thermal states of motion. *New Journal of Physics*, 11(2):023002, 2009.

[63] E. Knill. Quantum computing with realistically noisy devices. *Nature*, 434, 2005.

[64] D. J. Larson, J. C. Bergquist, J. J. Bollinger, Wayne M. Itano, and D. J. Wineland. Sympathetic cooling of trapped ions: A laser-cooled two-species nonneutral ion plasma. *Phys. Rev. Lett.*, 57:70–73, Jul 1986.

[65] Bjoern Lekitsch, Sebastian Weidt, Austin G. Fowler, Klaus Mølmer, Simon J. Devitt, Christof Wunderlich, and Winfried K. Hensinger. Blueprint for a microwave trapped ion quantum computer. *Science Advances*, 3, 2017.

[66] Jennifer F. Lilieholm. PhD thesis, University of Washington, 2020.

[67] G.-D. Lin, S.-L. Zhu, R. Islam, K. Kim, M.-S. Chang, S. Korenblit, C. Monroe, and L.-M. Duan. Large-scale quantum computation in an anharmonic linear ion trap. *EPL (Europhysics Letters)*, 86(6):60004, 2009.

[68] Y. Lin, J. P. Gaebler, T. R. Tan, R. Bowler, J. D. Jost, D. Leibfried, and D. J. Wineland. Sympathetic electromagnetically-induced-transparency laser cooling of motional modes in an ion chain. *Phys. Rev. Lett.*, 110:153002, Apr 2013.

[69] Lin, G.-D., Zhu, S.-L., Islam, R., Kim, K., Chang, M.-S., Korenblit, S., Monroe, C., and Duan, L.-M. Large-scale quantum computation in an anharmonic linear ion trap. *EPL*, 86(6):60004, 2009.

[70] N. M. Linke, S. Johri, C. Figgatt, K. A. Landsman, A. Y. Matsuura, and C. Monroe. Measuring the rényi entropy of a two-site Fermi-Hubbard model on a trapped ion quantum computer. *Phys. Rev. A*, 98:052334, Nov 2018.

[71] Norbert M. Linke, Mauricio Gutierrez, Kevin A. Landsman, Caroline Figgatt, Shantanu Debnath, Kenneth R. Brown, and Christopher Monroe. Fault-tolerant quantum error detection. *Science Advances*, 3(10), 2017.

[72] Emil Wolf Max Born. *Principles of Optics 6th Edition.* Electromagnetic Theory of Propagation, Interference and Diffraction of Light. Pergamon, 1993.

[73] D. L. Moehring, P. Maunz, S. Olmschenk, K. C. Younge, D. N. Matsukevich, L.-M. Duan, and C. Monroe. Entanglement of single-atom quantum bits at a distance. *Nature*, 449, 2007.

[74] C. Monroe and J. Kim. Scaling the ion trap quantum processor. *Science*, 339(6124):1164–1169, 2013.

[75] C. Monroe, R. Raussendorf, A. Ruthven, K. R. Brown, P. Maunz, L.-M. Duan, and J. Kim. Large-scale modular quantum-computer architecture with atomic memory and photonic interconnects. *Phys. Rev. A*, 89:022317, Feb 2014.

[76] Paul-Antoine Moreau, Ermes Toninelli, Thomas Gregory, and Miles J. Padgett. Imaging with quantum states of light. *Nature Reviews Physics*, 1(6):367–380, May 2019.

[77] T. Noel, M. R. Dietrich, N. Kurz, G. Shu, J. Wright, and B. B. Blinov. Adiabatic passage in the presence of noise. *Phys. Rev. A*, 85:023401, Feb 2012.

[78] A. Nomerotski, I. Chakaberia, M. Fisher-Levine, Z. Janoska, P. Takacs, and T. Tsang. Characterization of timepixcam, a fast imager for the time-stamping of optical photons. *Journal of instrumentation*, 12(01):C01017, 2017.

[79] Andrei Nomerotski. Imaging and time stamping of photons with nanosecond resolution in timepix based optical cameras. *Nuclear Instruments and Methods in Physics Research Section A: Accelerators, Spectrometers, Detectors and Associated Equipment*, 937:26–30, September 2019.

[80] Andrei Nomerotski, Dimitrios Katramatos, Paul Stankus, Peter Svihra, Guodong Cui, Sonali Gera, Mael Flament, and Eden Figueroa. Spatial and temporal characterization of polarization entanglement. *International Journal of Quantum Information*, 18(01):1941027, Feb 2020.

[81] Andrei Nomerotski, Michael Keach, Paul Stankus, Peter Svihra, and Stephen Vintskevich. Counting of hong-ou-mandel bunched optical photons using a fast pixel camera. *Sensors*, 20(12):3475, June 2020.

[82] D. A. Orlov, R. Glazenborg, R. Ortega, and E. Kernen. UV/visible high-sensitivity MCP-PMT single-photon GHz counting detector for long-range lidar instrumentations. *CEAS Space Journal*, 11(4):405–411, Dec 2019.

[83] D.A. Orlov, T. Ruardij, S. Duarte Pinto, R. Glazenborg, and E. Kernen. High collection efficiency MCPs for photon counting detectors. *Journal of Instrumentation*, 13(01):C01047–C01047, jan 2018.

[84] Wolfgang Paul. Electromagnetic traps for charged and neutral particles. *Rev. Mod. Phys.*, 62:531–540, Jul 1990.

[85] E. Peik, J. Abel, Th. Becker, J. von Zanthier, and H. Walther. Sideband cooling of ions in radio-frequency traps. *Phys. Rev. A*, 60:439–449, Jul 1999.

[86] H Eberly Peter W Milonni. *Lasers*. Electromagnetic Theory of Propagation, Interference and Diffraction of Light. New York : Wiley, 1988.

[87] T. Poikela et al. Timepix3: a 65k channel hybrid pixel readout chip with simultaneous ToA/ToT and sparse readout. *Journal of instrumentation*, 9(05):C05013, 2014.

[88] J.V. Pulé, A.F. Verbeure, and V.A. Zagrebnov. *Bose-Einstein Condensation and Superradiance*, pages 259–278. Springer Berlin Heidelberg, Berlin, Heidelberg, 2006.

[89] Karsten Pyka, Norbert Herschbach, Jonas Keller, and Tanja E. Mehlstäubler. A high-precision segmented paul trap with minimized micromotion for an optical multiple-ion clock. *Applied Physics B*, 114:231–241, 2014.

[90] Vaishnavi Rajagopal, Joan P. Marler, Mark G. Kokish, and Brian C. Odom. Trapped Ion Chain Thermometry and Mass Spectrometry through Imaging. *European Journal of Mass Spectrometry*, 22(1), 2016.

[91] H Rohde, S T Gulde, C F Roos, P A Barton, D Leibfried, J Eschner, F Schmidt-Kaler, and R Blatt. Sympathetic ground-state cooling and coherent manipulation with two-ion crystals. *Journal of Optics B: Quantum and Semiclassical Optics*, 3(1):S34, 2001.

[92] A. Safavi-Naini, P. Rabl, P. F. Weck, and H. R. Sadeghpour. Microscopic model of electric-field-noise heating in ion traps. *Phys. Rev. A*, 84:023412, Aug 2011.

[93] Tomasz Sakrejda. PhD thesis, University of Innsbruck, 2017.

[94] Sebastian D. Saliba, Mark Junker, Lincoln D. Turner, and Robert E. Scholten. Mode stability of external cavity diode lasers. *Appl. Opt.*, 48(35):6692–6700, Dec 2009.

[95] Th. Sauter, R. Blatt, W. Neuhauser, and P.E. Toschek. 'quantum jumps' observed in the fluorescence of a single ion. *Optics Communications*, 60(5):287–292, 1986.

[96] Ferdinand Schmidt-Kaler, Hartmut Häffner, Mark Riebe, Stephan Gulde, Gavin P. T. Lancaster, Thomas Deuschle, Christoph Becher, Christian F. Roos, Jürgen Eschner, and Rainer Blatt. Realization of the Cirac–Zoller controlled-NOT quantum gate. *Nature*, 422:408, March 2003.

[97] Rajannya Sen, Liisa M. Hirvonen, Alexander Zhdanov, Peter Svihra, Stefan Andersson-Engels, Andrei Nomerotski, and Dmitri Papkovsky. New luminescence lifetime macro-imager based on a Tpx3Cam optical camera. *Biomed. Opt. Express*, 11(1):77–88, Jan 2020.

[98] G Shu, M R Dietrich, N Kurz, and B B Blinov. Trapped ion imaging with a high numerical aperture spherical mirror. *Journal of Physics B: Atomic, Molecular and Optical Physics*, 42(15):154005, jul 2009.

[99] A. V. Steele, L. R. Churchill, P. F. Griffin, and M. S. Chapman. Photoionization and photoelectric loading of barium ion traps. *Phys. Rev. A*, 75:053404, May 2007.

[100] Kazuhiko Sugiyama. Laser cooling of single $^{174}Yb^{+}$ ions stored in a rf trap. *Japanese Journal of Applied Physics*, 38(4R):2141, 1999.

[101] Peter Svihra, Yingwen Zhang, Paul Hockett, Steven Ferrante, Benjamin Sussman, Duncan England, and Andrei Nomerotski. Multivariate discrimination in quantum target detection. *Applied Physics Letters*, 117(4):044001, July 2020.

[102] T. R. Tan, R. Kaewuam, K. J. Arnold, S. R. Chanu, Zhiqiang Zhang, M. S. Safronova, and M. D. Barrett. Suppressing inhomogeneous broadening in a lutetium multi-ion optical clock. *Phys. Rev. Lett.*, 123:063201, Aug 2019.

[103] D. Turecek, J. Jakubek, and P. Soukup. USB 3.0 readout and time-walk correction method for timepix3 detector. *Journal of Instrumentation*, 11(12):C12065 (2016), Dec.

[104] B. van der Heijden et al. Spidr, a general-purpose readout system for pixel asics. *Journal of instrumentation*, 12(02):C02040, 2017.

[105] Ye Wang, Mark Um, Junhua Zhang, Shuoming An, Ming Lyu, Jing-Ning Zhang, L.-M. Duan, Dahyun Yum, and Kihwan Kim. Single qubit quantum memory exceeding ten-minute coherence time. *Nature Photonics*, 11(10), October 2017.

[106] Liu Wei, Chen Shu-Ming, Chen Ping-Xing, and Wu Wei. A Configurable Surface-Electrode Ion Trap Design for Quantum Information Processing. *Chinese Physics Letters*, 30(12):123702, 2013.

[107] Walter Thompson Welford. *Optics, Volume 14 of Oxford physics series.* Oxford University Press, 1976.

[108] D. J. Wineland, J. C. Bergquist, Wayne M. Itano, and R. E. Drullinger. Double-resonance and optical-pumping experiments on electromagnetically confined, laser-cooled ions. *Opt. Lett.*, 5(6):245–247, Jun 1980.

[109] John Wright. PhD thesis, University of Washington, 2015.

[110] John Wright, Carolyn Auchter, Chen-Kuan Chou, Richard D. Graham, Thomas W. Noel, Tomasz Sakrejda, Zichao Zhou, and Boris B. Blinov. Toward a scalable quantum computing architecture with mixed species ion chains. *Quantum Information Processing*, 15(12):5339–5349, December 2016.

[111] Kenneth Wright, Jason M. Amini, Daniel L. Faircloth, Curtis Volin, S. Charles Doret, Harley Hayden, C-S Pai, David W. Landgren, Douglas Denison, Tyler Killian, Richart E. Slusher, and Alexa W. Harter. Reliable transport through a microfabricated X -junction surface-electrode ion trap. *New Journal of Physics*, 15(3):033004, 2013.

[112] Jannes B. Wübbena, Sana Amairi, Olaf Mandel, and Piet O. Schmidt. Sympathetic cooling of mixed-species two-ion crystals for precision spectroscopy. *Phys. Rev. A*, 85:043412, Apr 2012.

[113] Dahyun Yum, Debashis De Munshi, Tarun Dutta, and Manas Mukherjee. Optical barium ion qubit. *J. Opt. Soc. Am. B*, 34(8):1632–1636, Aug 2017.

[114] J. Zhang, G. Pagano, P. W. Hess, A. Kyprianidis, P. Becker, H. Kaplan, A. V. Gorshkov, Z.-X. Gong, and C. Monroe. Observation of a many-body dynamical phase transition with a 53-qubit quantum simulator. *npj Quantum Information*, November 2017.

[115] Lijian Zhang, Leonardo Neves, Jeff S Lundeen, and Ian A Walmsley. A characterization of the single-photon sensitivity of an electron multiplying charge-coupled device. *Journal of Physics B: Atomic, Molecular and Optical Physics*, 42(11):114011, May 2009.

[116] Yingwen Zhang, Duncan England, Andrei Nomerotski, Peter Svihra, Steven Ferrante, Paul Hockett, and Benjamin Sussman. Multidimensional quantum-enhanced target detection via spectrotemporal-correlation measurements. *Phys. Rev. A*, 101:053808, May 2020.

[117] A. Zhao et al. Coincidence velocity map imaging using tpx3cam, a time stamping optical camera with 1.5 ns timing resolution. *Review of Scientific Instruments*, 88(9):113104, November 2017.

[118] Shi-Liang Zhu, C. Monroe, and L.-M. Duan. Trapped ion quantum computation with transverse phonon modes. *Phys. Rev. Lett.*, 97:050505, Aug 2006.

[119] Liudmila A. Zhukas, Maverick J. Millican, Peter Svihra, Andrei Nomerotski, and Boris B. Blinov. Direct observation of ion micromotion in a linear paul trap. *Phys. Rev. A*, 103:023105, Feb 2021.

[120] Liudmila A. Zhukas, Peter Svihra, Andrei Nomerotski, and Boris B. Blinov. High-fidelity simultaneous detection of a trapped-ion qubit register. *Phys. Rev. A*, 103:062614, Jun 2021.